# Sensorless control for Limp-home mode of EV applications

Ehsan Dehghan-Azad

B.Eng. (Hons)

A thesis submitted for the degree of Doctor of Philosophy

October, 2017

School of Electrical and Electronic Engineering

Newcastle University

United Kingdom

# ABSTRACT

Over the past decade research into electric vehicles' (EVs) safety, reliability and availability has become a hot topic and has attracted a lot of attention in the literature. Inevitably these key areas require further study and improvement. One of the challenges EVs face is speed/position sensor failure due to vibration and harsh environments. Wires connecting the sensor to the motor controller have a high likelihood of breakage. Loss of signals from the speed/position sensor will bring the EV to halt mode. Speed sensor failure at a busy roundabout or on a high speed motorway can have serious consequences and put the lives of drivers and passengers in great danger.

This thesis aims to tackle the aforementioned issues by proposing several novel sensorless schemes based on Model Reference Adaptive Systems (MRAS) suitable for *limp-home* mode of EV applications. The estimated speed from these schemes is used for the rotor flux position estimation. The estimated rotor flux position is employed for sensorless torque-controlled drive (TCD) based on indirect rotor field oriented control (IRFOC).

The capabilities of the proposed schemes have been evaluated and compared to the conventional back-Electromotive Force MRAS (back-EMF MRAS) scheme using simulation environment and a test bench setup. The new schemes have also been tested on electric golf buggies. The results presented for the proposed schemes show that utilising these schemes provide a reliable and smooth sensorless operation during vehicle test-drive starting from standstill and over a wide range of speeds, including the field weakening region. Employing these new schemes for sensorless TCD in *limp-home* mode of EV applications increases safety, reliability and availability of EVs.

# ACKNOWLEDGMENT

First of all I would like to thank God for providing me the opportunity of doing this PhD. and giving me strength throughout the project.

I would like to thank my supervisory team: Dr. Shady Gadoue, Dr. David Atkinson, Dr. Howard Slater and Dr. Peter Barrass, for sharing their valuable knowledge and guidance over the course of this project.

Thanks to Sevcon and its personnel for allowing me to use the Lab equipment and also being a great support throughout my undergraduate degree. I would also like to thank Dr. David Hodgson for his help during the setup of my test bench and being patient to answer my C-coding questions.

I would also like to thank Prof. Frede Blaabjerg for his constructive comments and willingness to provide comprehensive reviews of my work.

Finally I would like to thank my lovely wife for being supportive and sacrificial over the course of this project when I have lived most of my time in University rather than home.

# Table of Contents

# Table of Figures

# PRINCIPAL NOMENCLATURE

| | |
|---|---|
| $B$ | Friction coefficient |
| $J$ | Rotor inertia |
| $T_{em}$ | Electromagnetic torque |
| $PP$ | Number of pole pairs |
| $\sigma$ | Leakage coefficient |
| $T_r$ | Rotor time constant |
| $p$ | Differential operator |
| $R_s, R_r$ | Stator and rotor resistances |
| $L_s, L_r$ | Stator and rotor self-inductances |
| $L_{ls}, L_{lr}$ | Stator and rotor leakage-inductances |
| $L_m$ | Magnetising inductances |
| $\bar{i}_s$ | Space phasor of the stator current |
| $i_{s\alpha}, i_{s\beta}$ | Stator current components in the stationary reference frame |
| $i_{sd}, i_{sq}$ | Stator current components in the synchronous reference frame |
| $\bar{i}_r$ | Space phasor of the rotor current |
| $\bar{v}_s$ | Space phasor of the stator voltage |
| $v_{s\alpha}, v_{s\beta}$ | Stator voltage components in the stationary reference frame |
| $v_{sd}, v_{sq}$ | Stator voltage components in the synchronous reference frame |
| $\bar{v}_r$ | Space phasor of the rotor voltage |

| | |
|---|---|
| $\overline{e}_m$ | Space phasor of the back-electromotive force |
| $e_{m\alpha}, e_{m\beta}$ | Back-electromotive force components in the stationary reference frame |
| $e_{md}, e_{mq}$ | Back-electromotive force components in the synchronous reference frame |
| $\overline{\psi}_s$ | Space phasor of the stator flux linkage |
| $\psi_{s\alpha}, \psi_{s\beta}$ | Stator flux linkage components in the stationary reference frame |
| $\overline{\psi}_r$ | Space phasor of the rotor flux linkage |
| $\psi_{r\alpha}, \psi_{r\beta}$ | Rotor flux linkage components in the stationary reference frame |
| $\psi_{rd}, \psi_{rq}$ | Rotor flux linkage components in the synchronous reference frame |
| $\psi_{PM}$ | Permanent magnet flux linkage |
| $\omega_e$ | Angular synchronous speed |
| $\omega_r$ | Angular rotor speed |
| $\omega_{sl}$ | Angular slip speed |
| $\theta_e$ | Rotor flux angle |
| $\theta_r$ | Rotor angle |
| $\theta_{sl}$ | Slip angle |
| $V_{inj}$ | High frequency voltage |
| $V_c$ | Alternating voltage carrier |
| $i_c$ | High frequency current carrier |

## Superscripts

| | |
|---|---|
| * | Reference Value |
| ^ | Estimated Value |
| e | Synchronous reference frame |
| s | Stationary reference frame |
| r | Rotor reference frame |

## List of Acronyms

| | |
|---|---|
| AC | Alternating Current |
| BPF | Band-pass Filter |
| DC | Direct Current |
| DTC | Direct Torque Control |
| EKF | Extended Kalman Filter |
| ELO | Extended Luenberger Observer |
| EMF | Electromotive Force |
| EV | Electric Vehicle |
| FEV | Full-cell Electric Vehicle |
| FOC | Field Oriented Control |
| HEV | Hybrid Electric Vehicle |
| HFSI | High Frequency Signal Injection |
| ICE | Internal Combustion Engine |
| IM | Induction Motor |
| LPF | Low-pass Filter |
| MRAS | Model Reference Adaptive Systems |
| NN | Neural Network |
| PEV | Pure Electric Vehicle |
| PHEV | Plug-in Hybrid Electric Vehicle |
| PI | Proportional and Integral |
| PMSM | Permanent Magnet Synchronous Motor |
| PWM | Pulse Width Modulation |
| RHEV | Range-extended Hybrid Electric Vehicle |
| SMO | Sliding Mode Observer |
| SVM | Space Vector Modulation |
| TCD | Torque-Controlled Drive |

# CHAPTER 1. INTRODUCTION AND SCOPE OF THE THESIS

## 1. Introduction

In recent years, the electrification concept in the automotive industry has gained momentum as it promotes reduction in CO2 emissions and lowers operating costs. Consequentially, Electric Vehicles (EVs) are becoming a more popular choice over vehicles equipped with Internal Combustion Engines (ICEs). Popularity of EVs has prompted researchers to do further investigation into the functional safety of EV applications.

In this chapter a brief history of EVs and a general overview on the different classification of EVs are included. It also covers the reason why the sensorless concept is being used in EV applications, followed by an overall scope and novelty of this thesis. Finally the thesis layout is provided.

### 1.1.1 History of Electric Vehicles

The first EV, built by Thomas Davenport in 1834, was a battery-powered tricycle. From this point EVs began to thrive in the US to the point that, in 1900 they made up 38% of the total annual sale of automobiles second only to steam-powered vehicles, the best seller at 40% [1]. The high cost of EVs at that time was their main drawback, only affordable by the wealthy elite. In 1913 Henry Ford came up with the idea of mass-producing of ICE vehicles, using the integrated moving assembly line, which pushed EVs out of the market [1]. The Ford vehicles were the first vehicle that many of the middle class Americans could afford and offered a far greater distance range to that of the EVs. Due to the dominance of ICE vehicles there was a long period of absence of EVs in the marketplace. However, since 1970 as part of the move towards renewable and cleaner energy sources, interest and development of EVs has been reignited [1].

In general, EVs can be divided into three main types; Hybrid EV (HEV), Pure EV (PEV), and Full-cell EV (FEV) [1]. These vehicles can be classified further, shown in Fig. 1.1, with respect to their source of energy and propulsion mechanism. HEVs use gasoline/diesel and electricity for energy with the propulsion mechanism including both the electric motor and engine. These vehicles can be further divided into the conventional and gridable types [1]. The conventional HEVs cannot be recharged by electricity and are only refueled with gasoline/diesel. Depending on the level of hybridisation these vehicle can be further divided into; micro-, mild- and full-HEVs [1]. However, the gridable HEV can be recharged with electricity and can be divided into the plug-in HEV (PHEV) and range-extended HEV (RHEV). PEVs use electricity for energy with the electric motor for its propulsion mechanism. FEVs use hydrogen (directly or indirectly) for energy with the electric motor for its propulsion mechanism [1].

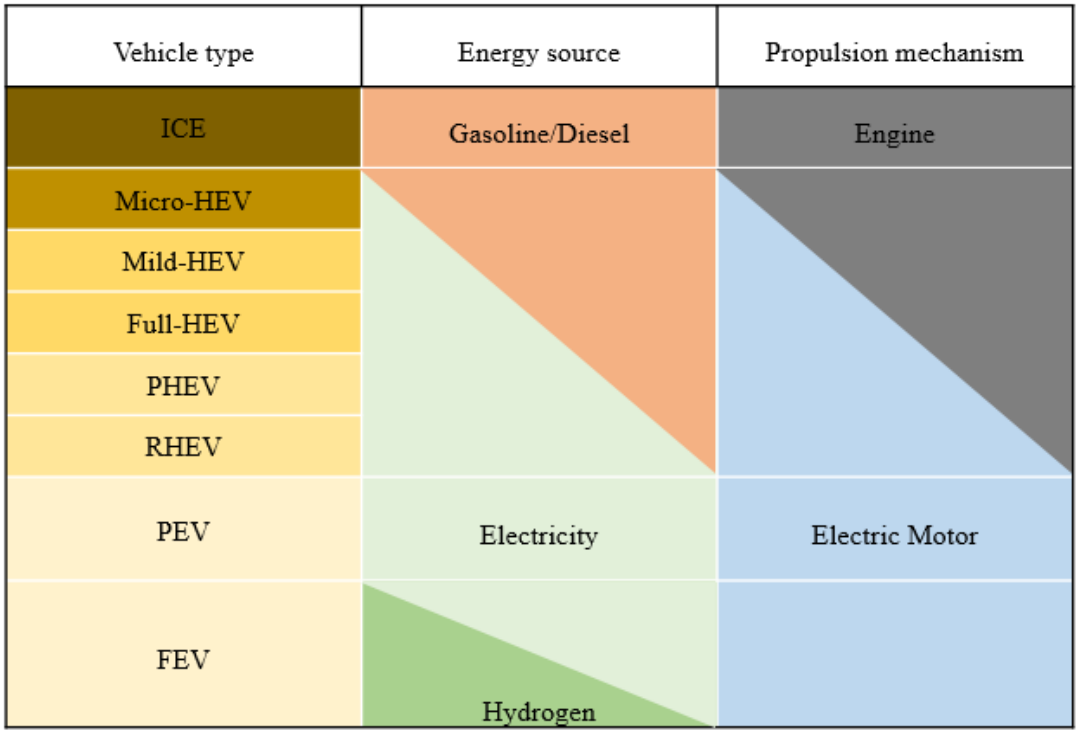


**Fig. 1.1. Classification of Electric Vehicles [1].**

### 1.1.2 Why sensorless control for Electric Vehicle applications?

Electric propulsion is the main system in EV applications which consists of three components: a transmission device, wheels and an electric motor drive [2]. The choice of electric motor drive is usually based on vehicle limitations, source of energy and driver expectations [2]. The electric motor drive includes; a motor controller, electric motors, a battery package with its charging circuitry, and sensors. The motor controller can be described as the brain in EVs, therefore, the efficiency and safety of EV applications is highly dependent on the health of the motor controller. Sensors measure properties, e.g. temperature, current, voltage and speed/position, and provide information to the motor controller. The accuracy and consistency of these sensors plays an important role in the overall health of the electric motor drive.

By carrying out the Failure Mode and Effect Analysis (FMEA) for the electric motor drive used in an EV application, one would note that speed/position sensor failure can have catastrophic consequences, for instance on a busy roundabout or highway. Although this failure may not have a high level of exposure classification in the Automotive Safety Integrity Level (ASIL), the severity and controllability classifications are very high. Therefore it is critically important and required by the road vehicles-functional safety standards (ISO26262) for the

drive mechanism, which is employed for EV applications, to be fault tolerant to the speed/position failure. The fault tolerant drive allows drivers and passengers of EVs to reach their destinations safely without disruption despite the occurrence of fault or failure [3], which is known as *limp-home* mode. It is a common safety practice in the event of any abnormality in the drive-train, e.g. speed/position sensor failure, for the power-train control module (PCM) to set the operation mode to *limp-home*. In this mode, the amount of power available is limited, reducing the maximum speed of the vehicle. This is a programmed response regardless of the nature of the failure. These speed and power limitations vary in every company but the essence of *limp-home* mode is to prevent the vehicle from further damage. Moreover, the EV driver has no choice but to take the vehicle to the nearest service centre. In this project, during *limp-home* mode of operation, the sensorless drive is expected to be capable of functioning in the following operation conditions:

- Capable of operating in a wide range of speeds (from standstill to twice the base speed of the electric motor)
- Reliable starting from standstill with the correct direction to that selected by the driver
- To be robust against parameter variations
- Smooth torque control capabilities during starting from standstill to reduce oscillations whilst the motor is coupled to the gearbox
- To be capable of operating in forward and reverse mode.

These conditions are expected to be satisfied regardless of distance travelled by the vehicle. However, using the senseless concept for the *limp-home* mode of EV applications, the electric drive's performance in the hill-hold operation is expected to experience some degradation. This is a tradeoff to increase safety, reliability and availability of the EV. The *limp-home* mode concept consists of a fault detection mechanism, a transition mechanism between *sensored* to sensorless control techniques and vice versa, and more importantly, a robust and accurate speed/position estimator. The latter is of high importance and will only be addressed in this research. In EV applications high computational effort is already required to implement various control schemes, this is to achieve the functional safety which is a critical aspect. Therefore because of the limited computational resources in the motor drive controller, the sensorless algorithm employed for fault tolerant purposes should not be too complicated. For EV applications torque-controlled drive (TCD) of induction motor (IM) is normally used [4]. In the absence of a mechanical sensor, TCD based on indirect rotor field oriented control (IRFOC) requires sensorless speed estimation for rotor flux angle calculation.

## 1.2 Scope and Novelty of the Thesis

The presented research in this thesis investigates sensorless operation in the *limp-home* mode of EV applications. Particular attention is given to the reliability of the sensorless mechanism used during vehicle-starting from standstill, smooth and safe sensorless operation in a wide range of speeds, including the field weakening region. The important scientific contributions originating from the research in this thesis are as follows:

1. A novel back-Electromotive Force model reference adaptive system (back-EMF MRAS) scheme with a compensating mechanism is developed. Unlike the conventional back-EMF MRAS, the new scheme is robust against motor parameter variation and errors due to digitisation in high speed regions. The new scheme not only offers a consistent sensorless vehicle-starting from standstill for consecutive attempts, but also is reliable over a wide range of speeds, including the field weakening region. Utilising this scheme also provides a smooth sensorless operation in vehicle hill-starting.
2. A novel stator voltage MRAS (Vs-MRAS) is proposed which, unlike existing MRAS schemes, does not require the prerequisite knowledge of stator resistance, stator inductance and rotor resistance nominal values and is, therefore, robust against motor parameter variation. The proposed scheme provides a consistent sensorless operation during vehicle-starting from standstill and smooth vehicle test-drive over a wide range of speeds, including the field weakening region.
3. A novel universal hybrid Vs-MRAS (HVs-MRAS) scheme is developed for sensorless control of IM and surface-mounted permanent magnet synchronous motor (SPMSM) drives. Utilising the new scheme provides a reliable and consistent sensorless operation during vehicle-starting from standstill and smooth operation over a wide range of speeds, including the field weakening region. The scheme is also robust against parameter variation and errors due to digitisation.

## 1.3 List of Publications

This thesis is predominantly based on the research findings which have been published in journals and an international conference. A list of these publications is given below:

- E. Dehghan-Azad, S. Gadoue, D. Atkinson, H. Slater, P. Barrass, and F. Blaabjerg, "Sensorless Control of IM for Limp-Home Mode EV Applications," *IEEE Transactions on Power Electronics*, vol. 32, pp. 7140-7150, 2017, [5].

- E. Dehghan-Azad, S. Gadoue, D. Atkinson, H. Slater, P. Barrass, and F. Blaabjerg, "Sensorless control of IM based on stator-voltage MRAS for Limp-home EV applications," *IEEE Transactions on Power Electronics*, Published in Early Access Articles, 2017, [6].
- E. Dehghan-Azad, S. Gadoue, D. Atkinson, H. Slater, and P. Barrass, "Sensorless Torque-Controlled Induction Motor Drive for EV applications," *IEEE Transportation Electrification Conference and Expo (ITEC)*, pp. 263 - 268, 2017, [7].

## 1.4 Layout of the Thesis

This thesis consists of eight chapters, organised as follows:

- Chapter 1 gives a brief introduction on the history of EVs and covers the importance of the sensorless concept in EV applications. It also includes the aims of the project and a list of scientific contributions and publications produced during the course of this project.
- Chapter 2 provides a comprehensive literature review on the sensorless control concept. This includes: the fundamental model based schemes, high frequency signal injection (HFSI) schemes, the hybrid schemes and unified sensorless schemes for different AC motors. Regarding the review on the fundamental model based schemes, attention has been focused on the MRAS schemes.
- Chapter 3 presents the mathematical principles of the IM and SPMSM. It also includes mathematical proof of the rotor-field oriented control. The mathematical derivation of the conventional back-EMF MRAS and the principle of a high frequency signal injection scheme used in this project are also provided.
- Chapter 4 gives a detailed description of the experimental test bench setup and provides a detailed account of the electric golf buggies used in this project.
- Chapter 5 presents a new back-EMF MRAS used for the sensorless control of IMs in the *limp-home* mode of EV applications. The performance of the new scheme is compared against that of the conventional back-EMF MRAS scheme using simulation environment and experimental test bench setup. The new scheme is also tested separately on an electric golf buggy.
- Chapter 6 describes a new sensorless scheme for IMs based on the Vs-MRAS scheme. The performance of this scheme is validated and compared with the conventional back-EMF MRAS using simulation environment and experimental test bench setup. The

capability and suitability of the new scheme for the *limp-home* mode of EV applications is experimentally approved by implementing the scheme on an electric golf buggy.

- Chapter 7 gives a full description of a new universal sensorless control based on the HVs-MRAS scheme. The performance of the new scheme is experimentally verified on two IMs and SPMSMs using experimental test bench setup and two electric golf buggies.
- Chapter 8 includes the overall conclusions of the thesis and recommendations for future works.

# CHAPTER 2. SENSORLESS CONTROL SCHEMES - A LITERATURE REVIEW

## 2.1 Introduction

The sensorless control concept was initially proposed to reduce the cost and size of a *sensored* electric drive and also reduce the complication which arises due to speed/position sensors' wiring [8]. Utilising the sensorless control concept promotes less complexity and maintenance requirements, and enables the drive to become more immune to noise. As a result, the reliability of the drive increases when operating in hostile environments. Over the past four decades several solutions for sensorless drives have been proposed in the literature. Therefore, in this chapter, a comprehensive review of the sensorless control techniques is carried out. This chapter provides a comprehensive review on sensorless control schemes for EV applications including fundamental model based methods, mainly focused on MRAS schemes, and HFSI schemes. A review of hybrid schemes which combine both model-based and HFSI schemes is included and finally, a review on universal sensorless control schemes for AC motors is provided.

## 2.2 Sensorless control based on fundamental model schemes

Fundamental model-based sensorless techniques are usually based on stator voltage (reconstructed, from the measured DC link and switching signals, or measured) and stator current components in the stationary reference frame. These schemes can be divided into two main groups: open-loop and closed-loop [9]. The closed-loop estimators, also known as observers, usually benefit from a correction term, which adjusts the estimator [9]. On the other hand the open-loop schemes do not have a correction term and are normally based on the stator voltage equation of the machine which make their accuracy greatly dependent on the motor nominal parameters used [9]. Therefore the performance of the sensorless drive, which utilises an open-loop estimator, seriously degrades during parameter variation, especially in the low speed region.

Schemes based on Kalman filters (KF) and Luenberger observers (LO) are common examples of the closed-loop type estimator. The KF and its extended version (EKF) are both of stochastic types. However, the KF can only be employed for linear systems, whereas the EKF can be used for non-linear time-varying systems [9]. Schemes based on EKF are computationally intensive and their precision is highly dependent on both the machine model parameters and measurement noises [8-11]. Moreover, at around zero speed, where the measurement errors are more significant than the stator voltage components, EKF schemes lose their control abilities [9].

In [12], in order to reduce the computational intensity of EKF and improve its performance, a sensorless scheme based on a reduced-order EKF was employed using a field programmable gate array (FPGA). This scheme employs fixed covariance matrices. Experimental results show that, using this scheme, a good position and speed estimation can be achieved up to 1000 rpm. However, during transient conditions accurate speed estimation cannot be guaranteed [13]. Moreover, the performance of the scheme around zero speed was not studied which is problematic for EKF schemes. In [14], a sensorless speed and flux estimation method has been proposed based on a multiple-model EKF with Markov chain (MC-MM-EKF). This scheme was experimentally tested and from comparison results, between proposed and interacting MM-EKF, one can see that utilising the proposed scheme reduces the error between the estimated and the measured speeds by almost 50%, however, not complete eradication. In addition, implementing this scheme adds extra computational efforts to the existing scheme.

Regarding LO, this scheme is deterministic in nature. This scheme is employable for linear time-variant systems, whereas nonlinear time-variant systems require using an Extended

LO (ELO) scheme [9]. The ELO schemes have more merits than conventional EKF. These are their relatively simple algorithm and easier tuning [9]. In [15], a new position sensorless scheme based on LO was proposed. In contrast to the conventional LO, this scheme does not require the speed estimation. Therefore it reduces the complexity related to the speed estimation errors of the observer. Recorded experimental results show that utilising this scheme provides a good performance above 10 rpm, regardless of whether a load was applied or not . However, similar to KF, LO is also not capable of performing well at zero and very low speed regions [9].

Another type of deterministic observer is a sliding mode observer (SMO). In this kind of observer, the error between measured and estimated stator current components are normally used with a sign function. The output of the sign function, which is the estimated back-EMF components, is then used to update the SMO. The back-EMF components in the stationary reference frame are then filtered using a Low-pass Filter (LPF). The filtered back-EMF components are used to extract the position and speed of motor. Utilising a sign function in this scheme is known to introduce chattering on the estimated speed and torque. Therefore, Kim et al. [16] have proposed a sensorless scheme based on SMO which replaces the sign switching function with a sigmoid function. This is to reduce the excessive chattering effect of the conventional scheme. Utilising this scheme eliminates the need for a LPF, this results in a faster dynamic response. To avoid problems with stator resistance variation an estimator is also employed, assisting with this parameter variation. However, the chattering issue associated with the SMO has not been entirely eliminated. The scheme has a bigger overshoot in comparison to the conventional scheme and also has steady state error between measured and estimated speeds.

In [17], in order to reduce chattering issues, a fixed-boundary-layer SMO (FBL-SMO) has been proposed in the synchronous reference frame for the purpose of EV applications. Experimental validation demonstrated by the author, in [17], show the actual speed and torque profile using a vehicle-drive simulator. It can be seen that a wide speed range from zero up to 6000 rpm has been achieved when the proposed scheme is used. However, the chattering effect can be seen on the speed and torque signals, especially on the torque signal. For EV applications, consideration should be given to sensorless schemes, known for being the most accepted representative candidate for the high performance, which are those based on MRAS [18]. Hence, MRAS schemes are discussed next.

### 2.2.1 Model reference adaptive systems and their shortcomings

Schemes based on MRAS [19, 20] are known for their low computational efforts and simplicity to implement [21]. The overall block diagram of a MRAS scheme is shown in Fig. 2.1. MRAS schemes usually consist of a reference model, an adjustable model and an adaptation mechanism, which is often a proportional and integral (PI) controller. The reference model is normally speed independent and its output components are calculated based on the voltage model in the stationary reference frame. Whereas the adjustable model is speed dependent and its output components are calculated using the current model in the stationary reference frame. The principle is that the difference between output components of the reference and the adjustable models are used through a PI controller to reduce the error in the estimated speed [22]. This estimated speed is then used to update the adjustable model accordingly. Depending on how the error between the reference and the adjustable models is calculated, MRAS schemes vary from one another, which are depicted as follows.

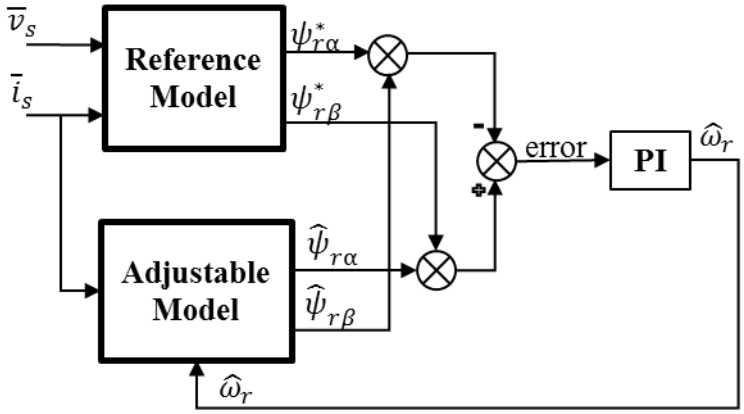


**Fig. 2.1 Block diagram of MRAS [19].**

### 2.2.2 Different MRAS schemes

Schauder [19] has proposed a MRAS scheme based on rotor flux (RF-MRAS) components in the stationary reference frame. This scheme was experimentally tested and results show a satisfactory performance apart from the zero speed region. The author has indicated that if this scheme is used in the zero speed region, it can result in the instability of the speed control. Since an open-loop integrator is used in the reference model of this scheme, it suffers from pure integration problems, such as; DC drift and initial condition [9, 20]. This scheme also suffers from parameter variation, especially stator resistance variation due to

temperature rise [9]. This scheme is the most studied scheme among MRAS schemes in literature. Consequently, several studies have aimed to improve its performance, which are now described.

In [23], a new scheme has been proposed based on a combined adaptation mechanism, based on the electromagnetic torque and the rotor flux components. The results in [23] demonstrated that utilising this scheme helps the RF-MRAS to be more robust in the low speed region. However, this scheme still suffers from sensitivity to parameter variation. In [24], also based on combination of the torque and the rotor flux equations a new scheme has been proposed to improve the RF-MRAS in low speed regions. Utilising this scheme increases complexity of the classical RF-MRAS. From results, recorded while the scheme was used, one can see that under 50% load it is highly sensitive to the stator resistance variation. Authors in [25, 26] have employed a SMO to improve problems associated with the high PI controller gains in noisy conditions. In [27], the reference model of the RF-MRAS is replaced with a sliding mode stator voltage model observer. These schemes introduce undesirable chattering on the torque response and remains sensitive to motor parameter variation.

In another attempt to improve the performance of the RF-MRAS, Peng and Fukao [20] have proposed two new MRAS schemes. The first scheme is based on the back-EMF-MRAS and the second one based on the instantaneous reactive power (RP-MRAS). Utilising the first scheme eliminates the need for integration in the reference model. As a result, the pure integration problems are solved and are no longer an issue, however, this scheme is still sensitive to parameter variation. It is worth mentioning that problems due to pure integration can also be solved using a LPF with a high gain instead of integrator. Nevertheless, this substitution causes instability in the low speed region [20, 26]. The second scheme is also free from pure integration problems and does not require the knowledge of stator resistance. However, this does not mean that the RP-MRAS scheme is robust against parameter variations. The main shortcoming of RP-MRAS scheme is also reported by [28], as lacking stability in the regenerating mode.

In order to overcome the shortcomings of the conventional RP-MRAS, [29] has proposed a new RP-MRAS scheme which is formed in the synchronous reference frame. Although, utilising this scheme eliminates the differentiating term, problems in the regenerating mode remained unsolved. In another attempt [30], has introduced a new function, represented by ‘X’, which aims to tackle the problem in the regenerating mode. The scheme has been experimentally tested and presented results demonstrate that this scheme is stable during regenerating mode. However, it is dependent on the knowledge of stator resistance. Authors in [31, 32] have combined artificial neural networks (ANNs) with RP-MRAS and RF-MRAS,

respectively. These schemes show a good performance in the low speed region and are stable in the regenerating mode, providing they are trained properly [28]. These schemes also require extensive computational efforts.

A MRAS scheme based on mutual inductance (M-MRAS) has been proposed in [33]. Unlike the aforementioned MRAS schemes, where the reference and the adjustable models are fixed, this scheme takes advantage of both models and employs them interchangeably. The approach allows simultaneous estimation of the rotor speed and the stator resistance value. This scheme was experimentally tested and results show a good speed performance for ± 1200 rpm. However, utilising this scheme in high speed regions requires the PI controllers' gains in the speed and current regulation loops to be retuned [33], which is undesirable. Furthermore, fast transient through zero might not be problematic but when dwelling in zero speed can cause this scheme to become unstable.

Orlowska-Kowalska and Dybkowski [34] have also proposed a new scheme based on stator current MRAS (Is-MRAS). In this scheme, in order to form the error tuning signal the estimated rotor flux components are multiplied to the error between the measured and the estimated stator current components. Recorded experiment results, when the motor nominal parameters are used, verify robustness of this scheme over a wide range of speed, including the field weakening region. Nevertheless, from the results for parameter variation tests, it can be seen that this scheme is sensitive to motor parameter variation.

The aforementioned MRAS schemes have been initially proposed for sensorless control of IM. However, these schemes can also be employed for sensorless control of PMSMs [35-38]. Rashed et al. [38] have proposed a MRAS scheme based on stator current components in the stationary reference frame for SPMSM. This scheme consists of two separate schemes. In Scheme 1, the rotor speed and stator resistance values are estimated and in Scheme 2 the rotor speed and the rotor flux magnitude are estimated. In order to operate in all conditions a combination of both schemes is required. This scheme benefits from the stator resistance estimator, hence, is robust against problems associated to its variation. However, the combination of both schemes requires significant computation processing. In [37], a back-EMF MRAS scheme is used for sensorless control of an interior permanent magnet synchronous motor (IPMSM). The reference back-EMF components are calculated using a SMO. The performance of this scheme in the medium and high speed regions from 3000 rpm to 5000 rpm is experimentally validated however, the paper has not made any comments on the performance of the proposed scheme in the low speed region and against parameter variation.

Marwali and Keyhani [21], have carried out a thorough comparative study, using simulation and experiments, between RF-MRAS and back-EMF MRAS. This study suggests

that it is extremely difficulty to implement the reference model of RF-MRAS due to the open loop integration used for calculating the rotor flux. Hence, for experimental implementation of RF-MRAS, this scheme should undergo some modifications. These modifications include the addition of LPFs to the output and input of the reference and adjustable models respectively [19, 22]. The addition of LPFs can lead to phase error and considerable delays in the speed estimation [39]. To overcome these issues [40] has employed a programmable cascaded LPF for the rotor flux calculation. Authors in [21], have also concluded that the low speed performance of the back-EMF MRAS is better than the RF-MRAS. Comparative study in [41] also concluded that the back-EMF MRAS has better tracking capability and fulfils the requirement as a versatile estimator.

As a result, the back-EMF MRAS is concluded to be a better candidate among MRAS schemes. The back-EMF MRAS implementation is relatively simple and can also be employed for sensorless control of PMSMs [37]. In the next subsection the common shortcomings of this scheme and their remedies provided in literature are discussed.

#### *2.2.2.1 Common shortcomings of back-EMF MRAS schemes*

As mentioned previously the Back-EMF MRAS scheme does not have problems associated with the pure integration. However, removing the integrator gives rise to the magnification of any noise in the reference model due to the derivative term. Shortcomings of this scheme also arise from disturbances in the stator voltage components, which are used as input variables in the reference model. These disturbances are mainly identified to be due to the four following reasons;

1) Variation in the stator resistance nominal value due to temperature rise [20, 42].
2) Variation in the magnetising inductance nominal value due to saturation effects, which in turn causes variation in the stator and rotor self-inductance nominal values [20].
3) Voltage drops due to inverter nonlinearities (e.g. switching dead-time and voltage drop of power semiconductor devices) [43, 44].
4) Errors due to digitisation in high speed regions [45, 46].

These disturbances can cause steady state error, oscillation and eventually leads to instability, especially in the low speed region in the cases of stator resistance variation and inverter nonlinearities. Online adaptation of the stator resistance estimator is the normal approach to deal with its variation issue [44]. In order to make the conventional back-EMF MRAS scheme immune to the stator resistance variation, speed and stator resistance estimators were proposed in [42] to operate simultaneously. The new combined scheme is reported to improve the stability of the back-EMF MRAS and increase its robustness against the stator

resistance mismatch. However, during a speed transient and no-load condition this scheme suffers from drift problems and it increases the complexity compared to the conventional scheme.

Stator voltage components can be measured by employing a voltage sensor, or a voltage measuring circuitry [47]. However, it is more common, in industry applications, to reconstruct the stator voltage components in the stationary reference frame by using the measured DC-link voltage value and the inverter switching signals. These switching signals are effected by the inverter nonlinearities. If these nonlinearities are not taken into account, they can cause voltage errors between the stator reference and actual input voltages of a motor. At very low speeds, these errors can even become larger than the motor's stator voltage [43], which can have a serious effect on the performance of the back-EMF MRAS in low speed regions. In [44], issues associated with inverter nonlinearities have been dealt with by considering a more accurate model of an inverter. Authors have experimentally shown that utilising this approach enables more accurate estimation.

Moreover, digitisation can also cause phase error in the reference model in high speed regions, especially the field weakening region [45, 46], which can lead to the back-EMF MRAS instability. In [46], to deal with the phase errors related to digitisation, an angle regulator feedback using the difference between the amplitude of the reference and the estimated components has been proposed. From experimental results, demonstrated at a constant speed of 10000 rpm with a step load change, it can be seen that by utilising this scheme with the regulator, an improved performance can be achieved. The scheme is more stable, and the estimated speed closely follows the reference speed without any steady state errors.

## 2.3 Sensorless control based on high frequency signal injection schemes

The fundamental model based schemes discussed so far are more suitable for medium and high speed regions. In order to have a reliable sensorless drive in zero and very low speed regions, schemes based on HFSI have been employed in literature [48-53]. By injecting a high frequency signal, which is much higher than the fundamental frequency of the machine, HFSI schemes benefit from specific motor properties. These are not available when a model based scheme is used. The injected high frequency signal is also referred to as a carrier signal [54]. Depending on the nature of the injected carrier signal and also where it is injected, these schemes vary from one another. Thus, they can be divided into three main approaches;

1) Injection of a pulsating carrier signal in the synchronous reference frame [48-51]

2) Injection of a rotating carrier signal in the synchronous reference frame [52]
3) Injection of a rotating carrier signal in the stationary reference frame [53].

It is possible to perform HFSI based on either current or voltage high frequency carrier signal injections, but the voltage carrier injection methods have been considered more often, in literature, over the current carrier injection methods. The latter methods provide a higher speed control bandwidth, but they are more vulnerable to effects of inverter nonlinearities, e.g. dead time [48]. Utilising the former methods require the feedback current components to be filtered which reduces the bandwidth of the current control. However, this method is more robust to the error due to inverter nonlinearities [48]. In order to extract the desired information, the high frequency carrier signal components are retrieved by different signal demodulation process techniques.

### 2.3.1 Different HFSI schemes

Janson and Lorentz [53] have proposed a HFSI sensorless scheme based on a rotating carrier signal injection in the stationary reference frame. This is to drive IM and salient AC machines in zero and low speed regions. In order to track rotor magnetic saliencies, a closed loop position and velocity observer incorporating heterodyning demodulation has been employed. The scheme is verified experimentally and the results demonstrate that using this scheme provides a sustained zero and low speed/position operation. However, implementing this scheme for an IM is only possible if the machine rotor has undergone modification. Authors also reported that the scheme is sensitive to inverter nonlinearities, e.g. dead time. Moreover, the saturation-induced anisotropy is not considered, which restricts this approach to unsaturated machines only [54].

Ha and Sul [48], have proposed a HFSI scheme for IMs which is of the type with a pulsating carrier injection in the synchronous reference frame. The scheme can be used in both voltage or current high frequency carrier injection approaches. Considering the voltage carrier injection method of this scheme, a high frequency pulsating voltage signal is added to the estimated d-axis stator voltage, after the current controller in the synchronous reference frame. The principle of this method is that since the injected high frequency voltage carrier is fixed, the terminal impedance components are dependent on the resulting HF stator current components [48]. By dividing carrier voltage by the resulting stator current components, terminal impedances are calculated. Finally, the error between the impedance components is fed through a PI controller which is equal to the rotor flux position. The authors have

demonstrated that, by experimental validation, using this scheme a satisfactory operation at zero stator frequency with 150% load torque can be achieved. This scheme requires a higher carrier amplitude injection when the machine is fully saturated. This is due to the difference between the impedance components being very small to detect [54]. Moreover, the performance of this scheme decays in the presence of high-order saliencies [52].

In [49], based on the pulsating voltage injection in the synchronous reference frame, a new scheme has been proposed for SPMSMs. This scheme takes advantage of the magnetic saliency of the motor which contains information about the rotor position. This saliency is as a result of the saturated stator core around q-axis of the motor due to the permanent magnet [49]. Therefore, the principle is that by injecting a pulsating HF carrier voltage signal the aforementioned magnetic saliency is detected on the measured resulting HF q-axis stator current. To extract information from this current, the measured stator currents are first transformed from stationary to synchronous reference frame. After that the q-axis current is passed through a high frequency signal demodulation process which in return provides the error signal. Finally, this error signal is passed through a PI controller, or a bang-bang controller, whose output is equal to the electrical rotor speed. Integrating this speed provides the rotor flux position. The authors have demonstrated, using experimental validation, a robust sensorless control at zero speed with 100% load can be achieved. However, using this scheme the absolute polarity of the magnet cannot be determined when starting from standstill. This can result in unpredictable starting direction and is a critical safety hazard for EV applications.

In another attempt [50], has proposed a scheme for PMSMs based on a pulsating voltage carrier signal injection in the synchronous reference frame which utilises zero-sequence voltage to extract angle information. Usually schemes based on the zero-sequence carrier voltage sensing method use rotating signal injection in the stationary reference frame [55], but this scheme injects a pulsating HF voltage in q-axis. Therefore, the proposed signal demodulation process is relatively simpler and is less effected by the processing delays. To measure the zero-sequence voltage, three resistors are required to be added in parallel to the input of the motor stator windings. The voltage between the neutral point of the stator windings and the three resistors is used as an input to the signal demodulation process. This scheme has been experimentally tested and the results show a good performance for various speed and torque conditions. However, from results shown in figure 13 of this paper, it can be seen that this scheme cannot provide a reliable initial rotor position estimation as it suffers from angle ambiguity of $\pi$ radians when starting from standstill. Moreover, implementing this scheme requires an extra voltage sensor to measure the voltage of the three resistor networks with respect to the neutral point of the motor.

Unlike the aforementioned HFSI schemes where injected carrier signals are sinusoidal, in [51] a HFSI scheme based on a pulsating square-wave type voltage signal injection in the synchronous reference frame has been proposed. This scheme does not require LPFs on the feedback stator current components, hence it has an increased current controller bandwidth. The scheme has been experimentally tested on an IPMSM. From recorded results it can be seen that a good speed estimation can be achieved from zero to 1500 rpm. However, the performance of the scheme when full load is applied at zero speed has not been demonstrated. Moreover, this scheme requires an additional magnet polarity detection mechanism when a correct direction for starting from standstill is required [56].

In [52], to reduce the effect of the secondary saliencies a new HFSI scheme based on a rotating voltage injection in the synchronous reference frame has been proposed for an IM. The new harmonic elimination method is based on the KF. The proposed scheme has been experimentally validated. Results show a satisfactory performance when this scheme is used during load step change from 30% to 80% at 60 rpm and speed step change from 60 rpm to 0 for 50% constant torque. However, this scheme is computationally complex and according to the authors, the scheme does not perform well at zero speed under low load conditions.

Schroedl [57] has proposed a sensorless scheme for AC machines based on exploiting the response of an anisotropic machine to PWM transients. This approach is known as Indirect Flux detection by On-line Reactance Measurement (INFORM). The magnetic anisotropy in the IMs and PMSMs reveals information about the flux axis. This anisotropy can be detected from complex INFORM reactance. This is calculated from the rate of change of the stator current over a short interval due to the stator voltage. The scheme has been experimentally validated and results, including torque reversal ±120% for an IM at zero and 100 rpm, confirm effectiveness of this scheme for sensorless speed and position estimation, at very low speed regions. The estimated rotor flux angle from INFORM method gets a certain angular displacement when the torque producing current is applied. Hence, a correction function based on KF is used, which makes this scheme computationally intense. Moreover, this scheme is more suitable for IMs with the closed rotor slots [54].

#### *2.3.1.1 Short comings*

Utilising HFSI based schemes have their own limitations. These are listed as follows;

1) These schemes are sensitive to the effects of inverter nonlinearities, such as dead time. Therefore, a complex and time-varying function is required to compensate for each operating point [54, 58].

2) Utilising these schemes introduces extra losses and transient disturbances in the medium and high speed regions, which distorts the performance of the drive [58]. Hence they are more suitable for zero and low speed regions.
3) These schemes normally require an extra magnet polarity identification mechanism [59-61]. This is to deal with the angle ambiguity of $\pi$ radians which occurs while the magnet polarity is initially being identified. This can cause reverse rotations during start up or complete failure to start [62].

## 2.4 Hybrid schemes: combination of fundamental model based and HFSI schemes

In general, the implementation of sensorless control of AC machines using the fundamental model based methods are less complicated than schemes based on the HFSI methods. This gives the fundamental model based schemes a distinct advantage making them a good candidate for most applications [54]. However, using these schemes for long-term dwelling in zero stator frequency is an issue. This can be solved by employing a HFSI scheme at zero and very low speed regions as a temporary addition. Therefore, hybrid (or combining) sensorless schemes based on a combination of both fundamental model based and HFSI schemes have been investigated in literature [56, 58, 62-65]. Utilising a hybrid scheme enables the sensorless drive to operate over a wide range of speed. In order to amalgamate both schemes a combining (or blending) function is also required.

In [56] a hybrid sensorless scheme has been proposed for IPMSM. This scheme employs the extended back-EMF scheme, proposed by Morimoto et al. [66], for medium and high speed regions. The HFSI scheme in [51] is used for operations in zero and low speed regions. In order to combine these schemes a speed dependent combining function is used. Moreover, for the sensorless drive to start reliably from standstill a magnet polarity detection method is used which requires 0.22 seconds to detect the polarity. The scheme has been experimentally evaluated and results show a smooth acceleration from zero to rated speed of 3000 rpm can be achieved under full load operation.

Foo and Rahman [63] have proposed a sensorless scheme for IPMSM based on a combination of an improved SMO, for medium and high speed regions, and a HFSI scheme, for zero and low speed regions. The employed HFSI scheme uses a rotating voltage injection in the synchronous reference frame, similar to [52]. A speed dependent function is also employed for transition between both schemes. The scheme has been experimentally tested at standstill under full load condition and speed reversal ±1000 rpm (two thirds of the motor based

speed) without load. However, from results it can be seen that as the speed increases so does the ripple in the estimated speed, which can become problematic in the field weakening region.

In another attempt, Andreescu et al. [62] have proposed a combined stator flux observer with a HFSI scheme for sensorless DTC of IPMSM. The flux observer is based on two merged observers, which are an open loop current model observer and a close loop voltage model observer. The employed HFSI is based on a rotating HF carrier voltage signal injection in the synchronous reference frame. In order to make the drive reliable during starting from standstill, this paper utilises the initial rotor position identification scheme in [59]. The combined scheme has been experimentally validated in full load operation for speed ranges of 1 rpm to 1750 rpm (rated speed). However, from the results it can be seen that the measured speed and the estimated torque signals contain considerable oscillations, which is due to the nature of the DTC.

In [58] a hybrid sensorless scheme has been proposed for SPMSM. This scheme takes advantage of the saliency detection method [67] for zero and low speed regions, which is based on the rotating voltage carrier signal injection in the stationary reference frame. For the medium and high speed regions a voltage model flux observer is used. In order to combine these schemes a flux compensating mechanism has been proposed. The compensating mechanism uses the flux components, which are calculated using the estimated angle from the HFSI scheme, as its reference. The error between the reference flux and the output flux components of the voltage model is then forced to zero using a proportional controller. A speed transition function is also used to switch the compensating mechanism ON/OFF. The voltage injection itself is separately hard switched using a hysteresis band. The scheme has been experimentally tested and results show a satisfactory performance during steady state and transient from zero to ±1500 rpm (half the motor base speed) has been achieved. Results also confirm reliability of this scheme during several attempts for sensorless starting from standstill.

## 2.5 Universal sensorless control schemes

When a sensorless drive is required to be applied for several AC motor applications, schemes based on universal sensorless control (USC) are a suitable choice, as these schemes can reduce computational complexity of the whole drive. Although utilising these schemes might not be as efficient as individually designed and optimised schemes for IM and PMSM, it is more applicable for an application engineer or technicians who do not have a vast array of sensorless drive experience.

In [68], a USC scheme utilising a stator flux linkage estimator has been proposed. This scheme benefits from a high-precision voltage integrator to deal with pure integration problems. The scheme was experimentally tested in the speed and torque control modes on three types of motors; IM, SPMSM, and IPMSM. From the recorded results it can be seen that this scheme, by considering iron loss, can improve torque control accuracy, especially for the IM control. Utilising this scheme also extends the load range in low speed regions for the IM. However, as it is also reported by the authors, this scheme is sensitive to motor parameter variation. Moreover, the scheme employs an incremental start-up operation, which is not reliable or robust enough in the case of PMSMs, where absolute magnet polarity is required. Therefore, for sensorless applications such as EVs, where reliability and safety during starting from standstill is essential, utilising this scheme can be hazardous.

By exploiting the similarity of AC motors [69] has proposed two sensorless schemes; a rotor flux estimator and a phase locked loop (PLL). Both schemes can be employed as a sensorless USC scheme and are derived from the voltage model equation. The PLL estimator was experimentally tested on an IM and a SPMSM. Results show that the estimated speed from the IM closely tracks the measured speed right through the field weakening region. Although tests for the PLL on SPMSM were only carried out in the medium speed region, it demonstrates a stable estimation. In order to employ this scheme for SPMSM, the d-axis current is required to be set to a value bigger than zero. As both proposed sensorless schemes are fundamentally model based in nature, they automatically inherit instability issues in zero and low speed regions, e.g. sensitivity to parameter variation and state un-observability.

Boldea et al. [70], by generalising schemes presented in [71-73], have also presented a USC scheme, based on active flux or torque-producing flux concept. The scheme takes advantage of combining a rotor flux observer, equipped with a compensator, and a PLL mechanism to estimate the speed and position. The scheme was experimentally tested on an IPMSM. Tests included; ±1 rpm speed reversal followed by full-load transients and ±4000 rpm speed reversal, including the field weakening region. Although utilising this scheme in low and medium speed regions provides an accurate speed estimation, the error between the estimated and measured speeds, in high speed regions, becomes very large at a region of 300 rpm. This can cause instability in high speed regions. In addition, this scheme on its own is not capable of performing a reliable starting from standstill, especially for PMSMs. This is because the exact position of the magnet and its polarity cannot be detected when using this scheme for starting from standstill.

## 2.6 Sensorless control for EV applications

Regarding the sensorless control for EV applications, a sensorless scheme which is capable of performing reliably from standstill and over a wide range of speeds, whilst remaining robust against motor parameter variation, is required. In this section sensorless schemes which have been specifically developed for EV applications are reviewed.

In [74], a sensorless scheme for an IM, based on the rotor flux vector calculation has been developed for EV applications. The scheme utilises an online rotor resistance calculation to reduce the sensitivity of the speed estimator to this parameter. The scheme has been tested using simulation and experimental setup. From the experimental results, shown for the proposed scheme, it is clear that the speed estimator closely tracks the measured speed up to the rated speed of the IM. However, above the rated speed, the estimated speed fluctuates, introducing ripples on the torque. These torque ripples gets magnified further when the motor is coupled to a gearbox. This scheme is also dependent on the magnetising inductance value. This value can vary by 50% which can cause instability, however, this has not been considered by the authors.

In [75], utilising an Is-MRAS, a sensorless control has been developed for an IM based on direct torque control (DTC) for traction applications. The scheme has been experimentally tested and results show when nominal parameters of the motor are used, a good speed tracking approximately twice the base speed (3834 rpm) can be achieved. Moreover, by utilising the DTC with the space vector modulation a fast torque response to load torque can be achieved. However, it has not been tested against motor parameter variation which can be the shortcomings of this scheme. Authors in [76] have also implemented a sensorless control based on the DTC for EV applications. In order to implement this scheme a rotor flux estimator, in the stationary reference frame, and a torque estimator are required. The estimated speed is calculated using the rotor flux components. From the simulation results is clear that the estimated speed is in good agreement with the measured speed, up to 1900 rpm. However, this scheme suffers from high torque ripple and current distortion, especially in the steady state operation. The scheme is also sensitive to the motor parameter variation, which can degrade the accuracy of the rotor flux estimator.

In another attempt, authors in [77] have developed a sensorless control for an IM, also based on Is-MRAS, using direct RFOC for EV applications. In order to estimate the stator current components a deterministic full order observer is used for the rotor flux estimation. The scheme has been validated using quasi-experimental methodology. Results show that this scheme provides a reasonable performance in constant torque region, when the nominal motor

parameters are used. However, authors have not commented on the sensitivity of the scheme to the motor parameter variation and its performance during the field weakening region.

Farasat and Karaman [78] have proposed a speed sensorless control of an IM for EV applications using hybrid FOC and DTC. Combining the FOC and DTC allows the electric motor drive to benefit from the advantages of both methods. However, utilising this scheme increases the complexity of the drive as the flux, torque and speed of the motor are required to be estimated. The proposed scheme has been tested using simulation. From results, e.g. shown in Fig 2-b, it can be seen that in the field weakening region the developed torque of the IM has considerable amount of ripples, which can cause the sensorless control to become unstable. In another attempt authors, in [79], have used an EKF for sensorless control of EV applications. This scheme is also based on the combination of the FOC and DTC. The scheme has only been verified using simulation. From results it is clear that the developed scheme is sensitive to the stator resistance variation, especially below 25 rad/sec when the stator resistance value is increase by 75% of its nominal value.

In [80], a sensorless scheme based on the RF-MRAS has been developed, using IFOC, for EV applications. The scheme has been tested using simulation. The results show that in medium speed regions the RF-MRAS demonstrates a good performance. However, as the author has also concluded in the paper that using the RF-MRAS for EV applications requires that the scheme undergo a lot of improvements. The main required improvements are; robustness against sensitivity to motor parameter variations and reliability in zero and low speed regions which have also been mentioned earlier in this chapter. In [81], also based on the RF-MRAS, a sensorless scheme has been developed for EV application. In order to overcome problems associated with the stator resistance variation, a stator resistance estimator is also implemented. The scheme has been verified using simulation and experimentally. From the recorded results it is clear that using this scheme resolves issues due to the stator resistance variation. However, instability in zero and low speed regions and problems due to pure integration still remained unsolved.

Patel et al. [82] have proposed a hybrid sensorless scheme for an IPM traction drive of EV applications. The HFSI scheme in this paper is based on the rotating carrier signal injection in the stationary reference frame. For medium and high speed regions the rotor position has been estimated using an open-loop stator flux observer. To implement this scheme a magnet polarity detection is required. This scheme has been experimentally tested and results show that using this scheme a robust dynamic performance can be achieved at 4000 rpm while 100% load is applied. However, this scheme uses a hard-switching mechanism for transition between HFSI and back-EMF schemes, which can cause torque ripple. Moreover, integrating the stator voltage

components using an open-loop approach can lead to instability, especially in the field weakening region.

In [83] a sensorless torque control using the sliding mode flux and speed observer has been developed for EV applications. The scheme has been validated using simulation and experimentally implemented on an actual EV. Tests included acceleration and deceleration of the vehicle from 30 rad/sec to 80 rad/sec and back to 30 rad/sec. It is clear that using the proposed scheme the estimated speed closely tracks the measured speed. However, the estimated speed is required to be calculated from the derivative of the rotor flux angle, which can cause speed ripple. To deal with this issue a LPF is required which in return causes delay on the estimated speed. Moreover, the performance of the vehicle in zero and low speed regions and sensitivity to the motor parameter variation have not been studied which can be the main shortcomings of this scheme.

Almost all of the above schemes suffer from motor parameter variation. The schemes based on DTC suffer from torque and current ripples which are not desirable to be used in EV applications. In addition, the above sensorless schemes are normally designed for a specific type of motor and cannot be employed as a universal sensorless scheme. Moreover, none of the reviewed sensorless schemes for EV application are capable of offering the following characteristics at once. These are:

- To be computationally easy to implement
- Robustness against motor parameter variation
- Provides a smooth torque control
- Reliable in starting from standstill
- Capable of performing in a wide range of speeds
- Being universally implementable for different types of motors

Therefore, from reviewing the above papers, one can conclude that there is a gap for more research in the area of sensorless control for EV applications.

## 2.7 Conclusion

Considering different aspects of the sensorless concept a comprehensive literature review has been provided and concludes the following:

a) The back-EMF MRAS is the most suitable candidate among MRAS schemes for use in the *limp-home* mode operation of EV application, powered by an IM. However, in order to employ this scheme, it requires some modification to improve its performance,

specifically against parameter variation, inverter nonlinearities and digitisation in high speed regions.

b) HFSI schemes are found to be more suitable for zero and low speed regions.

c) Regarding sensorless control of PMSMs, hybrid schemes provide a more effective solution.

d) The use of universal schemes promote the reduction in computational complexity of the overall sensorless drive when used on AC motors.

e) From the reviewed literature, it is clear that there is a gap for further research in the development of sensorless schemes capable of meeting the requirements of EV applications. Therefore, the main focus of this thesis is to fill in this gap by designing sensorless schemes suitable for EV applications.

# CHAPTER 3. SENSORLESS CONTROL BASED ON INDIRECT ROTOR-FIELD ORIENTED CONTROL FOR EV APPLICATIONS - MATHEMATICAL MODELLING

## 3.1 Introduction

For high performance applications, such as EV and HEV, TCDs are usually employed and several TCD approaches have been presented in literature [84-89]. Although these approaches have different structures, in most cases an estimated torque feedback loop is employed. This is used for the calculation of the stator current reference on the q-axis. The accuracy of the estimated feedback signal plays a major role in the stability of vehicle-starting from standstill and in low speed regions. Without accurate feedback, the torque control becomes very difficult and results in halt mode or a jerky-start situation. In order to achieve a high

dynamic operation in torque controlled drives two main techniques are normally employed, which are; field oriented control and DTC. One of the main disadvantages of the DTC is high ripple levels in the current and torque [84, 90, 91]. As far as EVs are concerned, these torque distortions at very low speeds create an undesirable cogging effect, when the vehicle is pulling away. When the electric motor is coupled to a gearbox, torque ripple can excite gearbox oscillations which are very hard to dampen out. Therefore, field oriented control can arguably be more suited control scheme for EV applications.

This chapter includes four parts: the first part presents mathematical modelling of the IM and SPMSM, the second part presents principles of the indirect rotor field oriented control for the IM, the third part shows principles of the conventional back-EMF model reference adaptive system for the IM, and the final part describes the sensorless control of an AC motor using a high frequency signal injection technique.

## 3.2 Mathematical modelling of the induction and surface-mounted permanent magnet synchronous motors

### 3.2.1 Mathematical modelling of induction motor

The space vector representatives of the stator and rotor voltage equations of an IM, can be expressed as follows:

$$\overline{v}_s^s = R_s \overline{i}_s^s + p\overline{\psi}_s^s \tag{3.1}$$

$$\overline{v}_r^r = R_r \overline{i}_r^r + p\overline{\psi}_r^r \tag{3.2}$$

where the subscripts “s “and “r” indicate the stator and rotor quantities, respectively. Meanwhile, the superscript “s” and “r” indicate that variables are in the stationary and the rotor reference frames, respectively.

From (3.1) and (3.2) it can be seen that the time derivation of the flux linkages and voltage drops due to resistances, yield voltage equations. The stator and rotor flux linkages in the stationary reference frame can be written as:

$$\overline{\psi}_s^s = L_s \overline{i}_s^s + L_m \overline{i}_r^s \tag{3.3}$$

$$\overline{\psi}_r^s = L_r \overline{i}_r^s + L_m \overline{i}_s^s \tag{3.4}$$

As it can be seen, (3.3) and (3.4) consist of two components which are as a result of the stator and rotor current contributions. To express (3.2) with respect to the rotor linkage flux in the stationary reference frame, (3.2) is transformed into the stationary reference frame:

$$\overline{v}_r^s = R_r \overline{i}_r^s + p\overline{\psi}_r^s - j\omega_r \overline{\psi}_r^s \tag{3.5}$$

As the rotor bars' circuits are being shorted $\overline{v}_r^s = 0$, hence, (3.5) can be rewritten as:

$$p\overline{\psi}_r^s = -R_r \overline{i}_r^s + j\omega_r \overline{\psi}_r^s \tag{3.6}$$

By rearranging (3.4) for the rotor current vector ($\overline{i}_r^s$), we have:

$$\overline{i}_r^s = \frac{1}{L_r}(\overline{\psi}_r^s - L_m \overline{i}_s^s) \tag{3.7}$$

and by substituting (3.7) in (3.6), (3.6) becomes:

$$p\overline{\psi}_r^s = \frac{L_m}{T_r}\overline{i}_s^s - \frac{1}{T_r}\overline{\psi}_r^s + j\omega_r \overline{\psi}_r^s \tag{3.8}$$

where $T_r = \frac{L_r}{R_r}$ is the rotor time constant.

Similarly by implementing (3.7) into (3.3), we have the stator flux linkage expressed with respect to the rotor linkage flux, which is as follows:

$$\overline{\psi}_s^s = \left(L_s - \frac{L_m^2}{L_r}\right)\overline{i}_s^s + \frac{L_m}{L_r}\overline{\psi}_r^s \tag{3.9}$$

Implementing (3.9) in (3.1), (3.1) can also be expressed with respect to the rotor flux linkage, which is as follows:

$$\overline{v}_s^s = (R_s + pL_s')\overline{i}_s^s + \overline{e}_m \tag{3.10}$$

Where; $L_s' = L_s\left(1 - \frac{L_m^2}{L_s L_r}\right) = L_s\sigma$. Where; $\sigma$ is the leakage coefficient.

Note that $\overline{e}_m = \frac{L_m}{L_r} p\overline{\psi}_r^s$ is the back-EMF term in the stationary reference frame.

Expressing an IM in a state space model provides a reasonable solution for control problems using simulation software. Therefore, using (3.8) and (3.10) the IM state space representation can be expressed with the stator current and the rotor flux linkage components in the stationary reference frame as state variables. Thus, we have:

$$\begin{bmatrix} pi_{s\alpha} \\ pi_{s\beta} \\ p\psi_{r\alpha} \\ p\psi_{r\beta} \end{bmatrix} = \begin{bmatrix} -\xi & 0 & \frac{\eta}{T_r} & \eta\omega_r \\ 0 & -\xi & -\eta\omega_r & \frac{\eta}{T_r} \\ \frac{L_m}{T_r} & 0 & -\frac{1}{T_r} & -\omega_r \\ 0 & \frac{L_m}{T_r} & \omega_r & -\frac{1}{T_r} \end{bmatrix} \begin{bmatrix} i_{s\alpha} \\ i_{s\beta} \\ \psi_{r\alpha} \\ \psi_{r\beta} \end{bmatrix} + \begin{bmatrix} \frac{1}{L'_s} & 0 \\ 0 & \frac{1}{L'_s} \\ 0 & 0 \\ 0 & 0 \end{bmatrix} \begin{bmatrix} v_{s\alpha} \\ v_{s\beta} \end{bmatrix} \quad (3.11)$$

where: $\xi = \frac{R_s}{L'_s} + \frac{L^2 m}{L'_s L_r \tau_r}$, and $\eta = \frac{L_m}{L'_s L_r}$.

The stator voltage equation (3.1) can also be presented in the synchronous reference frame. The synchronous reference frame rotates at the same speed as the synchronous angular velocity ($\omega_e$).

$$\theta_e = \int \omega_e \, dt = \int (\omega_{sl} + \omega_r) dt \quad (3.12)$$

By multiplying both sides of (3.1) and (3.5) with the term $e^{-j\theta_e}$, (3.1) and (3.5) can be transformed from the stationary to the synchronous reference frame respectively, as given below:

$$\overline{v}_s^e = R_s \overline{i}_s^e + p\overline{\psi}_s^e + j\omega_e \overline{\psi}_s^e \quad (3.13)$$

$$\overline{v}_r^e = R_r \overline{i}_r^e + p\overline{\psi}_r^e + j\omega_{sl} \overline{\psi}_r^e \quad (3.14)$$

where superscript “e” indicates that variables are in the synchronous reference frame.

Comparing (3.13) with (3.14), it can be seen that $\omega_{sl}$ = ($\omega_e - \omega_r$), which is the slip angular velocity, has appeared in (3.14) instead of ($\omega_e$).

The stator and rotor flux linkages (3.3) and (3.4) in the stationary reference frame can also be expressed in the synchronous reference frame, as given below:

$$\overline{\psi}_s^e = L_s \overline{i}_s^e + L_m \overline{i}_r^e \quad (3.15)$$

$$\overline{\psi}_r^e = L_r \overline{i}_r^e + L_m \overline{i}_s^e \quad (3.16)$$

By substituting (3.15) and (3.16) into (3.13) and (3.14), respectively, the IM synchronous model can be expressed with currents as state variables:

$$\begin{bmatrix} v_{sd}^e \\ v_{sq}^e \\ 0 \\ 0 \end{bmatrix} = \begin{bmatrix} R_s + pL_s & -\omega_e L_s & pL_m & -\omega_e L_m \\ \omega_e L_s & R_s + pL_s & \omega_e L_m & pL_m \\ pL_m & -\omega_{sl} L_r & R_r + pL_r & -\omega_{sl} L_r \\ \omega_{sl} L_r & pL_m & \omega_{sl} L_r & R_r + pL_r \end{bmatrix} \begin{bmatrix} i_{sd}^e \\ i_{sq}^e \\ i_{rd}^e \\ i_{rq}^e \end{bmatrix} \quad (3.17)$$

Equation (3.13) can be represented with respect to the rotor flux linkage and the stator current vectors in the synchronous reference frame. This is achieved firstly by transforming (3.9) from the stationary to the synchronous reference frame:

$$\overline{\psi}_s^e = \left(L_s - \frac{L_m^2}{L_r}\right)\overline{i}_s^e + \frac{L_m}{L_r}\overline{\psi}_r^e \quad (3.18)$$

and then, by substituted (3.18) into (3.13), (3.13) becomes:

$$\overline{v}_s^e = (R_s + pL_s')\overline{i}_s^e + \frac{L_m}{L_r}p\overline{\psi}_r^e + j\omega_e(L_s'\overline{i}_s^e + \frac{L_m}{L_r}\overline{\psi}_r^e) \quad (3.19)$$

The electromagnetic torque for the IM with several pole pairs (PP) can be written as follows:

$$T_{em} = \frac{3}{2}PP\frac{L_m}{L_r}(\overline{\psi}_r^e \otimes \overline{i}_s^e). \quad (3.20)$$

Where, $\otimes$ is the cross product sign.

### 3.2.2 Mathematical modelling of Surface-mounted PMSM

The SPMSM is a non-salient motor which means that the inductance on the direct and the quadrature axes are equal ($L_d = L_q = L_s$). The dynamic equations of the SPMSM in the synchronous reference frame are derived as follows:

The stator flux linkage of a SPMSM in the stationary reference frame can be written as below:

$$\overline{\psi}_s^s = L_s\overline{i}_s^s + \psi_{PM}e^{j\theta_e} \quad (3.21)$$

Hence, by considering (3.21), the stator voltage equation of the SPMSM in the stationary reference frame can be written as:

$$\overline{v}_s^s = (R_s + pL_s)\overline{i}_s^s + j\omega_e\psi_{PM}e^{j\theta_e} \quad (3.22)$$

The stator voltage equation (3.22) can also be expressed in the synchronous reference frame. This is achieved by multiplying both sides of (3.22) by the term ($e^{-j\theta_e}$). This yields:

$$\overline{v}_s^e = (R_s + pL_s)\overline{i}_s^e + j\omega_e L_s \overline{i}_s^e + j\omega_e \psi_{PM}. \tag{3.23}$$

Note that the term ($j\omega_e L_s \overline{i}_s^e$) is decoupling term and the term ($j\omega_e \psi_{PM}$) is the back-EMF in the synchronous reference frame which only appears on the q-axis.

In the normal differential equation form, the SPMSM dynamic equations in the synchronous reference frame can be expressed as below:

$$\begin{bmatrix} pi_d^e \\ pi_q^e \end{bmatrix} = \begin{bmatrix} -\frac{R_s}{L_s} & \omega_e \\ -\omega_e & -\frac{R_s}{L_s} \end{bmatrix} \begin{bmatrix} i_d^e \\ i_q^e \end{bmatrix} - \frac{\omega_e \psi_{PM}}{L_s} \begin{bmatrix} 0 \\ 1 \end{bmatrix} + \frac{1}{L_s} \begin{bmatrix} v_d^e \\ v_q^e \end{bmatrix}. \tag{3.24}$$

## 3.3 Principle of indirect rotor-field oriented control

Depending on the nature of the reference frame alignment, the field oriented control concept can be divided into three main techniques, which are:

1) Rotor field oriented control (RFOC)
2) Stator field oriented control (SFOC)
3) Airgap field oriented control (airgap-FOC)

RFOC is the most common technique and divides further into two approaches; direct and indirect. The direct approach requires the rotor flux components to be estimated or measured by using a flux sensing coil or Hall sensors. The rotor flux can be estimated, from the stator flux and current components in the stationary reference frame, using (3.9). Utilising the flux sensor is not a convenient approach due to armature reaction, space limitation, and noise [92]. However, the indirect approach does not require any flux estimation or sensor. The rotor flux angle can be indirectly calculated, from the measured speed and slip. In the RFOC the rotor flux is aligned with the d-axis in the synchronous reference frame, which is shown in Fig. 3.1. Consequently, the rotor flux components can be written as follows:

$$\begin{aligned} &\overline{\psi}_r^e = \psi_{rd}^e \\ &\psi_{rq}^e = 0, \qquad p\psi_{rq}^e = 0 \end{aligned} \tag{3.25}$$

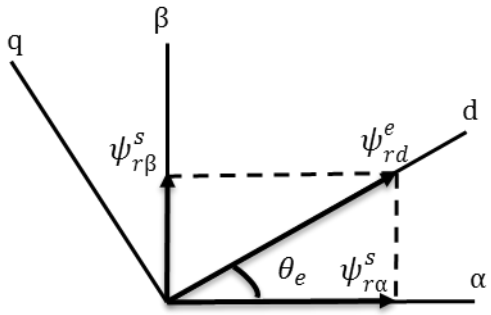


**Fig. 3.1. Vector diagram representation of the Rotor flux in the rotor field oriented control.**

By applying the rotor field orientation conditions in (3.25) into (3.19), the stator voltage components' equations in the synchronous reference frame become:

$$v_{sd}^e = (R_s + pL_s')i_{sd}^e - \omega_e L_s' i_{sq}^e + \frac{L_m}{L_r} p\psi_{rd}^e \tag{3.26}$$

$$v_{sq}^e = (R_s + pL_s')i_{sq}^e + \omega_e L_s' i_{sd}^e + e_{mq}^e \tag{3.27}$$

where, $e_{mq}^e = \omega_e \frac{L_m}{L_r}\psi_{rd}^e$ is the back-EMF term in the synchronous reference frame. Note that this term only appears on the q-axis.

The slip angular velocity can be calculated by employing the rotor field orientation conditions. This is achieved first by transforming (3.7) from the stationary to the synchronous reference frame and then applying conditions (3.25) into (3.7). This yields:

$$\begin{aligned} i_{rd}^e &= \frac{1}{L_r}(\psi_{rd}^e - L_m i_{sd}^e) \\ i_{rq}^e &= -\left(\frac{L_m}{L_r} i_{sq}^e\right) \end{aligned} \tag{3.28}$$

By substituting (3.28) for the rotor voltage components in (3.14), (3.14) becomes:

$$\begin{aligned} 0 &= \frac{1}{T_r}(\psi_{rd}^e - L_m i_{sd}^e) + p\psi_{rd}^e \\ 0 &= -\frac{L_m}{T_r} i_{sq}^e + \omega_{sl}\psi_{rd}^e \end{aligned} \tag{3.29}$$

Therefore, from the q-axis component of (3.14) the slip angular velocity can be calculated, which is as follows:

$$\omega_{sl} = \frac{L_m i_{sq}^e}{T_r \psi_{rd}^e} \tag{3.30}$$

By considering steady state condition, where $p\psi_{rd}^e = 0$, the d-axis component of (3.29) can be rewritten as follows:

$$\psi_{rd}^e = L_m i_{sd}^e \tag{3.31}$$

by applying (3.31) in (3.30), the slip angular velocity can be rewritten as below:

$$\omega_{sl} = \frac{i_{sq}^e}{T_r i_{sd}^e} \tag{3.32}$$

Hence, the rotor flux angle ($\theta_e$) can be expressed as:

$$\theta_e = \int (\frac{i_{sq}^e}{T_r i_{sd}^e} + \omega_r) dt \tag{3.33}$$

Applying the rotor field orientation conditions into the electromagnetic torque equation of the IM (3.20), we have:

$$T_{em} = \frac{3}{2}\, PP \frac{L_m}{L_r} \psi_{rd}^e\, i_q^e. \tag{3.34}$$

The block diagram of TCD of the IM based on IRFOC used in EV applications is shown in Fig. 3.2. The electromagnetic torque is applied using an accelerator pedal by the driver of the EV. By rearranging (3.34), the reference q-axis current ($i_q^*$), the torque producing current, is calculated. Usually, under rated base speed, for the sake of mathematical simplicity, the value of the reference d-axis current ($i_d^*$), the flux producing current, is kept to a constant value. However, this approach is not as energy efficient as when a Lookup Table (LUT) is employed. Utilising a LUT provides maximum torque per ampere (MTPA) with a fast dynamic torque response [93]. Therefore, in EV applications the value of the reference d-axis current is extracted using a LUT. The rotor flux angle, (3.33), is calculated from summation of the rotor speed, measured from an encoder, and the slip angular velocity.

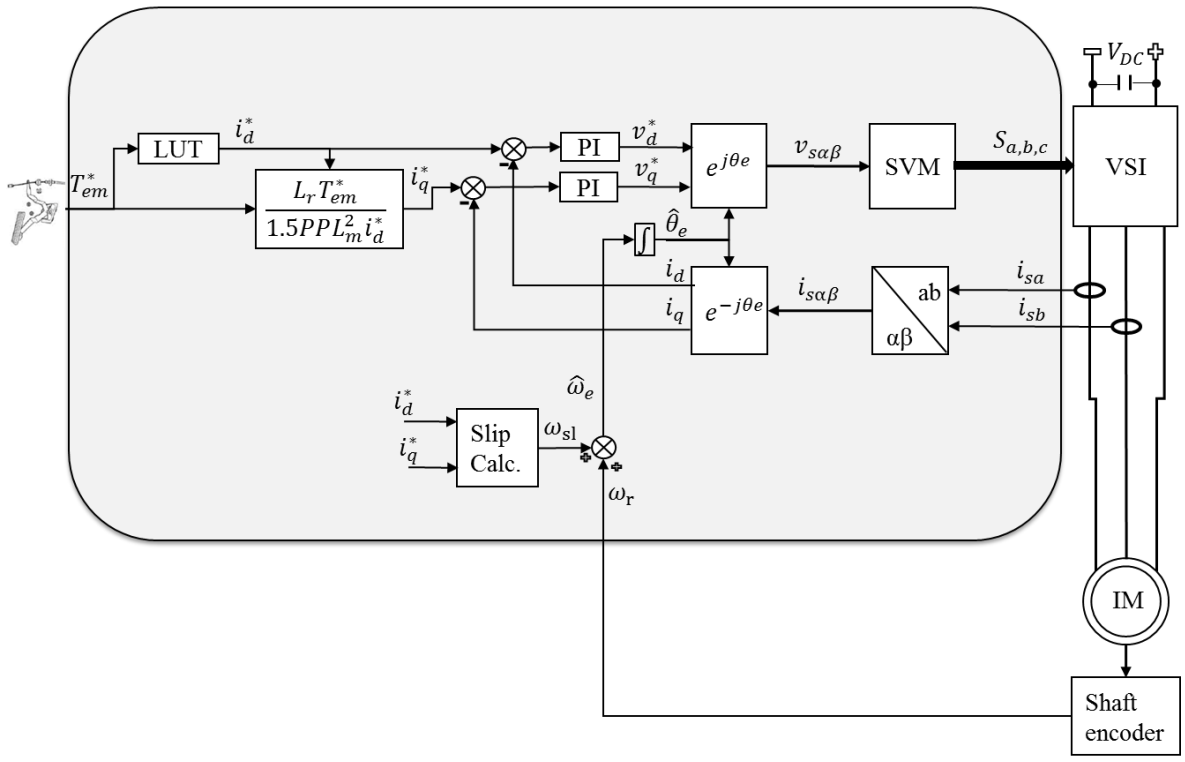


**Fig. 3.2. Block diagram of torque-controlled drive of the IM based on the IRFOC used in EV applications (with speed sensor).**

The electromagnetic torque equation for the SPMSM ($\psi_{rd}^e = \psi_{PM}$), can be written as below:

$$T_{em} = \frac{3}{2} PP\, \psi_{PM}\, i_q^e. \tag{3.35}$$

The block diagram of the TCD of the SPMSM based on IRFOC used in EV applications is shown in Fig. 3.3. Unlike IRFOC for the IM drive, the SPMSM drive does not require any slip calculation. Hence, the rotor flux angle is calculated from the measured synchronous speed from a shaft encoder. The reference q-axis current is calculated by rearranging the electromagnetic torque equation (3.35). The reference d-axis current is also extracted from a LUT with $i_d^*$ kept at zero within the rated speed region.

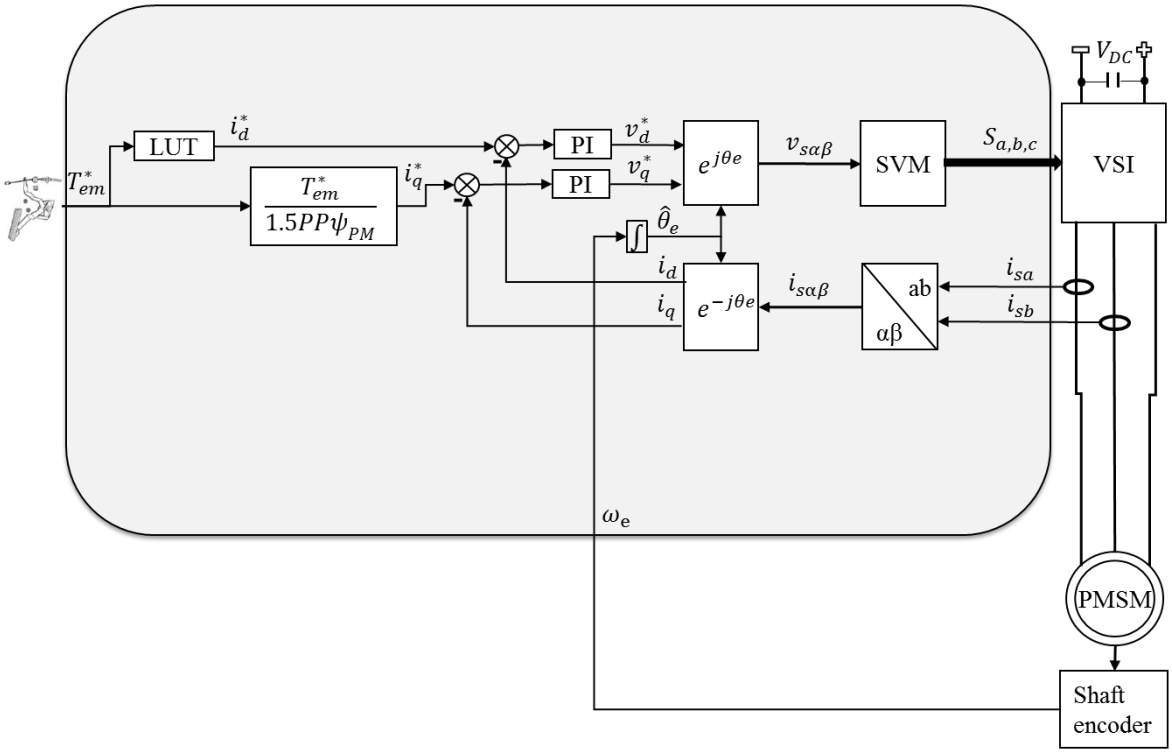


**Fig. 3.3. Block diagram of the torque-controlled drive of a SPMSM based on IRFOC used in EV applications (with speed sensor).**

## 3.4 Principles of Model Reference Adaptive System for Induction Motor

The block diagram of the conventional back-EMF MRAS [20] used for the speed estimation of the IM is shown in Fig. 3.4. It consists of a reference model, which is independent from the estimated speed, an adjustable model, which gets updated by the estimated speed, and an adaptation mechanism. The principle of the conventional MRAS is based on driving the error, which is obtained from the cross product of the reference and estimated vectors ($\overline{e}_{mR}^*$ and $\overline{e}_{mA}^{\wedge}$, respectively), to zero. The scheme is stable when the angle between the reference and the estimated vectors is kept as small as possible between ±90 degrees, for forward and reverse mode of operations, respectively. If the angle increases beyond 90 degrees, e.g. due to sudden full torque injection in the speed mode operation, this scheme can become unstable. In regenerative braking, the vectors are suddenly swapped around and the direction of the angle changes from positive to negative which can also cause instability, especially in the case of the RP-MRAS schemes [28].

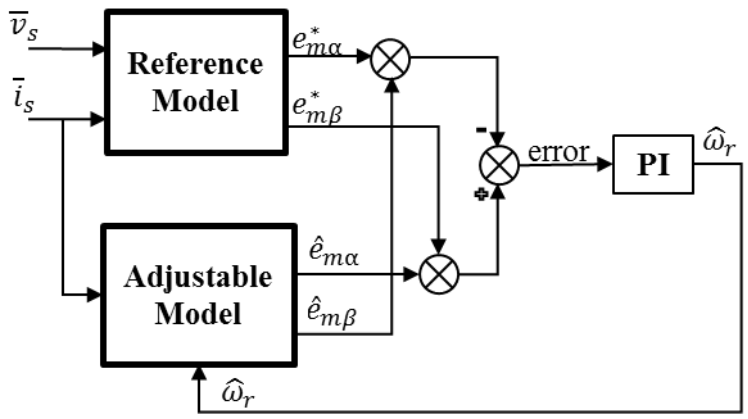


**Fig. 3.4. Block diagram of the conventional back-EMF MRAS [20].**

The reference model, based on stator equation (3.10), takes in the reconstructed stator voltage and current components in the stationary reference frame and in return provides the back-EMF reference components in the stationary reference frame [20], which are given below:

$$\begin{aligned} e^*_{m\alpha} &= v_{s\alpha} - (R_s + pL'_s)i_{s\alpha} \\ e^*_{m\beta} &= v_{s\beta} - (R_s + pL'_s)i_{s\beta} \end{aligned} \tag{3.36}$$

The adjustable model takes in the stator current and estimated speed and in return provides the estimated back-EMF components in the stationary reference frame [20]. The estimated components are calculated based on the rotor equation (3.8), which are written as below:

$$\begin{aligned} \hat{e}_{m\alpha} &= \frac{L_m}{L_r}\, p\psi^s_{r\alpha} = \frac{L_m}{L_r}\frac{(L_m i_{s\alpha} - \psi^s_{r\alpha} - \omega_r T_r \psi^s_{r\beta})}{T_r} \\ \hat{e}_{m\beta} &= \frac{L_m}{L_r}\, p\psi^s_{r\beta} = \frac{L_m}{L_r}\frac{(L_m i_{s\beta} - \psi^s_{r\beta} + \omega_r T_r \psi^s_{r\alpha})}{T_r} \end{aligned} \tag{3.37}$$

In order to design the adaptation mechanism for MRAS hyperstability concept is used [19, 20]. This concept helps to ensure the overall system will be stable and that the estimated value will converge to its desired value. Therefore, the aim is first to derive an error state equation. This is achieved by subtracting the reference and estimated components from each other, which is as follows [20]:

$$p\overline{\epsilon} = A\overline{\epsilon} - W \tag{3.38}$$

where, $\overline{\epsilon} = (\bar{e}^*_m - \overline{\hat{e}}_m)$ is the error vector, $A = \begin{bmatrix} -\frac{1}{T_r} & -\omega_r \\ \omega_r & -\frac{1}{T_r} \end{bmatrix}$, and $W = (\omega_r - \hat{\omega}_r)\begin{bmatrix} \hat{e}_{m\beta} \\ -\hat{e}_{m\alpha} \end{bmatrix}$

Then by letting

$$\widehat{\omega}_r = \Phi_2([\epsilon]) + \int \Phi_1([\epsilon])dt \tag{3.39}$$

and solving by applying Popov's criterion, a suitable candidate for the adaptation mechanism can be found. Popov's criterion requires that

$$\int_0^{t_1} [\overline{\epsilon}]^T . [W]dt \geq -\gamma_0^2 \qquad for\ all\ t_1 \geq 0 \tag{3.40}$$

where $\gamma_0^2$ is a positive constant.

Substituting for $\epsilon$ and $W$ from (3.38) into (3.40), and using the definition of $\widehat{\omega}_r$ in (3.39), we have:

$$\int_0^{t_1} \left\{ \left(\epsilon_\alpha \hat{e}_{m\beta} - \epsilon_\beta \hat{e}_{m\alpha}\right)(\omega_r - \Phi_2([\epsilon]) - \int \Phi_1([\epsilon])dt) \right\} dt \geq -\gamma_0^2 \tag{3.41}$$

By solving (3.41), using the following well known equation [19, 20]

$$\int_0^{t_1} \dot{f}(t)\,.\,k_2 f(t)\,dt \geq -\frac{k_2}{2} f^2(0), k_2 > 0. \tag{3.42}$$

The Popov's integral inequality (3.40) can be satisfied by letting $\Phi_1$ and $\Phi_2$ in (3.39) be as follows:

$$\begin{aligned} \Phi_1 &= k_2\left(\hat{e}_{m\alpha} e^*_{m\beta} - e^*_{m\alpha} \hat{e}_{m\beta}\right) \\ \Phi_2 &= k_1\left(\hat{e}_{m\alpha} e^*_{m\beta} - e^*_{m\alpha} \hat{e}_{m\beta}\right) \end{aligned} \tag{3.43}$$

where $k_1$ and $k_2$ are gains of the controller.

Hence, the adaptation mechanism (3.39), can be expressed as the following:

$$\widehat{\omega}_r = \left(k_p + \frac{K_i}{s}\right) * \left(\bar{\hat{e}}_{m\alpha\beta} \otimes \bar{e}^*_{m\alpha\beta}\right). \tag{3.44}$$

Where, $k_p$ and $K_i$ are proportional and integral gains, respectively.

## 3.5 Principles of High frequency signal injection

The HFSI scheme employed in this thesis is based on the synchronous injection method, which was originally proposed by Linke [94] and later reviewed by Holtz (Fig. 38) in [54]. This scheme requires a high frequency alternating carrier to be injected in the estimated d-axis

voltage. The principle of this scheme is to derive an error between the estimated (or assumed) and the actual rotor flux angle and force the error to zero using a PLL control structure, as shown in Fig. 3.5.

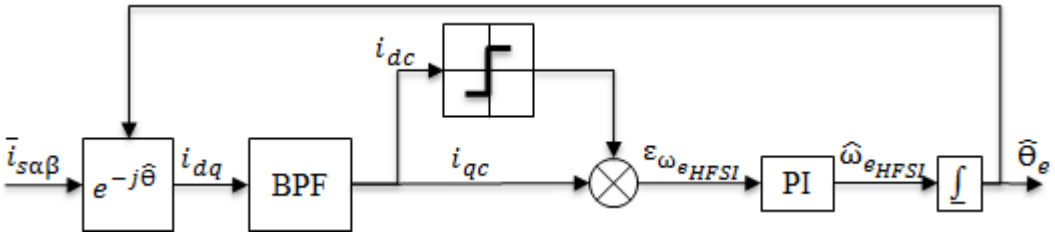


**Fig. 3.5. Signal flow diagram of the PLL mechanism used for demodulation of HFSI carrier [54].**

Thus, the objective is to obtain a signal, which directly represents the error angle ($\epsilon_{\omega_{e_{HFSI}}}$). In order to achieve that, an alternating carrier ($V_c$) at high frequency ($\omega_{inj}$) is injected in the estimated d-axis [54].

$$\begin{bmatrix} v_{dc} \\ v_{qc} \end{bmatrix} = \begin{bmatrix} V_c \cos(\omega_{inj} t) \\ 0 \end{bmatrix}. \tag{3.45}$$

Therefore, the error angle is obtained as it is given in [54].

$$i_{dqc} = BPF(I_{dq}) \tag{3.46}$$

$$\epsilon_{\omega_{e_{HFSI}}} = i_{qc} sign(i_{dc}) \tag{3.47}$$

The error angle signal is driven to zero by using a PI controller which outputs the estimated synchronous speed ($\hat{\omega}_{e_{HFSI}}$). The estimated rotor flux angle is then calculated by integrating the synchronous speed as shown in Fig. 3.5. The general block diagram of an AC motor drive based on the sensorless IRFOC using high frequency signal injection technique is shown in Fig. 3.6. A high frequency signal carrier is added to the estimated d-axis voltage ($v_d^*$). A LPF is required to cancel out high frequency signals on the measured d-axis current ($i_d$). The carrier signal does not appear on the q-axis, hence, it does not need to be low-pass filtered [54].

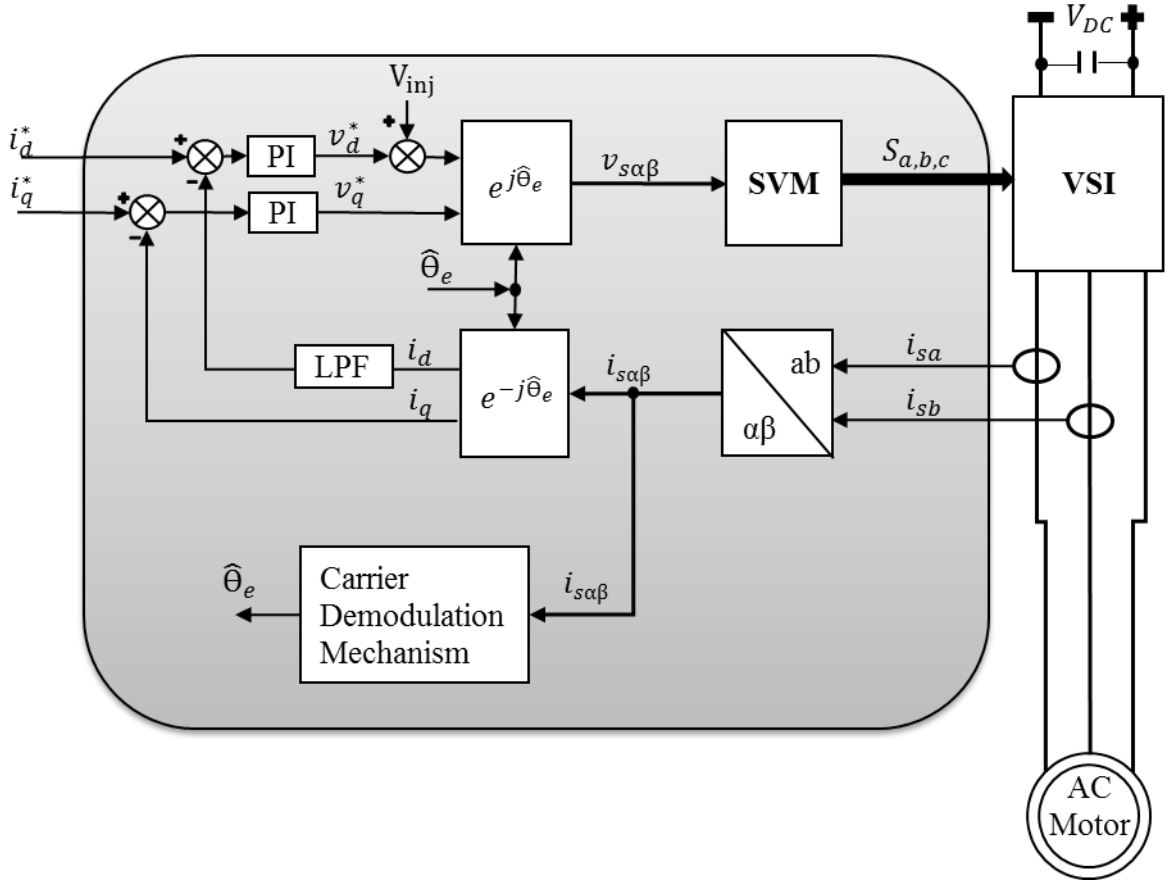


**Fig. 3.6. General block diagram of an AC motor drive based on the sensorless IRFOC using high frequency signal injection technique.**

## 3.6 Conclusion

This chapter included the description of the mathematical modelling of the IM and SPMSM. The principles of the IRFOC for the IM and SPMSM have been provided. Moreover, the principles of the conventional back-EMF MRAS for IM have also been given. Finally, the sensorless control of an AC motor using HFSI technique has been presented. This scheme is employed, in chapter 7, for universal sensorless control in zero and low speed regions.

The presented mathematical models of the electric motors and the concept of IRFOC are used for developing Matlab/Simulink models. These Simulink models, shown in the Appendix, have helped with verifying the proof of concepts in the following chapters.

# CHAPTER 4. THE EXPERIMENTAL SETUP

## 4.1 Introduction

In order to allow experimental implementation of the developed schemes in this project a test setup is required. This project has been sponsored by Sevcon Ltd. in Gateshead. Sevcon offers a wide range of products, such as controllers, DC/DC converters and battery charging systems, for on/off-road, marine and construction equipment.

The experiments were therefore carried out using the facilities and equipment provided by Sevcon. For this project, a back to back platform based on a 19 kW IM and a 10 kW SPMSM was designed and built, as both motors are currently used in the automotive industry for EV applications. The back to back arrangement includes two 72 V generation 4 Dragon8 controllers designed by Sevcon. The block diagram of the test bench and a photograph are shown in Fig. 4.1. A detailed description of the main components of the test bench are provided in the following sections. To further verify the proposed schemes in this project two electric golf buggies were used, their details are also presented.

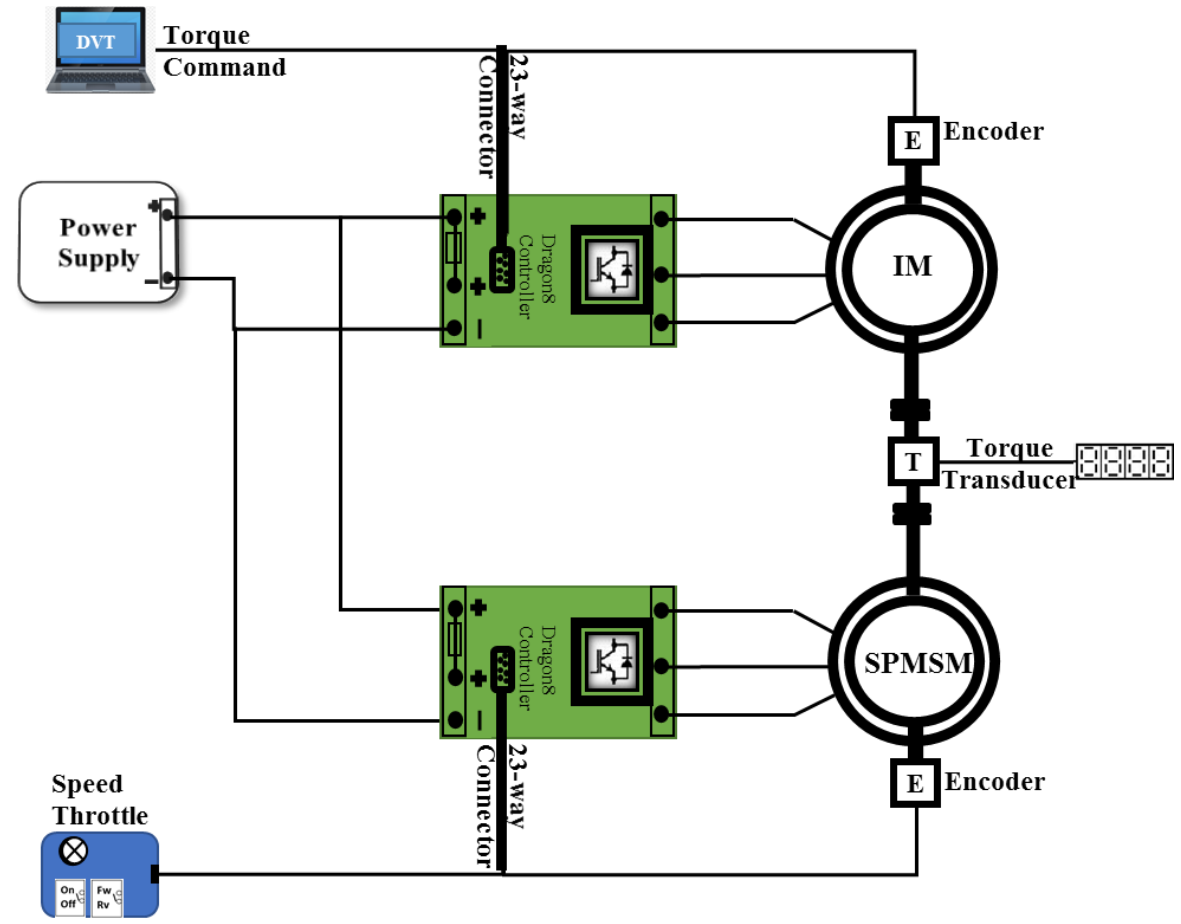


(a)

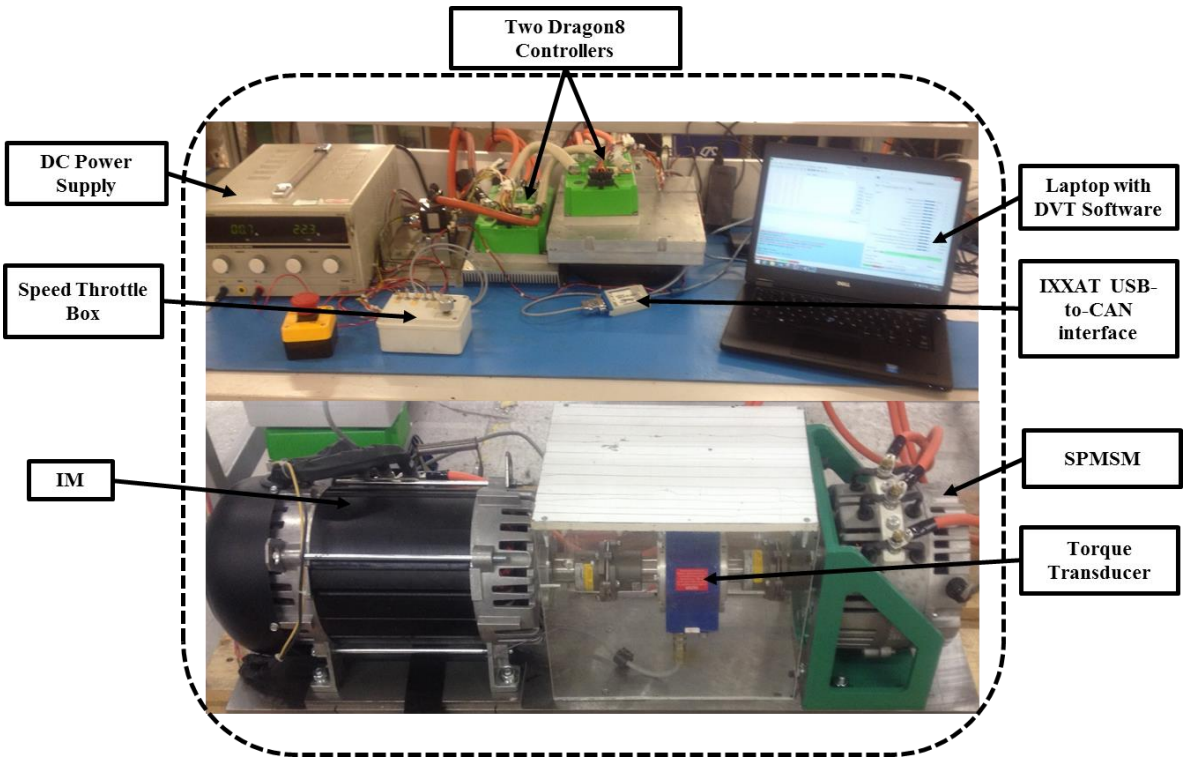


(b)

**Fig. 4.1. Experimental setup (a) block diagram (b) actual test bench.**

## 4.2 Dragon8 Controller

Dragon8 is an AC motor controller with 48 V to 96 V DC nominal battery voltage ranges, and maximum power of up to 35 kW. A photograph of the Dragon8 controller is shown in Fig. 4.2. This controller is compatible with IM, PMSM, or brushless DC motor. The controller includes up to 6 digital inputs and 4 analogue inputs. It also includes two dedicated 5 V and 10 V (both 200 mA) outputs. The Dragon8 controller contains a 32-bit floating point µ-processor. The controller has switching and sampling frequencies of 8 kHz and 16 kHz, respectively. It is capable of performing four quadrant control in speed and torque modes.


**Fig. 4.2. Photograph of the Dragon8 controller.**

## 4.3 The test bench setup

The test bench consists of a 19 kW star-connected three-phase IM, designed for use in EV applications, and a 10 kW SPMSM. The test rig also contains a 300 Nm torque transducer, used for validation, and two Sevcon (72 V) 29 kW Dragon8 controllers. The stator currents were measured using two Hall sensors which are built in to the controllers. In order to communicate with the controller on the IM, Device Communicator Tool (DVT) software was utilised. During the experiments, the rotor speed was varied using a speed throttle box connected to the controller which was controlling the SPMSM load machine, if the IM was under test. The D8 controller connected to the IM was set to the torque mode and the torque commands were applied using the DVT software on the laptop. A DC power supply was used to provide DC voltage to both controllers. The IM and SPMSM were equipped with an incremental Hall-Effect encoder (AB) and a Sine/Cos encoder, respectively. These were used for evaluation of the implemented sensorless approach (measured speed). The sensorless control algorithm was hand-coded in C-programming language and was compiled using "Keil" software development environment. Results of all the tests were recorded using the vehicle interface measurement tool which is built in the DVT software. The nominal parameters of the tested IM and SPMSM are provided in Table 4.1.

**Table 4.1. Nominal motor parameters of the motors on the dynamometer.**

| Parameter description | IM on Dyno. | SPMSM on Dyno. |
|---|---|---|
| **Power [kW]** | 19 | 10 |
| **Rated torque [Nm]** | 48 | 51 |
| **DC-link Voltage [V]** | 65 | 65 |
| **Rated stator current [A]** | 450 | 125 |
| **Pole pair** | 2 | 4 |
| **Stator Resistance [mΩ]** | 4.6 | 65.0 |
| **Stator Inductance [µH]** | 888.0 | 50.0 |
| **Magnetising induc. [µH]** | 855.0 | - |
| **Rotor Resistance [mΩ]** | 6.1 | - |
| **Rotor inductance [µH]** | 888.0 | - |
| **Torque constant [Nm/A]** | - | 0.12 |

## 4.4 Electric golf buggies

In order to demonstrate the performance of the proposed schemes presented in this thesis, two electric golf buggies have been used, which are shown in Fig. 4.3. Both vehicles have a single traction motor. One of the golf buggies, shown in Fig. 4.3-(a), is powered by 5 kW IM and is equipped with a Hall-Effect encoder (AB). The other golf buggy, shown in Fig. 4.3-(b), is powered by 5 kW SPMSM and is equipped with a UVW encoder. The speed from the encoder

was only used for validation which is labelled as the measured speed in the recorded results. All of the experimental tests using the golf buggies have been carried out on an indoor test track, which has an area of 35 m by 5 m. The test track includes a ramp which is used for the vehicle hill-starting tests.

(a)

(b)

**Fig. 4.3. Actual photographs of (a) the IM golf buggy, and (b) the SPMSM golf buggy.**

A general block diagram for both golf buggies is shown in Fig. 4.4. During the vehicles' test-drive, forward, park and reverse operation modes were manually selected using the vehicles' gear sticks and the torque command was applied using the accelerator pedal. Both buggies are equipped with the 48 V Dragon8 controller. A laptop was used to communicate with the controllers by using IXXAT USB-to-CAN interface. Both vehicles drive the rear wheels using a fixed ratio differential. During the tests using golf buggies, the estimated speed, from proposed schemes, and measured speed, from encoders, were compared. The nominal motor parameters of the motors on the golf buggies are shown in Table 4.2.

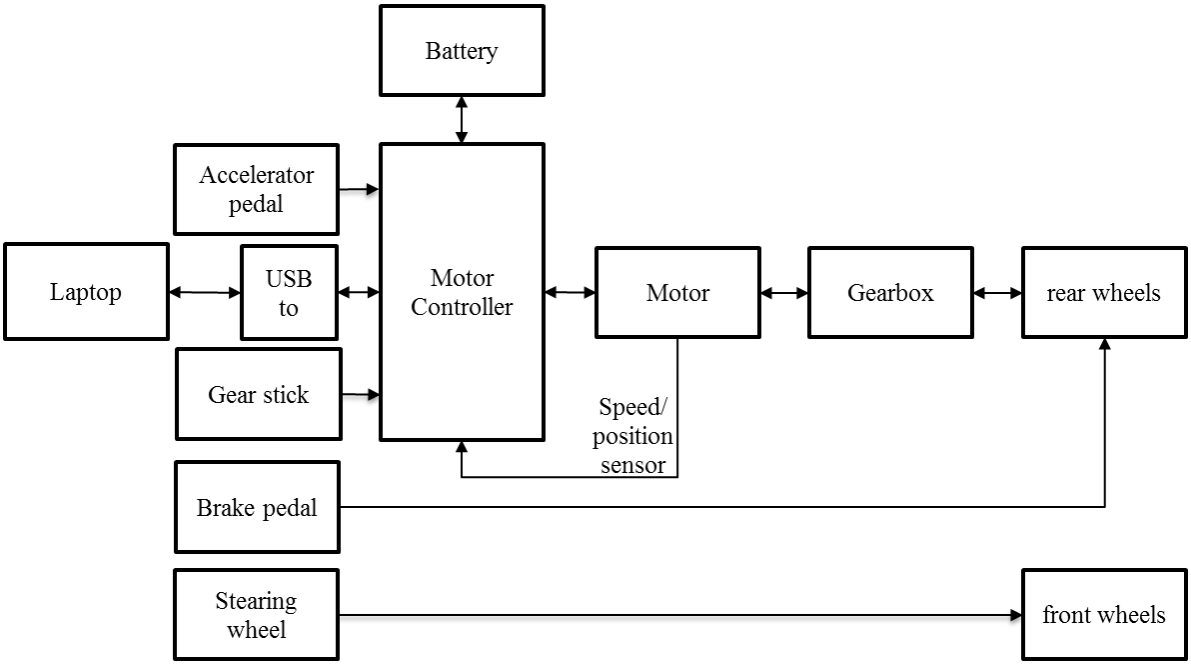


**Fig. 4.4. Block diagram of both golf buggies.**

**Table 4.2. Nominal motor parameters of the motors on the golf buggies.**

| Parameter description | IM on Golf buggy | SPMSM on Golf buggy |
|---|---|---|
| **Power [kW]** | 5 | 5 |
| **Rated torque [Nm]** | 22 | 38 |
| **DC-link Voltage [V]** | 48 | 48 |
| **Rated stator current [A]** | 138 | 100 |
| **Pole pair** | 2 | 4 |
| **Stator Resistance [mΩ]** | 10.24 | 13.0 |
| **Stator Inductance [µH]** | 850.3 | 100.0 |
| **Magnetising induc. [µH]** | 778.0 | - |
| **Rotor Resistance [mΩ]** | 4.45 | - |
| **Rotor inductance [µH]** | 850.3 | - |
| **Torque constant [Nm/A]** | - | 0.13 |

## 4.5 Conclusion

This chapter has presented the test setup and the electric golf buggies which have been used in this project. A full description of a dragon8 controller used in this thesis has been presented. The components of the experimental test setup have been listed and described. The golf buggies description and their block diagram have also been presented.

# CHAPTER 5. SENSORLESS CONTROL OF IM BASED ON BACK-EMF MRAS WITH COMPENSATING MECHANISM

This chapter presents a novel speed estimation scheme for IMs based on back-EMF MRAS. The scheme is employed for the purpose of sensorless TCD used in the *limp-home* mode operation in EV applications. A performance comparison was carried out between the proposed and conventional back-EMF MRAS schemes for starting from standstill, sensitivity to parameter variations and constant speed operation with load variations. Utilising the IM golf buggy, the behaviours of the new scheme was separately investigated for vehicle-starting from standstill, wide speed range including field weakening region and hill-starting operations. The proposed scheme is computationally easy to implement, robust against sensitivity to parameter variations and errors due to digitisation in the field weakening region. This scheme not only is consistent for vehicle-starting from standstill, it also provides a reliable vehicle-drive in the field weakening region and during vehicle hill-starting. The dynamometer and vehicle test-

drive results show the suitability of the proposed scheme for the purpose of EV fault tolerant *limp-home* mode operation.

## 5.1 Introduction

The conventional back-EMF MRAS scheme is computationally easy to implement, however, this scheme is sensitive to parameters variations. These variations can cause voltage errors between the stator reference and actual input voltages of IM. At very low speed, these errors can even become larger than the motor's stator voltage [43], which can have serious effect on the performance of the back-EMF MRAS in the low speed region. Moreover, digitisation effects can cause phase error in the reference model in the field weakening region [45, 46], which leads to the back-EMF MRAS instability.

In this chapter, in order to deal with the aforementioned problems, a new back-EMF MRAS scheme is proposed for the purpose of fault tolerant *limp-home* mode operation in EV applications. The reference model of this scheme takes advantage of a novel compensating mechanism, to compensate for errors due to parameter variations and digitisation in high speed regions. A new approach is used in the adjustable model of this scheme which is also free from integration problems. This results in an effective sensorless control when starting from standstill and during high speed operation. A realistic speed/torque profile is used for testing purposes. Experimental results demonstrate the robustness of this scheme against motor parameter variations in addition to successful starting from standstill. The vehicle test–drive, utilising the proposed scheme, confirms control stability and reliability during vehicle hill-starting and field weakening operation.

## 5.2 Sensorless TCD based on IRFOC using back-EMF MRAS

The overall block diagram of the sensorless TCD based on IRFOC used in this chapter for fault tolerant EV application is shown in Fig. 5.1. In EV applications the torque demand is applied by the driver using the accelerator pedal. In this approach the reference stator current on the direct-axis ($i_d^*$) is provided from a LUT and the reference stator current on the quadrature-axis ($i_q^*$) is calculated from electromagnetic torque equation of the IM (3.34).

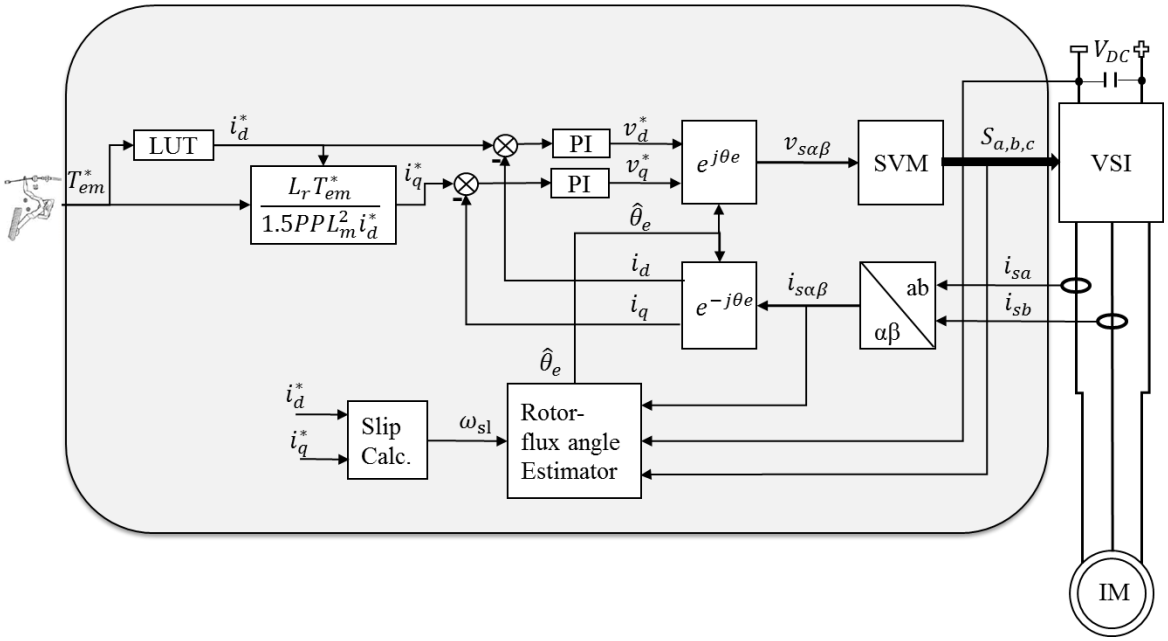


**Fig. 5.1. Block diagram of sensorless TCD based on IRFOC.**

## 5.3 Proposed back-EMF MRAS scheme

The block diagram of the proposed back-EMF MRAS is shown in Fig. 5.2. The signal flow diagrams of the reference and adjustable models of the proposed scheme are shown in Fig. 5.3-(a) and -(b), respectively. The reference model consists of two PI controllers which utilise errors between back-EMF components of the adjustable and reference models, to compensate for the errors due to the motor parameters variation, digitisation. Note that the compensating PI controllers have a lower bandwidth to the one used for the adaptation mechanism. The PI controller of the adaptation mechanism is usually designed to have a bandwidth twice the maximum motor's operating electrical frequency. This allows the MRAS scheme to continue its operation to the field weakening region. The adjustable model is based on the back-EMF in the synchronous reference frame, hence the mutual cross coupling and rotor-flux integration in (3.37) is no longer required. This approach promotes increase in the stability of the MRAS schemes, due to being immune from problems related to the offset accumulations caused by integration. The back-EMF components of the adjustable model are initially calculated in the synchronous reference frame and then transformed to the stationary reference frame.

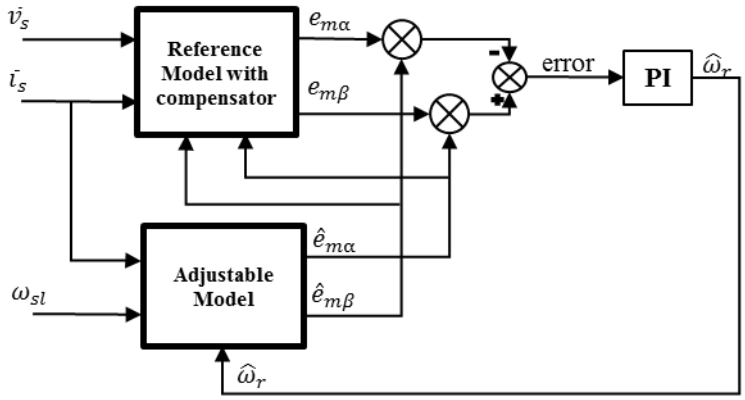


**Fig. 5.2. Block diagram of the proposed back-EMF MRAS scheme.**

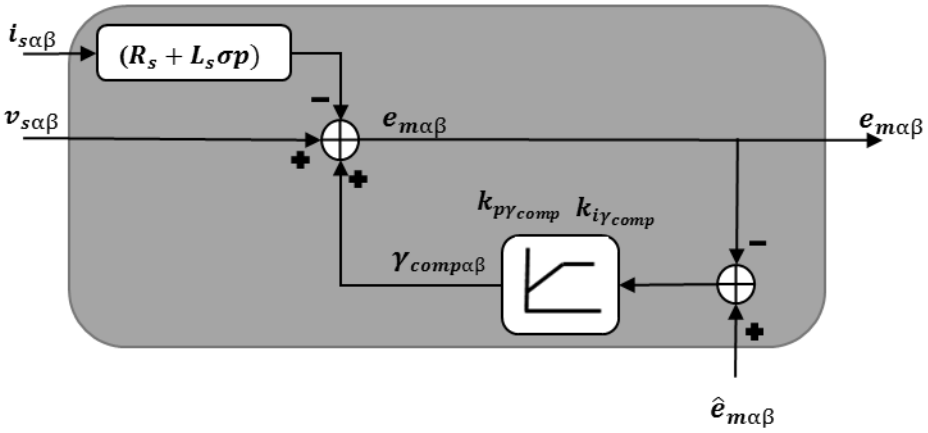


**(a)**

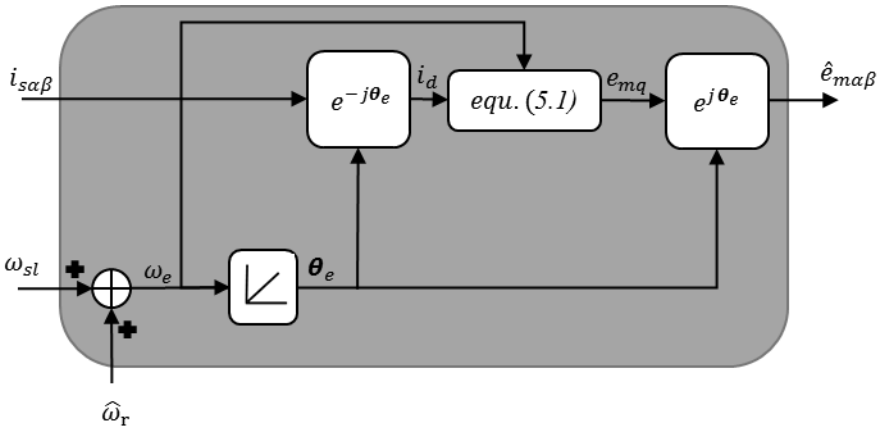


**(b)**

**Fig. 5.3. Signal flow diagrams of the proposed scheme; (a) reference model and (b) adjustable model.**

The back-EMF of IM can be expressed in the synchronous reference frame as follows:

$$e_{mq}^{e} = \omega_e \frac{L_m}{L_r} \psi_{rd}. \tag{5.1}$$

$e_{mq}^{e}$ is back-EMF in the synchronous rotor flux reference frame.

Note that it has been assumed that the transformation of the stator current components from the stationary to the synchronous reference frame are made in the complete rotor flux reference frame. This allows the back-EMF term, in the synchronous rotor flux reference frame, to only appear on the q-axis. The back-EMF is proportional to the rotor flux and the synchronous speed. The estimated back-EMF vector of the adjustable model is calculated by transforming (5.1) from the synchronous to the stationary reference frame:

$$\begin{cases} \hat{e}_{m\alpha} = -\, e_{mq}^{e} * \sin(\hat{\theta}_e) \\ \hat{e}_{m\beta} = e_{mq}^{e} * \cos(\hat{\theta}_e) \end{cases} \tag{5.2}$$

where, $\hat{\theta}_e$ is estimated angular position in the synchronous reference frame.

The back-EMF vector of the reference model in the stationary reference frame is calculated using the following:

$$\begin{cases} e_{m\alpha} = v_{s\alpha} - \left(R_s i_{s\alpha} + L_s \sigma \frac{d}{dt} i_{s\alpha}\right) + \gamma_{comp\alpha} \\ e_{m\beta} = v_{s\beta} - (R_s i_{s\beta} + L_s \sigma \frac{d}{dt} i_{s\beta}) + \gamma_{comp\beta} \end{cases}. \tag{5.3}$$

Where, ( $\gamma_{comp\alpha}$ $and$ $\gamma_{comp\beta}$) are the back-EMF compensating components. These are calculated utilising PI controllers to drive the error between the back-EMF components of the adjustable and reference models to zero.

$$\begin{cases} \gamma_{comp_\alpha} = \left(k_{p\gamma_{comp}} + \frac{k_{i\gamma_{comp}}}{s}\right)\left(\epsilon_{\gamma_{comp\alpha}}\right) \\ \gamma_{comp_\beta} = \left(k_{p\gamma_{comp}} + \frac{k_{i\gamma_{comp}}}{s}\right)(\epsilon_{\gamma_{comp\beta}}) \end{cases}. \tag{5.4}$$

Where; $\epsilon_{\gamma_{comp\alpha}} = \hat{e}_{m\alpha} - e_{m\alpha}$ and $\epsilon_{\gamma_{comp\beta}} = \hat{e}_{m\beta} - e_{m\beta}$ are the back-EMF error components used in the compensating mechanism.

Fig. 5.4 shows a block diagram of the compensating mechanism. The term $e_{m\alpha\beta_{[nom]}}$ represents the nominal back-EMF components, calculated when nominal parameters of the IM are used. The term $e_{m\alpha\beta}$ represents the output back-EMF components of the reference model.

The term $\Delta D$ represents disturbances in the stationary reference frame due to parameter variations ($\Delta R_s \; and \; \Delta L_s \sigma$) and digitisation which can affect the reference model. Without the compensator, the output back-EMF components include the nominal back-EMF components plus some disturbances. These disturbances can cause a steady state error, oscillation and eventually lead to instability, especially in the low speed region due to stator resistance variation. However, by closing the loop using the estimated back-EMF components from the adjustable model, which are free from aforementioned disturbances, the effects of $\Delta D$ can be eliminated.

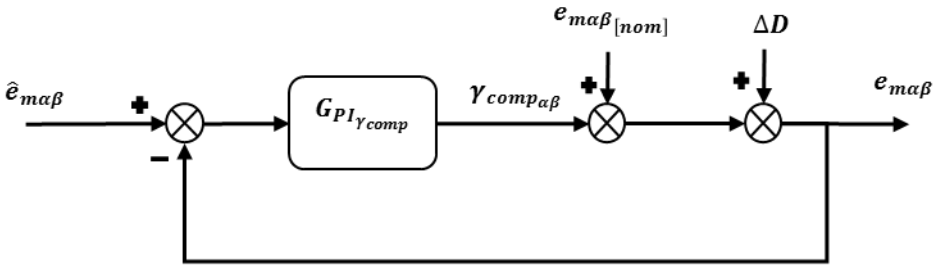


**Fig. 5.4. Block diagram of the compensating mechanism.**

The transfer function of feedback block diagram of the compensating mechanism with respect to the output back-EMF components and the control loop can be expressed by superposition of the response to the three inputs individually, as follows:

$$e_{m\alpha\beta\,cl} = \frac{G_{PI_{\gamma comp}}}{1 + G_{PI_{\gamma comp}}}\,\hat{e}_{m\alpha\beta} + \frac{1}{1 + G_{PI_{\gamma comp}}}\,e_{m\alpha\beta\,[nom]} + \frac{1}{1 + G_{PI_{\gamma comp}}}\,\Delta D\,. \tag{5.5}$$

The compensating mechanism is stable if all the poles of (5.5) are on the left half-plane (LHP). This can be investigated in the s-plane by setting the denominator to zero, which yields:

$$\mathrm{s} = -\frac{k_{i\gamma comp}}{1 + k_{p\gamma comp}}. \tag{5.6}$$

It can be seen that (5.6) is negative, hence, the compensator is stable. For the adaptation mechanism a PI controller, similar to the one used for the conventional scheme in (3.44), is employed to minimise the speed error. To guarantee that the estimated rotor speed converges

to the actual rotor speed, the overall proposed MRAS requires to be asymptotically stable. The overall stability of the proposed MRAS is investigated by employing a Lyapunov function V, which is expressed as below [23]:

$$V = \bar{\epsilon}_{e_m}^{T} \bar{\epsilon}_{e_m} > 0. \tag{5.7}$$

Where, $\bar{\epsilon}_{e_m} = \begin{bmatrix} e_{m\alpha} - \hat{e}_{m\alpha} \\ e_{m\beta} - \hat{e}_{m\beta} \\ x_{m\alpha} - \hat{x}_{m\alpha} \\ x_{m\beta} - \hat{x}_{m\beta} \end{bmatrix}$ is error vector.

In order to derive the state error equations the following assumptions are made:

$$\begin{cases} x_{m\alpha} = \dot{\omega}_e \dfrac{L_m}{L_r} \psi_{rd}\, sin(\theta_e) \\ x_{m\beta} = -\dot{\omega}_e \dfrac{L_m}{L_r} \psi_{rd}\, cos(\theta_e) \\ \dot{\omega}_e = 0 \end{cases}. \tag{5.8}$$

The state error equations can be expressed as below:

$$\dot{\bar{\epsilon}}_{e_m} = [A]\left[\bar{\epsilon}_{e_m}\right] - [W]. \tag{5.9}$$

Where;

$$A = \begin{bmatrix} 0 & \omega_e & -1 & 0 \\ -\omega_e & 0 & 0 & -1 \\ 0 & 0 & 0 & -1 \\ 0 & 0 & 1 & 0 \end{bmatrix}, \qquad W = \hat{e}_{m\alpha\beta} \otimes (\omega_e - \hat{\omega}_e). \tag{5.10}$$

Differentiating both side of (5.7), yields:

$$\dot{V} = \left(\dot{\bar{\epsilon}}_{e_m}^{T}\, \bar{\epsilon}_{e_m}\right) + \left(\bar{\epsilon}_{e_m}^{T}\, \dot{\bar{\epsilon}}_{e_m}\right) = \bar{\epsilon}_{e_m}^{T}(A^T + A)\bar{\epsilon}_{e_m} = -I\bar{\epsilon}_{e_m}^{T}\bar{\epsilon}_{e_m}. \tag{5.11}$$

Where, $I = \begin{bmatrix} 0 & 0 & 1 & 0 \\ 0 & 0 & 0 & 1 \\ 1 & 0 & 0 & 0 \\ 0 & 1 & 0 & 0 \end{bmatrix}$.

The function given in (5.11) is always negative. A system is said to be asymptotically stable if Lyapunov function satisfies following conditions [23, 95];

$$\begin{cases} 1)\ V\ = 0\ for\ \widehat{\omega}_e\ = 0 \\ 2)\ V > 0\ for\ \left|\left|\widehat{\omega}_e\right|\right|\ \neq 0 \\ 3)\ \dot{V}\ \leq 0 \quad \forall \widehat{\omega}_e \end{cases} \tag{5.12}$$

It is clear that (5.7) satisfies conditions 1 and 2 of (5.12), this is regardless of the estimated speed direction. Moreover, (5.11) also satisfies condition 3 of (5.12). Hence, it can be state that the proposed scheme is asymptotically stable.

## 5.4 Results and discussion

In this section, simulation and experimental results and discussion are presented to evaluate the effectiveness and feasibility of the proposed scheme for different operating conditions. Using the test bench, the performance of the proposed scheme was compared against that of the conventional back-EMF MRAS scheme. All of the experiments were conducted in the sensorless mode. For these tests the measured (encoder) and estimated (sensorless) speeds were recorded.

In order to tune the estimator PI controller gains of the proposed scheme, the identical compensator PI controllers gains, were initially set to zero. To obtain the optimal dynamic performance, the adaptation PI controller gains were first tuned whilst the encoder signal was used for the transformation between reference frames. The proportional gain of the adaptation PI controller was gradually increased, while the integral gain was set to zero, until the estimator speed could approximately track the actual speed. Then the integral gain was increased to achieve faster dynamic response. After aforementioned procedure for the proposed scheme, both gains of the compensator PI controllers were set to one. This results in a small steady state error between the actual and estimated speed. By gradually decreasing both gains the error is reduced to zero. We have found that the dynamic performance of the compensator PI controllers are more dependent on the proportional gain than the integral gain. Therefore, the integral gain can be set to any value smaller than one, as long as it is greater than zero.

Utilising the above procedure, for experiments on the dynamometer test bench, the adaptation PI controller gains of the conventional and proposed schemes were set to ($K_p = 1\ and\ K_i = 0.1$) and ($K_p = 0.8\ and\ K_i = 0.08$), respectively. The gains of the compensator PI controllers in the reference model of the proposed scheme were set to ( $k_{p\gamma_{comp}} = 0.1\ and\ k_{i\gamma_{comp}} = 0.001$). For experiments on the golf buggy, the adaptation PI controller gains of the proposed schemes were set to ($K_p = 0.9\ and\ K_i = 0.08$). The gains of the

compensator PI controllers in the reference model of the proposed scheme were set to ($k_{p\gamma_{comp}} = 0.1 \; and \; k_{i\gamma_{comp}} = 0.002$).

### 5.4.1 Simulation results

Initially, the behaviour of the proposed and conventional back-EMF schemes have been studied in the simulation environment using Matlab/Simulink software. Using the mathematical model of an IM in the stationary reference frame, as given in (3.11), a motor with nominal parameters similar to the one provided in Table 4.1 was modelled. To calculate the rotor speed a mechanical model is used:

$$\omega_r = \frac{1}{J}\int (T_{em} - T_{load} - B\omega_r)dt \tag{5.13}$$

To apply load on the IM, a load function has been modelled with respect to the motor speed, which is as follows:

$$T_{load} = \omega_r^3 k_{load} \tag{5.14}$$

where, $k_{load}$ is a positive constant, which is tuned to provide a load torque value as close as possible to the electromagnetic torque.

To drive the IM, the TCD based on IRFOC, shown in Fig. 5.1, was also developed in Matlab/Simulink environment.

#### *5.4.1.1 Different torque levels using motor nominal parameters*

The following test was carried out to demonstrate the performance of the proposed and conventional back-EMF schemes for different applied torque levels using motor nominal parameters. During these tests the applied torque level was varied while the load function was used to apply similar value of load on the IM. The results for the conventional and the proposed schemes are shown in Fig. 5.5-(a) and -(b), respectively. From the results of both schemes, it can be seen that the estimated speed closely tracks the measured speed and that the value of the measured torque matches the applied torque command level.

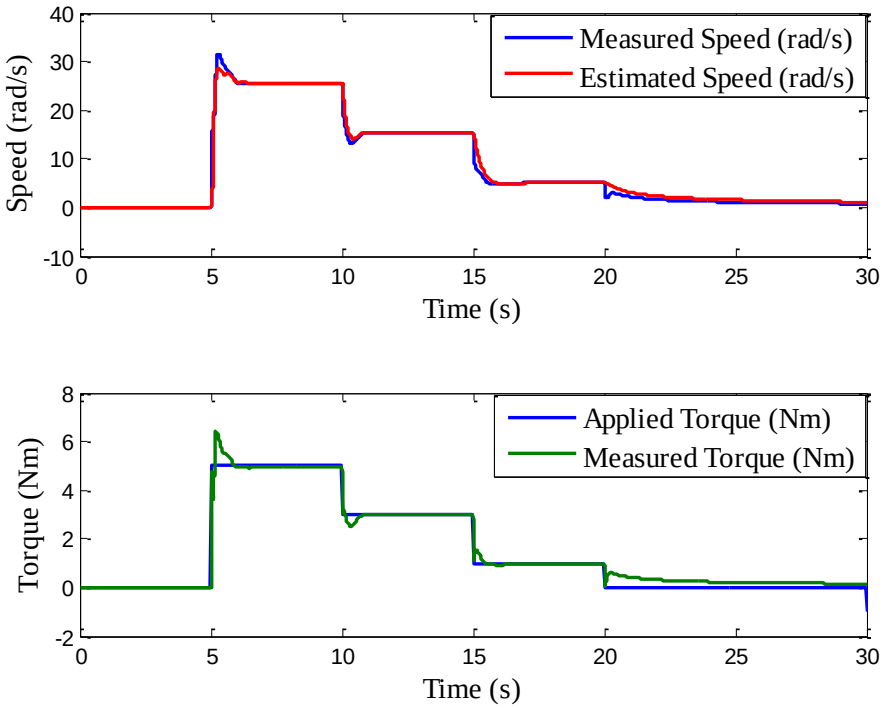


(a)

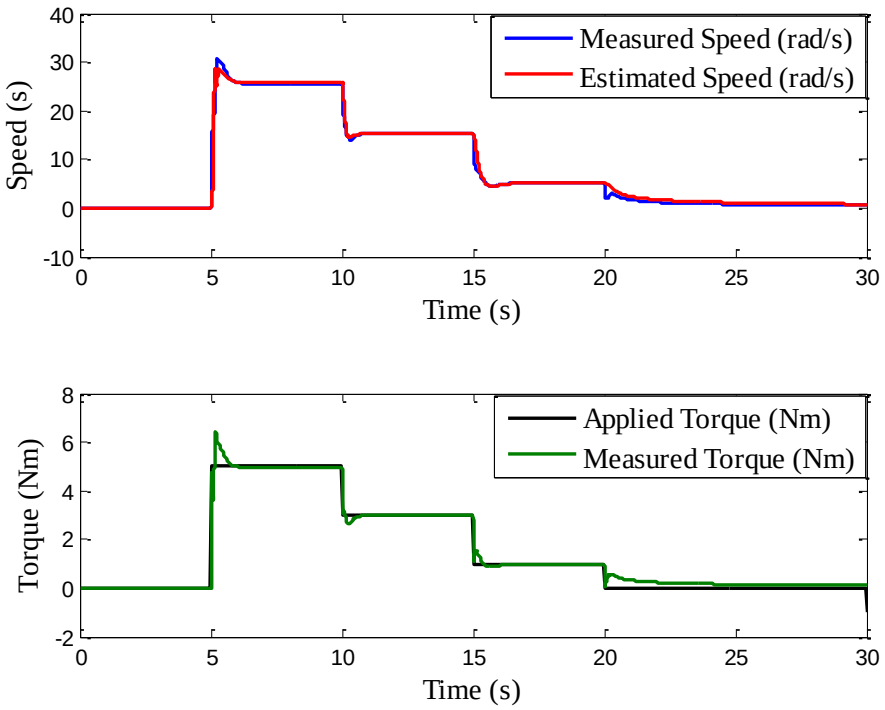


(b)

**Fig. 5.5. Simulation results for sensorless control at different applied torque levels with the motor nominal parameters. (a) The conventional scheme, and (b) the proposed scheme.**

#### *5.4.1.2 Different torque levels with 50% stator resistance variation*

This test was carried out to demonstrate the performance of the proposed and the conventional back-EMF schemes against 50% stator resistance variation. For this test the nominal value of the stator resistance in the IM model has been increased by 50%. From the results of the conventional scheme, which is shown in Fig. 5.6-(a), it can be seen that the stator resistance variation causes a steady-state error between the estimated and measured speeds. Moreover, in the low speed region the conventional scheme becomes unstable, hence the measured torque at 1 Nm no longer follows the applied torque command. However, from the results of the proposed scheme, which is shown in Fig. 5.6-(b), it can be seen that the estimated speed closely continues to follow the measured speed. The measured torque also tracks the applied torque command.

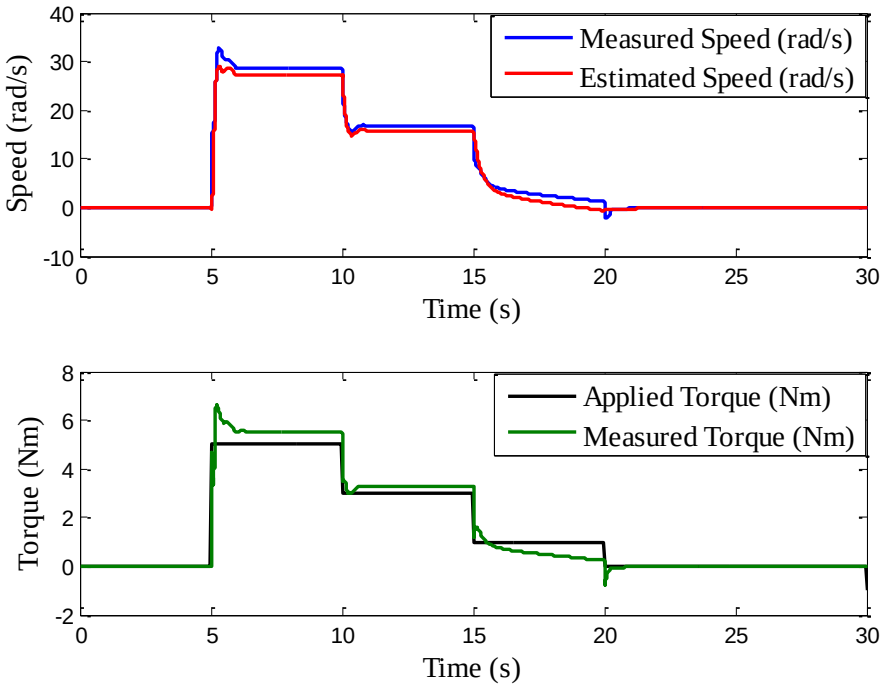


(a)

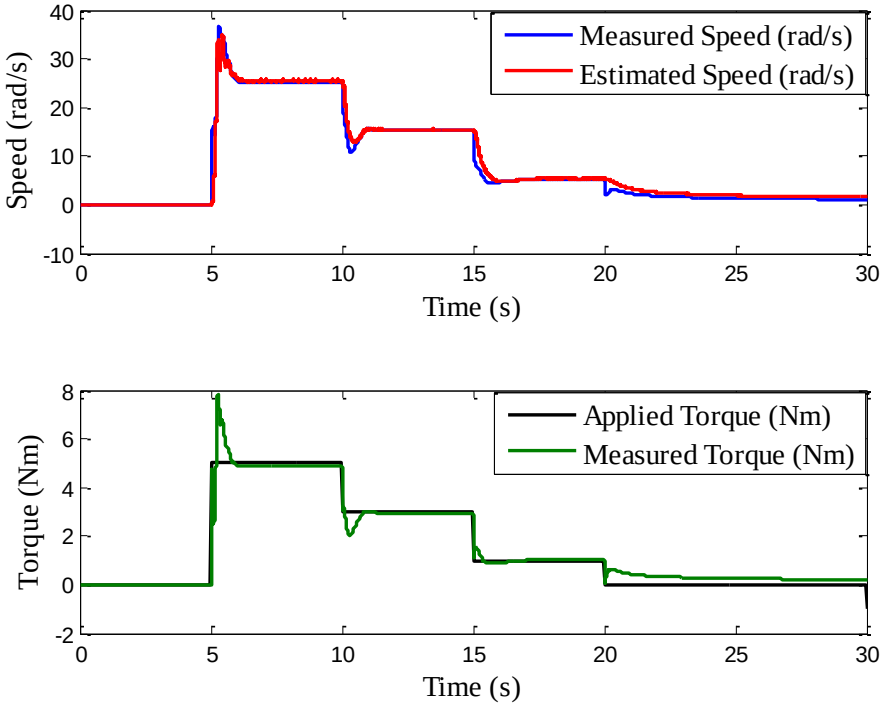


(b)

**Fig. 5.6. Simulation results for sensorless control at different applied torque levels with 50% stator resistance variation. (a) The conventional scheme, and (b) the proposed scheme.**

### 5.4.2 Experimental results from dynamometer setup

#### *5.4.2.1 Starting from standstill*

The sensorless IM TCD used for the purpose of fault tolerant *limp-home* mode of EV applications, must be capable of performing adequately at zero and low speeds. It is also very important to have consistency in performing vehicle-starting from standstill for consecutive attempts. Therefore this test was carried out for three consecutive attempts in forward direction to demonstrate the consistency of the conventional and the proposed back-EMF MRAS schemes for starting from standstill. During this test the speed is varied using the throttle box with the applied torque command kept at 15 Nm. Fig. 5.7-(a) shows the result of this test for the conventional scheme. Since, in the first attempt the conventional scheme had failed to start from standstill for an applied torque command of 15 Nm, the torque command was increased to 20 Nm and 25 Nm for the second and third attempts, respectively. From result of the proposed scheme, which is shown in Fig. 5.7-(b), it is clear that this scheme is consistent in starting from standstill and shows no steady-state error at zero speed.

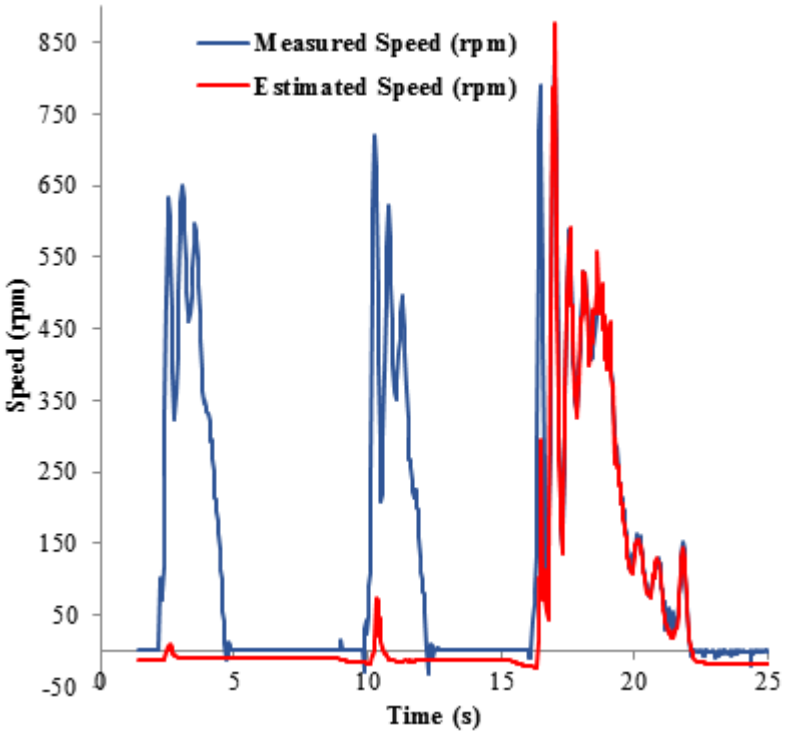


**(a)**

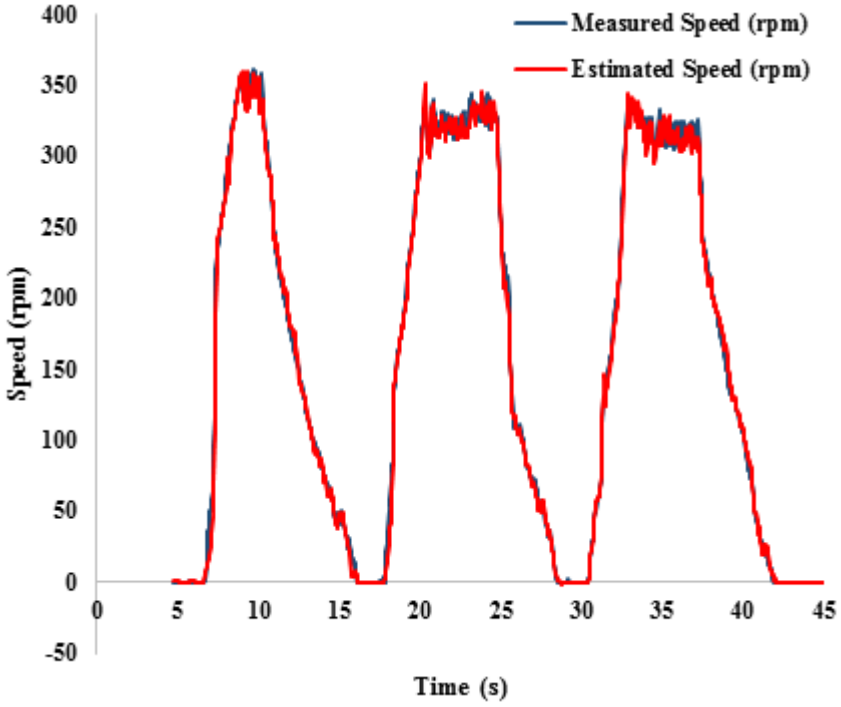


(b)

**Fig. 5.7. Experimental results for sensorless performance starting from standstill with nominal parameters at 15 Nm. (a) Conventional Back-EMF MRAS (b) the proposed scheme.**

#### *5.4.2.2 Sensitivity to stator resistance variation*

This test was carried out to demonstrate robustness of the proposed scheme against sensitivity to the stator resistance variations. During this test the stator resistance was increased by 50% and 100% from its nominal value and the applied torque command was kept constant at 15 Nm. Results for the conventional scheme are shown in Fig. 5.8-(a) and Fig. 5.9-(a) for cases of 50% and 100% increase in the stator resistance value, respectively. It is clear that, in the case of 50% increase, this scheme suffers from sensitivity to stator resistance variations at low speeds and it becomes more unstable for the case of 100% increase. Results of the proposed scheme are shown in Fig. 5.8-(b) and Fig. 5.9-(b) for 50% and 100% increase in the stator resistance value, respectively. It is obvious that the estimated speed continuous tracking the measured speed regardless of 50% or 100% increase in the stator resistance value. Hence the proposed scheme is robust against sensitivity to the stator resistance variations.

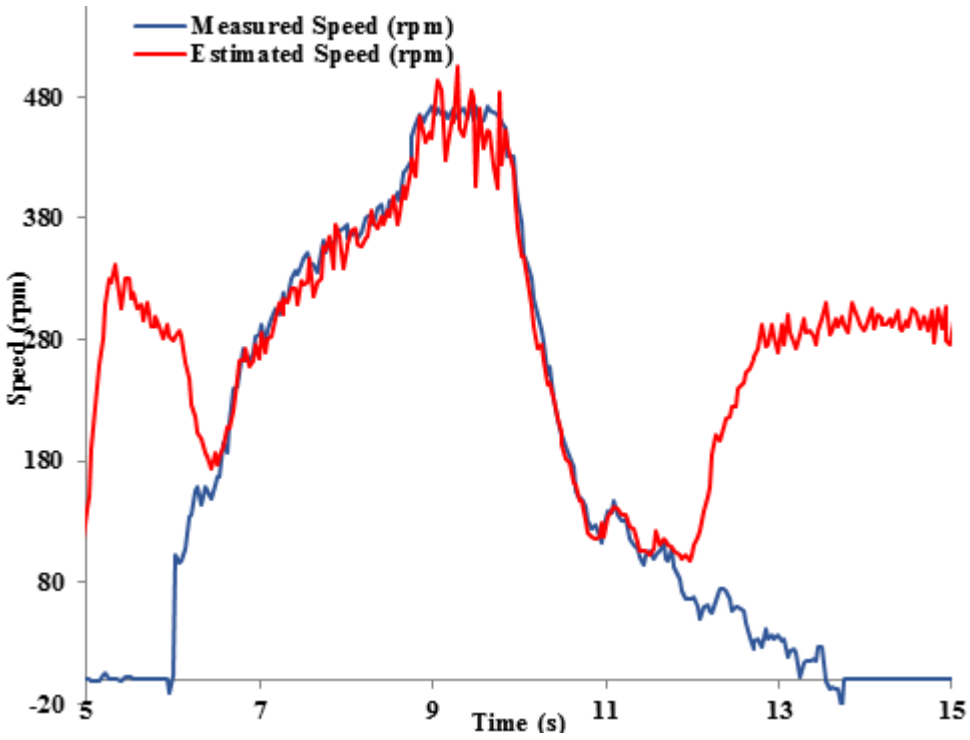


**(a)**

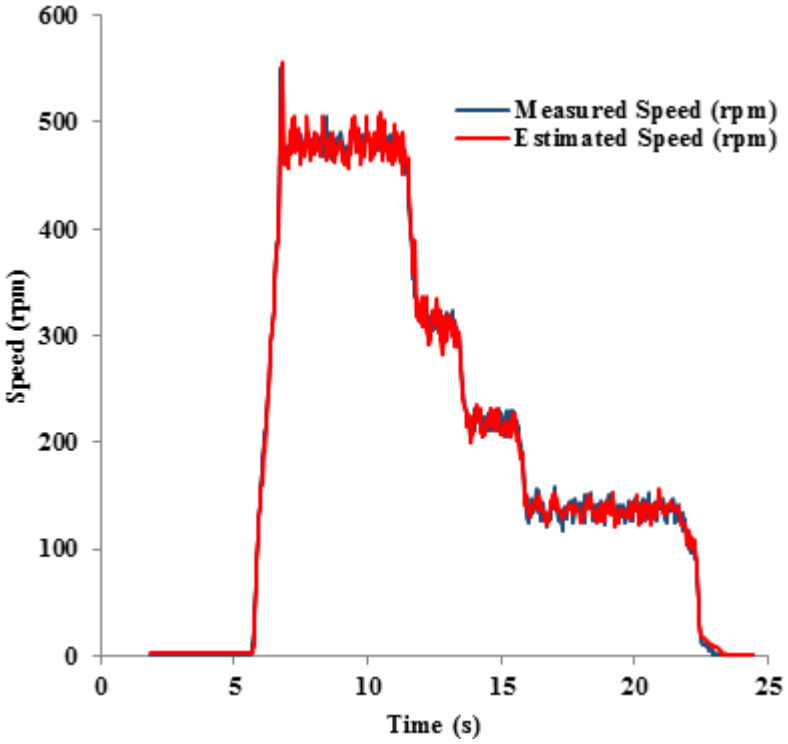


(b)

**Fig. 5.8. Experimental results for sensorless performance with 50% increase in the stator resistance at 15 Nm. (a) Conventional Back-EMF MRAS (b) the proposed scheme.**

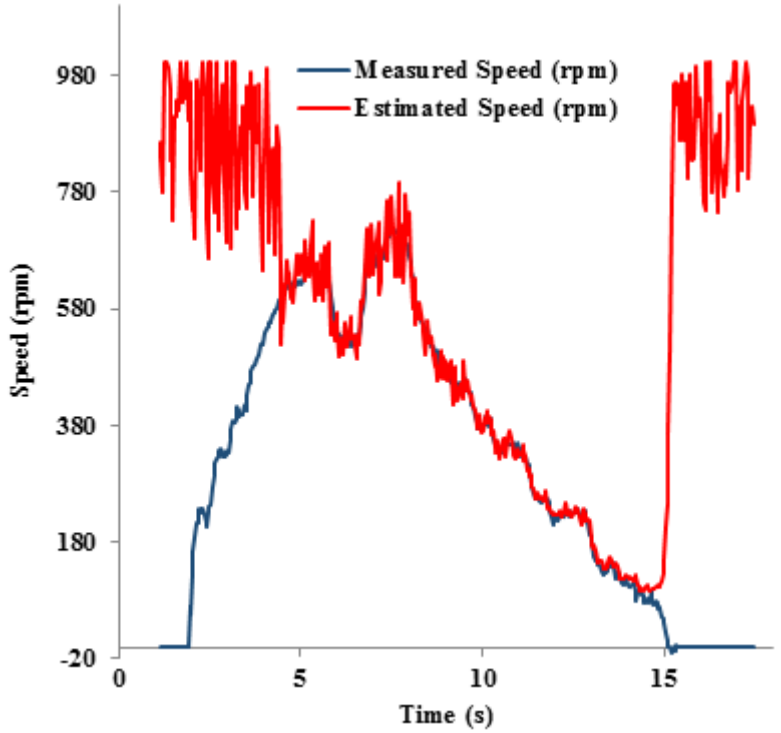


**(a)**

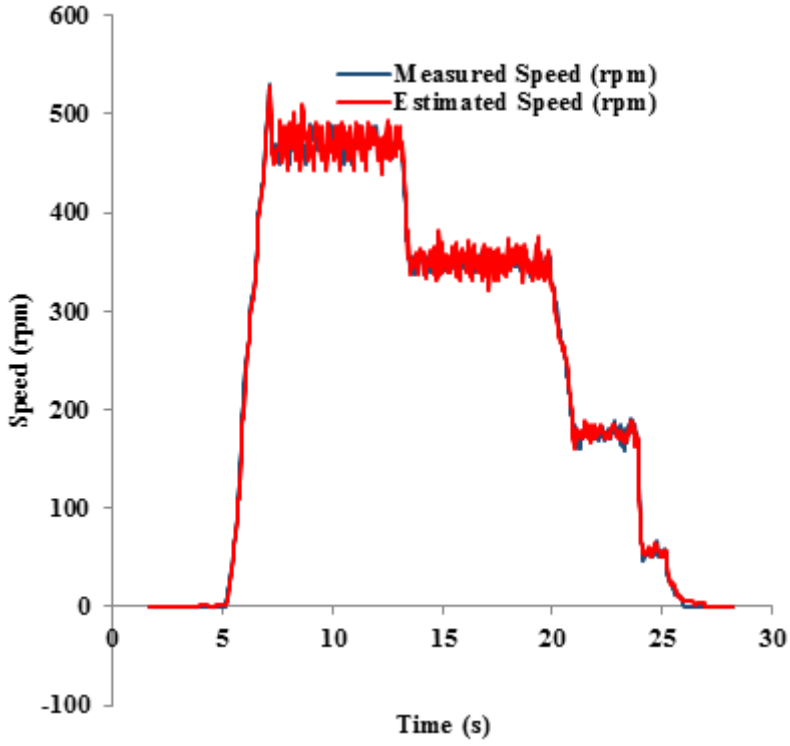


(b)

**Fig. 5.9. Experimental results for sensorless performance with 100% increase in the stator resistance at 15 Nm. (a) Conventional Back-EMF MRAS (b) the proposed scheme.**

#### *5.4.2.3 Constant speed operation at different torque levels*

This test was carried out to demonstrate the behaviour of the proposed scheme at constant speed with load torque variations. For this test the shaft speed was kept constant at 300 rpm with the applied torque command varied in 5 Nm intervals from 15 Nm to 50 Nm. Results of this test are shown in Fig. 5.10-(a) and -(b) for the conventional and proposed schemes, respectively. As can be seen, the conventional scheme has significant oscillations and at 50 Nm, it completely loses stability. Hence the estimated speed no longer tracks the measured speed. On the contrary, the proposed scheme shows much less oscillations and the estimated speed continuously tracks the measured speed closely regardless of variations in the torque command level.

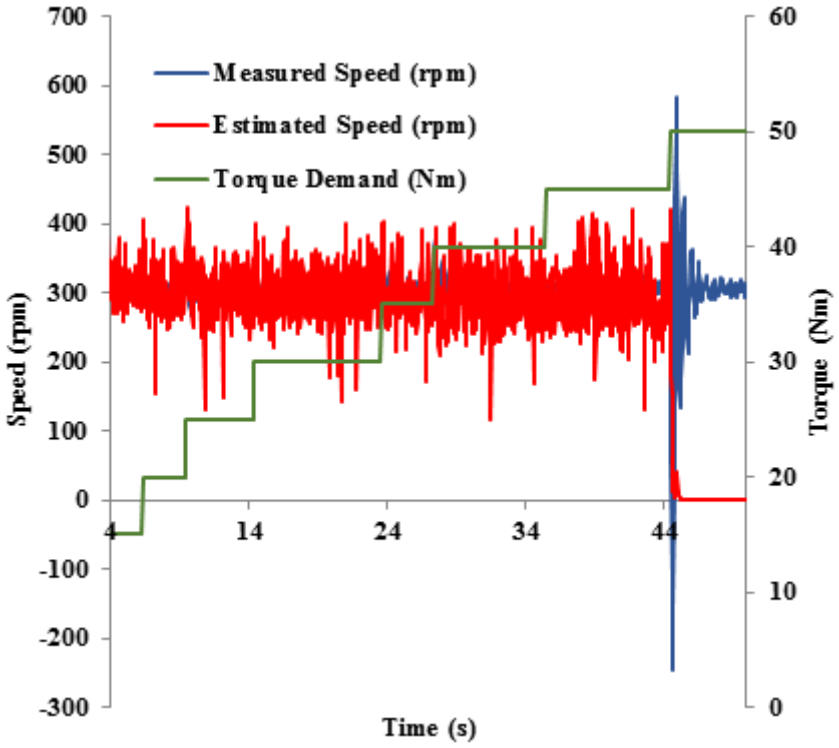


**(a)**

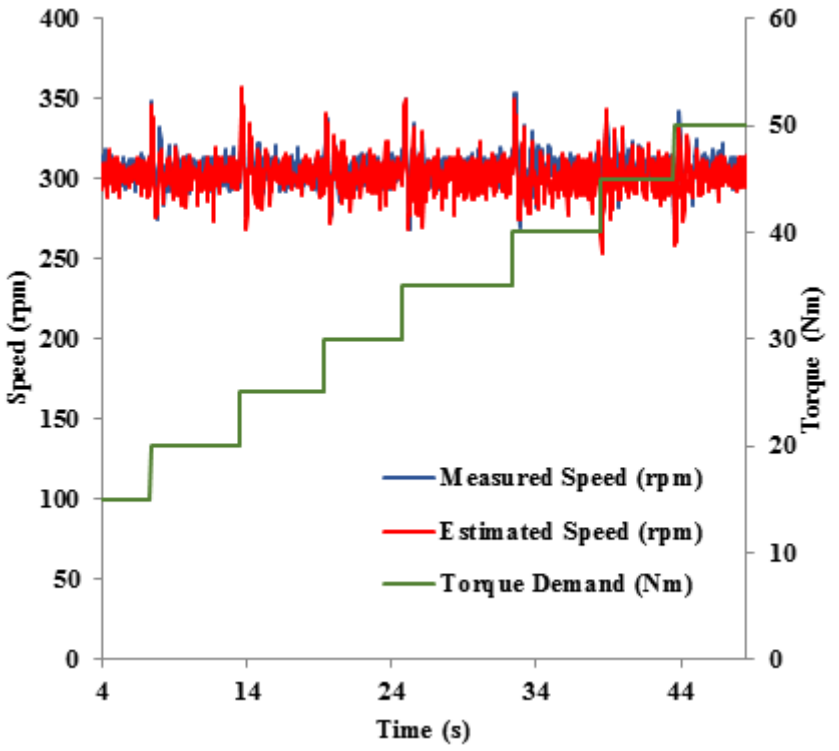


(b)

**Fig. 5.10. Experimental results for sensorless performance at constant speed in region of 300 rpm with the torque command increased in 5 Nm intervals from 15 Nm to 50 Nm. (a) Conventional Back-EMF MRAS (b) the proposed scheme.**

### 5.4.3 Experimental results from golf buggy

The following tests were carried out only for the proposed scheme. For these tests the estimated speed, utilising the proposed scheme, was employed in the controller instead of the signal from the AB encoder, which was mounted on the vehicle's IM. The speed from the encoder was only used for validation which is labelled as measured speed in the recorded results. During these tests, forward, park and reverse operation modes were manually selected using the vehicle's gear stick and the torque command was applied using the accelerator pedal.

#### *5.4.3.1 Vehicle test-drive for consecutive vehicle-starting from standstill*

This test was carried out to confirm the capability of the proposed scheme during consecutive attempts for vehicle-starting from standstill in forward and reverse mode directions using the golf buggy. During this test, the vehicle was first driven forward and suddenly stopped by applying brake pedal, which was repeated for 5 attempts. After changing to the reverse mode the same procedure was repeated for the reverse direction for 3 attempts. The result of this test is shown in Fig. 5.11. It is clear that the estimated speed tracks the measured speed very closely in both directions and despite sudden changes in the vehicle speed the estimator remains stable and consistent in vehicle-starting from standstill.

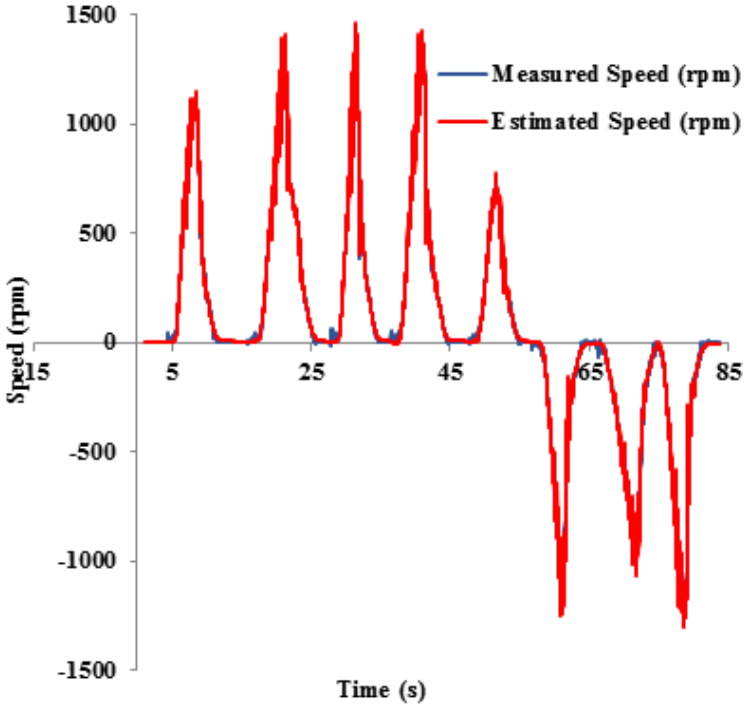


**Fig. 5.11. Experimental result from Golf buggy. Sensorless vehicle-starting from standstill for consecutive attempts in forward and reverse modes of operation.**

### *5.4.3.2 Forward and reverse test-drive in wide speed range*

It is required that sensorless schemes used for EV applications be capable of performing in a wide speed range, especially in the field weakening region. Therefore this test was carried out to demonstrate the capability of the proposed scheme for wide range of speeds. During this test the vehicle was accelerated forward to around +2860 rpm and then slowed down to zero and the same procedure was repeated in the reverse direction for the speed around -2860 rpm. Fig. 5.12 shows the result of this test, which confirms the capability and reliability of the proposed scheme across the whole speed range. Moreover, utilising the proposed scheme provides a smooth test-drive in wide speed range.

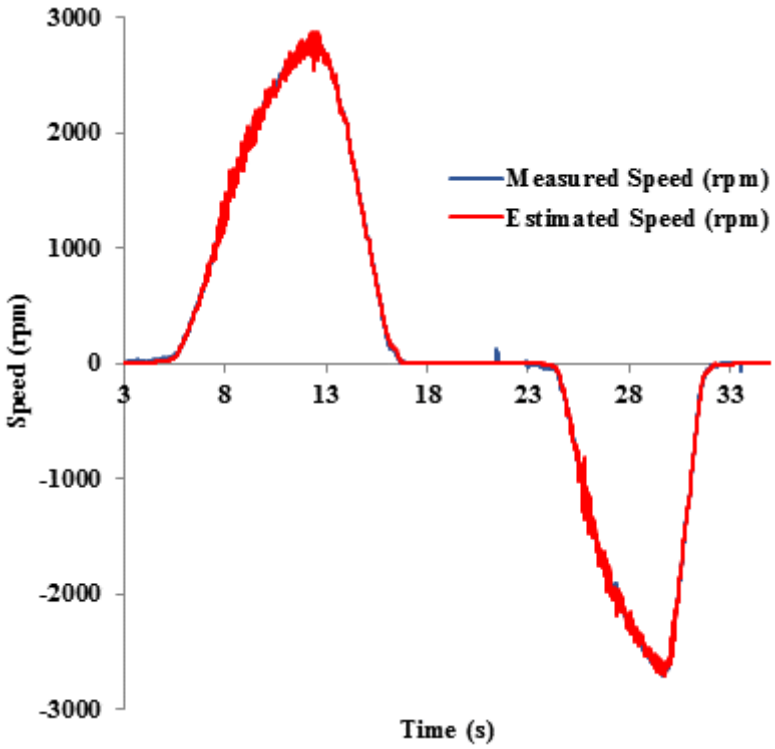


**Fig. 5.12. Experimental result from Golf buggy. Sensorless vehicle test-drive in wide speed range for forward and reverse modes drive operation.**

### *5.4.3.3 Vehicle hill-starting performance*

This test was carried out to demonstrate the behaviour of the proposed scheme during vehicle hill-starting. In order to create a realistic worst case scenario, this test was carried out after 30 mins of the vehicle test-drive to increase the motor's temperature, hence increase in the stator resistance above its nominal value. A 15 degree ramp, which is especially designed for the vehicle hill-starting test, was used for purpose of this test. In order to prevent the vehicle from rolling backwards, a torque command of around 5 Nm was initially applied, using the accelerator pedal. The torque command was gradually increased to cause the vehicle to move forward and then the accelerator was gradually eased back to reduce the torque command to around 5 Nm again. The result of this test is shown in Fig. 5.13, which illustrates stability and reliability of this scheme during the vehicle hill-starting. It is clear that the vehicle did not roll backward during standstill period while it was on the ramp.

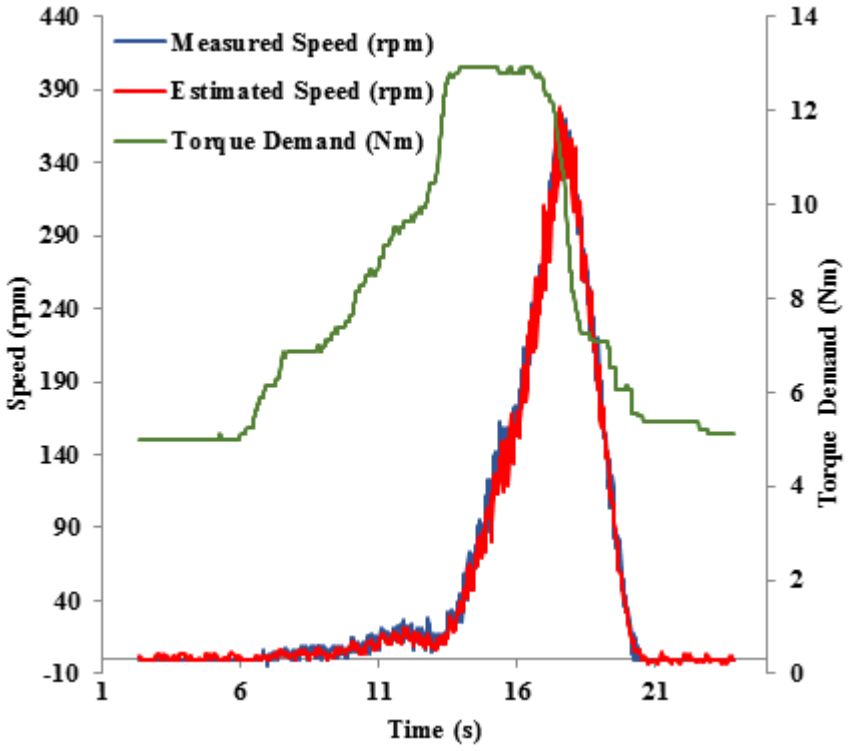


**Fig. 5.13. Experimental result from Golf buggy. Sensorless vehicle test-drive in hill-starting for forward mode drive operation.**

## 5.5 Conclusion

A novel back-EMF MRAS speed estimator is described in this chapter for the purpose of sensorless TCD employed for the fault tolerant *limp-home* mode EV applications. The proposed scheme was successfully implemented and tested on two different IMs using the laboratory test bench and golf buggy, respectively. This scheme is not computationally demanding and is robust against stator resistance variations of 50% and 100% increase. The proposed scheme is not only consistent and stable for the vehicle-starting from standstill and low speeds, it also performs reliably above base speed in the field weakening region. During the tests, the proposed scheme had shown satisfactory operation throughout forward and backword modes of operation in addition to the constant speed variable load operation. More importantly the scheme had demonstrated satisfactory performance for vehicle hill-starting. Therefore the proposed back-EMF MRAS scheme is suitable for the *limp-home* mode operation of EV applications by providing consistent, safe and reliable operation over the whole speed range.

However, to implement this scheme all the IM nominal parameters are required. Therefore developing a sensorless scheme which is less dependent on the prerequisite knowledge of the IM nominal parameters will be the purpose of the next chapter.

# CHAPTER 6. SENSORLESS CONTROL OF IM BASED ON STATOR VOLTAGE MRAS

A novel sensorless speed estimation is described for an IM based on a new Vs-MRAS scheme. The Vs-MRAS scheme uses the error between the reference and estimated stator voltage vectors and estimates the synchronous speed. Unlike existing MRAS schemes, the proposed sensorless scheme does not require the measured nominal values of stator resistance, stator inductance, and rotor resistance. This scheme is insensitive to variations of the aforementioned parameters. Moreover, using the proposed scheme eliminates the need for slip calculation. The proposed scheme is implemented and experimentally tested in the lab environment, on the 19 kW IM**,** and also applied on the electric golf buggy, powered by the 5 kW IM. The results show that the proposed scheme is immune to parameter variations and is consistent in vehicle-starting from standstill and hill-starting tests. This scheme is also free from drift problems associated with a pure integration and is stable in the field weakening region. The test-drive results from the golf

buggy confirm suitability of the proposed Vs-MRAS scheme over a wide range of speeds for the purpose of TCD in EV applications.

## 6.1 Introduction

It is essential for the sensorless scheme which is employed, for the purpose of fault tolerant EV application, to be capable of functioning during vehicle-starting from standstill and low speeds. More importantly, the sensorless algorithm should be less complicated and require smaller execution time to make an efficient use of the limited available space in the DSP [5]. Among these approaches, speed estimation based on MRAS schemes are relatively simpler to implement and often require lower computational effort [22, 25].

In this chapter, a novel Vs-MRAS scheme is proposed for the purpose of fault tolerant *limp-home* operation for EV applications. The proposed scheme takes advantage of stator voltage reference components in the stationary reference frame by setting them as its reference model. These are compared with the estimated stator voltage components using the measured stator current components. This scheme is computationally simpler to implement and is independent from the initially measured nominal motor parameters such as; stator resistance, stator inductance, and rotor resistance. The proposed scheme is immune to parameter variations and errors due to digitisation in the field weakening region. Experimental tests are carried out to investigate the performance of the proposed scheme. Experimental results show robustness of this scheme against stator resistance variation in addition to successful starting from standstill. The vehicle test-drive, utilising the proposed scheme, confirms the consistency and reliability of this scheme in a wide speed range.

The structure of this chapter is as follows; Section 6.2 describes the sensorless TCD based on IRFOC technique using the proposed scheme. Section 6.3 gives a detailed description of the new Vs-MRAS scheme. Section 6.4 shows the simulation and experimental results of the proposed sensorless scheme. Finally the conclusion is provided in Section 6.5.

## 6.2 Sensorless TCD based on IRFOC technique using proposed Vs-MRAS

The overall block diagram of the sensorless TCD based on IRFOC employing the proposed scheme is shown in Fig. 6.1. The accelerator pedal is used for applying the torque demand in EV. A LUT is used to produce the value of the reference d-axis stator current and the reference q-axis stator current is calculated by rearranging the electromagnetic torque equation of the IM.

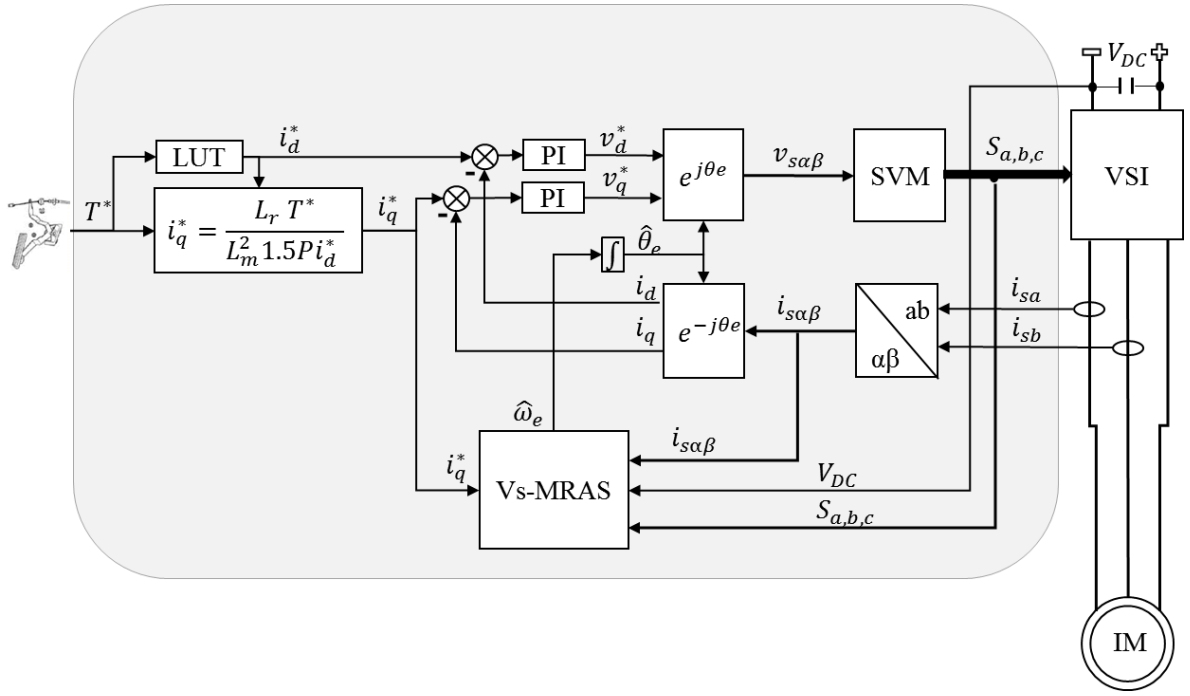


**Fig. 6.1. The overall block diagram of the sensorless TCD of IM based on IRFOC for the purpose of EV application.**

## 6.3 Proposed stator voltage based MRAS scheme

The block diagram of the proposed Vs-MRAS scheme is shown in Fig. 6.2. The signal flow diagrams of the reference model, which is shown in the Fig. 6.3, takes in the reconstructed and estimated (from the adjustable model output) stator voltage components in the stationary reference frame and in return provides the reference stator voltage components. The reference model takes advantage of two identical compensating mechanisms, similar to the one presented in [5]. Utilising these compensators make the proposed scheme immune to errors which are due to parameter variations and digitisation in the field weakening region. The stator voltage space vector is calculated in the stationary reference frame using the measured DC-link voltage and the switching signals [96]:

$$\bar{v}_{s\alpha\beta} = \frac{2 * V_{DC}}{3}\left(S_a + S_b e^{j\frac{2\pi}{3}} + S_c e^{-j\frac{2\pi}{3}}\right). \tag{6.1}$$

Where; $V_{DC}$ is the measured DC-link voltage and $S_{a,b,c}$ are switching signals.

Note that in order to have a sinusoidal signal, when (6.1) is used, the reconstructed stator voltage components are required to be LP filtered. In this thesis two LPFs with 3-kHz cutoff frequency are used. The Simulink implementation of (6.1) is demonstrated in Fig. 10.7 in the

Appendix. A test also carried out to compare the stator voltage components which were obtained from the output of the VSI model and reconstructed using the equation (6.1). From results shown in Fig. 10.8, it is clear that the reconstructed stator voltage components are identical to the ones measured from the output of the VSI model.

Hence, the reference stator voltage components in the stationary reference frame can be expressed as:

$$\bar{v}^*{}_{s\alpha\beta} = \bar{v}_{s\alpha\beta} - \bar{\gamma}_{\alpha\beta}. \tag{6.2}$$

Where, $\bar{v}^*{}_{s\alpha\beta} = (v^*{}_{s\alpha} + jv^*{}_{s\beta})$ is the reference stator voltage, and $\bar{\gamma}_{\alpha\beta} = (\gamma_\alpha + j\gamma_\beta)$ is the compensating vector, which can be calculated from:

$$\bar{\gamma}_{\alpha\beta} = \left(k_{p\gamma} + \frac{K_{i\gamma}}{s}\right) * \left(\bar{\hat{v}}_{s\alpha\beta} - \bar{v}^*{}_{s\alpha\beta}\right). \tag{6.3}$$

Where, $k_{p\gamma}$ and $K_{i\gamma}$ are proportional and integral gains of the identical compensating controllers, respectively, and $\bar{\hat{v}}_{s\alpha\beta} = (\hat{v}_{s\alpha} + j\hat{v}_{s\beta})$ is the estimated stator voltage vector.

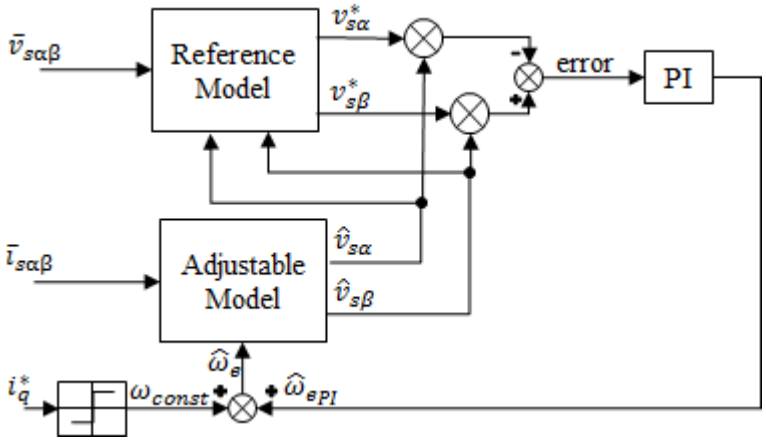


**Fig. 6.2. Block diagram of the proposed stator voltage based MRAS scheme.**

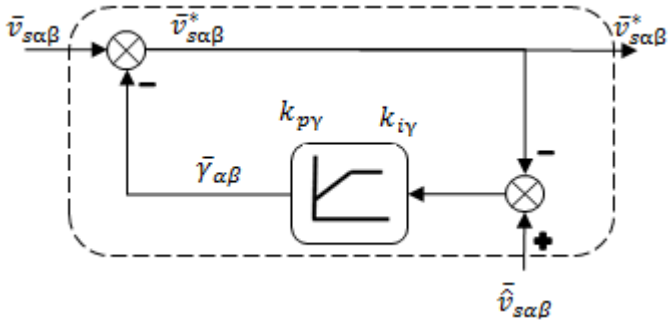


**Fig. 6.3. Signal flow diagram of the reference model of the proposed Vs-MRAS scheme.**

The signal follow diagram of the adjustable model used in this scheme is shown in Fig. 6.4. It uses the measured stator current components and the estimated electrical synchronous speed and in return, by mimicking the voltage model equation, calculates the estimated stator voltage components. This is derived by considering the voltage model equation of IM in the stationary reference frame as:

$$\hat{\bar{v}}_{s\alpha\beta} = \hat{\bar{e}}_{m\alpha\beta} + (R_s + L_s\sigma p)\bar{\imath}_{s\alpha\beta}. \tag{6.4}$$

The estimated back-EMF ($\hat{\bar{e}}_{m\alpha\beta}$) is first calculated in the synchronous reference frame and then transformed into the stationary reference frame:

$$\hat{\bar{e}}_{m\alpha\beta} = e_{mq}e^{j\theta_e} = (\hat{\omega}_e \frac{L_m}{L_r}\psi_{rd})e^{j\theta_e}. \tag{6.5}$$

Where; ($e_{mq} = \hat{\omega}_e \frac{L_m}{L_r}\psi_{rd}$) is back-EMF in the synchronous reference frame, $\hat{\omega}_e$ is synchronous speed and ($\psi_{rd} = i_d L_m$) is d-axis rotor flux.

In order to make the adjustable model independent from the term ($R_s + L_s\sigma p$), (6.4) can be expressed as the following:

$$\hat{\bar{v}}_{s\alpha\beta} = \left(\hat{\bar{e}}_{m\alpha\beta} + (k_1)\bar{\imath}_{s\alpha\beta}\right)k_2. \tag{6.6}$$

Where; first coefficient ($k_1$) can be treated as a known constant by setting its value to a small positive constant, e.g. in this paper for both IMs ($k_1 = 0.001$). Note that the value of the first coefficient ($k_1$) is selected using trial and error. This was achieved while the measured speed, from encoder, was used to drive the motor. The second coefficient ($k_2$), which is unknown, can conveniently be incorporated in the gains of the PI controller (adaptation mechanism). Hence, for implementing the proposed scheme the initial measured nominal values of the stator resistance and inductance, and the leakage coefficient are no longer required.

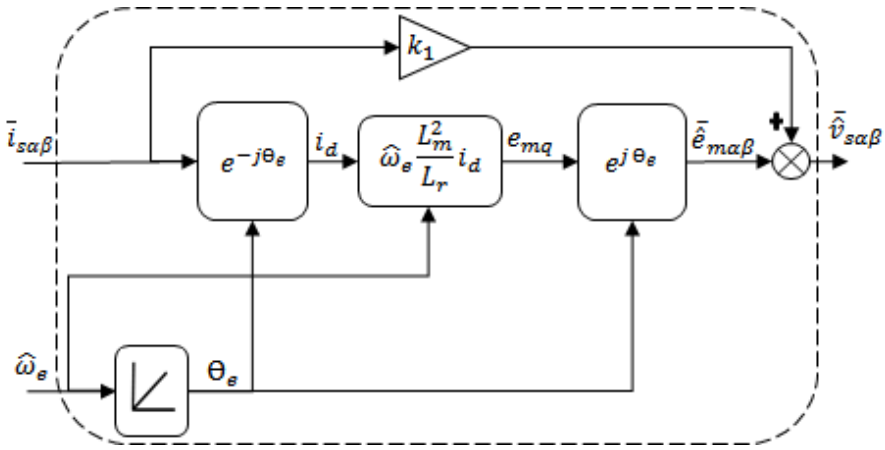


**Fig. 6.4. Signal flow diagram of the adjustable model of the proposed Vs-MRAS scheme.**

The back-EMF estimation in (6.5) requires synchronous speed ($\hat{\omega}_e$) which includes the estimated value of synchronous speed ($\hat{\omega}_{ePI}$), from the output of the adaptation mechanism, and a speed constant ($\omega_{const}$).

$$\hat{\omega}_e = \hat{\omega}_{ePI} + \omega_{const}. \tag{6.7}$$

Where;

$$\hat{\omega}_{ePI} = \left(k_p + \frac{K_i}{s}\right) * \left(\bar{\hat{v}}_{s\alpha\beta} \otimes \bar{v}^*_{s\alpha\beta}\right). \tag{6.8}$$

The speed constant ($\omega_{const}$), which is dependent on the sign of the reference q-axis current, helps the sensorless vehicle start from standstill in the correct direction that is requested by the driver.

$$\omega_{const} = \begin{cases} \omega_{const} = 1 \; for \; i_q^* > 0 \\ \omega_{const} = 0 \; for \; i_q^* = 0 \\ \omega_{const} = -1 \; for \; i_q^* < 0 \end{cases}. \tag{6.9}$$

Hence, utilising the proposed scheme eliminates the requirement for slip calculation, which is normally required in IRFOC for the synchronous speed calculation and is dependent on the rotor resistance.

In order to prove the overall stability of the proposed scheme and guaranteeing that the estimated speed converges to the actual speed, the Lyapunov stability function is employed [23]. By subtracting the outputs of the reference model from the adaptive model, the error vector based on the stator voltage components can be constructed as:

$$\bar{\epsilon}_{v_{s\alpha\beta}} = \bar{v}^{*}_{s\alpha\beta} - \bar{\hat{v}}_{s\alpha\beta}. \tag{6.10}$$

In order to derive the state error equations the following assumptions are made;

$$\begin{cases} x_\alpha = \dot{\omega}_e K_{\psi_d} sin(\theta_e) \\ x_\beta = -\dot{\omega}_e K_{\psi_d} cos(\theta_e). \\ \ddot{\omega}_e = 0 \end{cases} \tag{6.11}$$

Hence, by differentiating both sides of (6.10) and employing (6.11), the state error equations can be expressed as below;

$$\dot{\bar{\epsilon}}_{\alpha\beta} = [A][\bar{\epsilon}_{\alpha\beta}] - [W]. \tag{6.12}$$

Where; $\bar{\epsilon}_{\alpha\beta} = \begin{bmatrix} \epsilon_{v_{s\alpha}} \\ \epsilon_{v_{s\beta}} \\ \epsilon_{x_\alpha} \\ \epsilon_{x_\beta} \end{bmatrix}$ is the error vector, $A = \begin{bmatrix} 0 & \omega_e & -1 & 0 \\ -\omega_e & 0 & 0 & -1 \\ 0 & 0 & 0 & -1 \\ 0 & 0 & 1 & 0 \end{bmatrix}$, and $W = \bar{\hat{v}}_{s\alpha\beta} \otimes (\omega_e - \hat{\omega}_e)$.

According to the Lyapunov function of the linear part in (6.12), the Lyapunov function ($V$) is selected as the following [23];

$$V = \bar{\epsilon}^{T}_{\alpha\beta} \bar{\epsilon}_{\alpha\beta} > 0. \tag{6.13}$$

Differentiating both sides of (6.13), we have;

$$\dot{V} = \dot{\bar{\epsilon}}^{T}_{\alpha\beta} \bar{\epsilon}_{\alpha\beta} + \bar{\epsilon}^{T}_{\alpha\beta} \dot{\bar{\epsilon}}_{\alpha\beta} = \bar{\epsilon}^{T}_{\alpha\beta} (A^T + A) \bar{\epsilon}_{\alpha\beta} = -I \bar{\epsilon}^{T}_{\alpha\beta} \bar{\epsilon}_{\alpha\beta}. \tag{6.14}$$

Where;

$$I = \begin{bmatrix} 0 & 0 & 1 & 0 \\ 0 & 0 & 0 & 1 \\ 1 & 0 & 0 & 0 \\ 0 & 1 & 0 & 0 \end{bmatrix} \tag{6.15}$$

A function is said to be asymptotically stable if the following conditions are satisfied [95]:

$$\begin{cases} 1)\ V = 0\ for\ \hat{\omega}_e = 0 \\ 2)\ V > 0\ for\ \left|\left|\hat{\omega}_e\right|\right| \neq 0 \\ 3)\ \dot{V} \leq 0 \quad \forall \hat{\omega}_e \end{cases} \tag{6.16}$$

Considering (6.13), it is clear that conditions one and two of (6.16) are satisfied. Moreover, (6.14) also satisfies the third condition in (6.16). Hence, it can be stated that the proposed scheme is asymptotically stable.

## 6.4 Results and Discussion

In this section, simulation and experimental results and discussion are presented to evaluate the effectiveness of the proposed scheme for different operating conditions. The performance of the proposed scheme is compared against that of the conventional back-EMF MRAS scheme, using dynamometer setup. The recorded behaviour of the proposed scheme implemented on the electric golf buggy is also presented.

### 6.4.1 Simulation results

The behaviour of the proposed and conventional back-EMF MRAS schemes were evaluated, using simulation, for different torque levels with 100% stator resistance variation. To carry out this test, the nominal value of the stator resistance in the IM model was increased by 100%. During this test the measured speed was recorded from the output of the IM model and compared against the estimated speed. The applied torque command value was also compared with the measured torque value from the output of the IM model. The results of this test for the conventional and proposed schemes are shown in Fig. 6.5-(a) and -(b), respectively. From these results, it is clear that the conventional back-EMF MRAS fails to start from standstill when stator resistance is increased by 100%. However, from the results of the proposed Vs-MRAS scheme it can be seen that a successful sensorless starting from standstill can be achieved regardless of 100% stator resistance variation. Note that 100% increase in the stator resistance can cause oscillations in the estimated speed which can be a disadvantage of the proposed scheme.

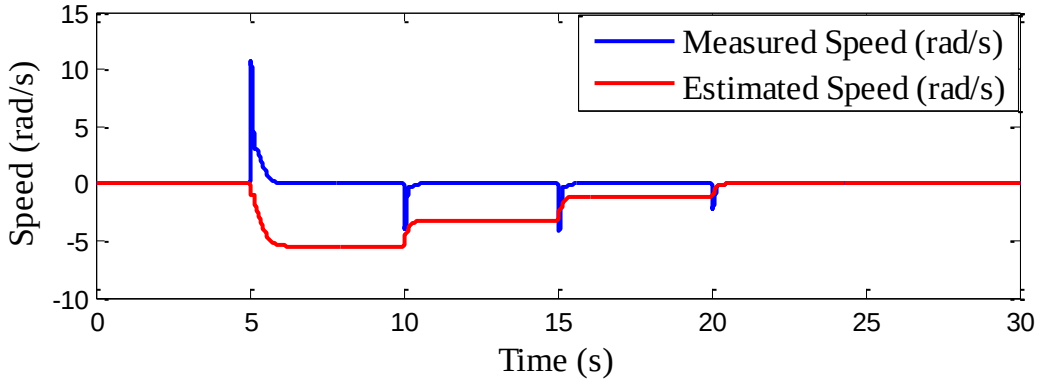


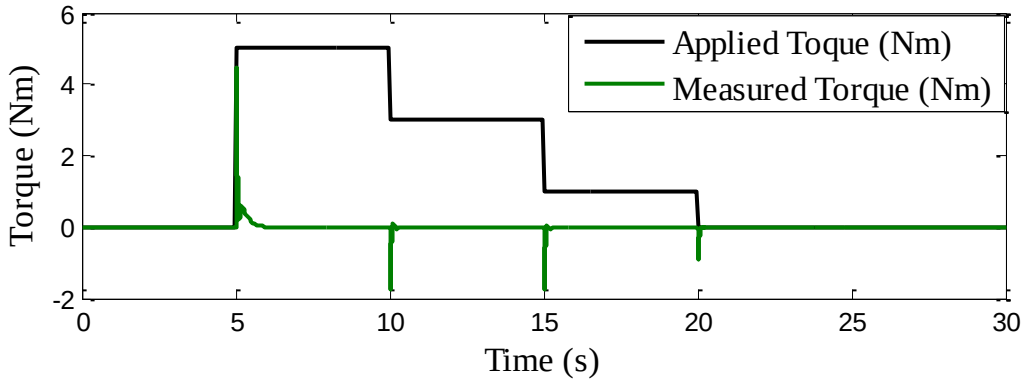


(a)

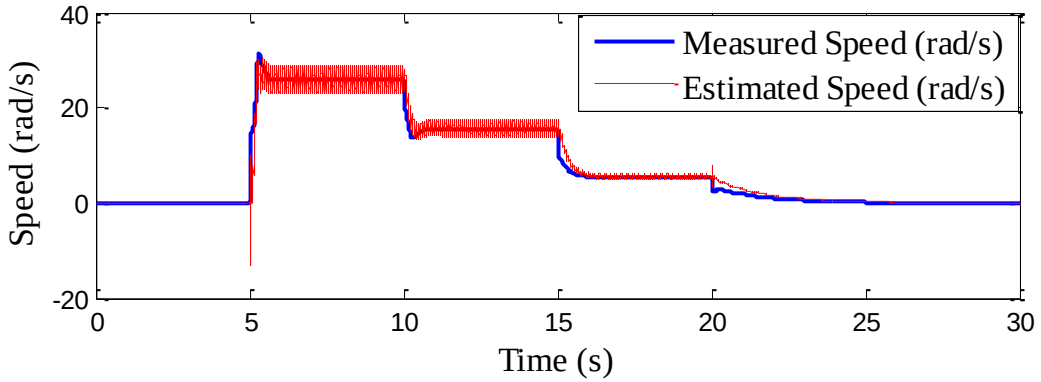


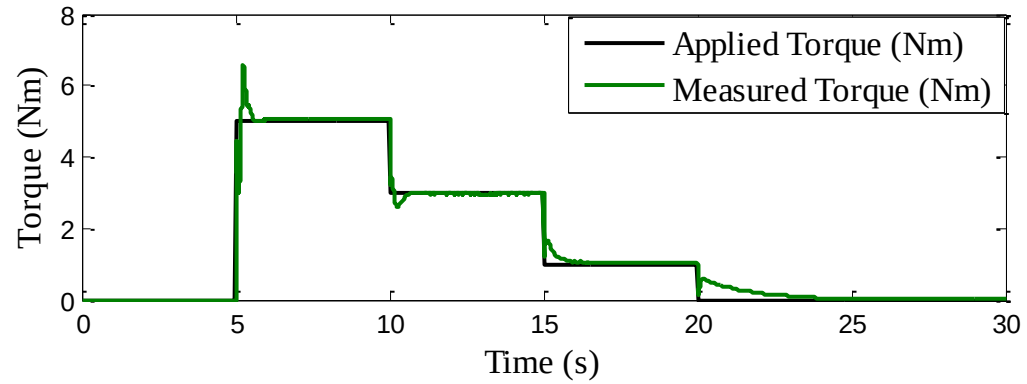


**(b)**

**Fig. 6.5. Simulation results for different torque level with 100% stator resistance variation. (a) The conventional back-EMF MRAS scheme and (b) the proposed Vs-MRAS scheme.**

### 6.4.2 Experimental results from dynamometer setup

All of the experiments were conducted in sensorless mode. For the purpose of validation, the estimated rotor speed has been compared against the measured rotor speed. In these tests the measured (from encoder) and estimated (from sensorless scheme) speeds were recorded using the DVT software on a laptop. The tuning procedure of PI controllers described in [5] is also used for the proposed scheme, which is as follows:

At first, the identical compensator PI controllers' gains were set to zero. Next, to obtain the optimal dynamic performance, the adaptation PI controller gains were tuned whilst the encoder signal was used for the transformation between reference frames. The proportional gain was gradually increased, while the integral gain was set to zero, until the speed from estimator could approximately track the actual speed. Then the integral gain was increased to achieve faster dynamic response. After the described procedure was carried out, both gains of the compensator PI controllers were set to one which results in a small steady state error. The error is derived to zero by gradually reducing both gains. Using the aforementioned procedure, for experiments on the dynamometer test bench, the adaptation PI controller gains of the conventional and proposed schemes were set to ( $K_p = 1 \; and \; K_i = 0.1$ ) and ( $K_p = 0.5 \; and \; K_i = 0.05$), respectively. The gains of the compensator PI controllers in the reference model of the proposed scheme were set to ($k_{p\gamma} = 0.8 \; and \; k_{i\gamma} = 0.001$). For experiments on the golf buggy, the adaptation PI controller gains of the proposed schemes were set to ($K_p = 0.6 \; and \; K_i = 0.04$). The gains of the compensator PI controllers in the reference model of the proposed scheme were set to ($k_{p\gamma_{comp}} = 0.9 \; and \; k_{i\gamma_{comp}} = 0.002$).

The above procedure for tuning gains of PI controllers is based on trial and error. Therefore, a systematic approach such as auto-tuning, e.g. Zieglar-Nichols tuning, can improve the tuning procedure.

#### *6.4.2.1 Starting from Standstill with Nominal Parameters*

Consistency in reliable starting from standstill with correct direction of that requested is essential in the EV applications. Therefore this test was carried out to demonstrate capability of the conventional and the proposed schemes for starting from standstill. In this test the IM was driven without load in the forward and reverse directions while the command torque of +2 Nm and -2 Nm were applied, respectively. This test was carried out in two attempts for each direction. From the result of the conventional scheme, shown in Fig. 6.6-(a), it is clear that, this

scheme is inconsistent when starting from standstill. It can be seen that for the applied torque of -2 Nm, at 47 s, the drive became unstable and accelerated in the opposite direction to which was requested. However, from the result of the proposed scheme shown in Fig. 6.6-(b) it is obvious this scheme is capable of performing consistent and reliable starting from standstill in both directions.

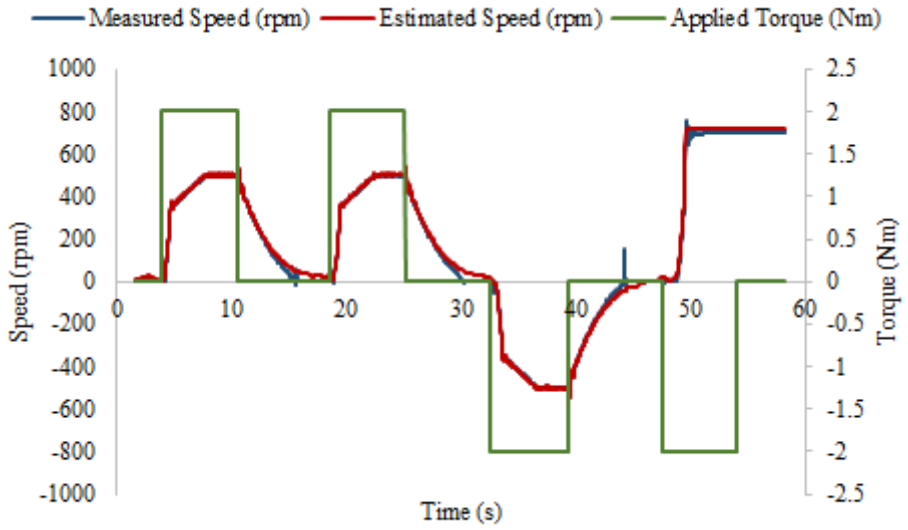


**(a)**

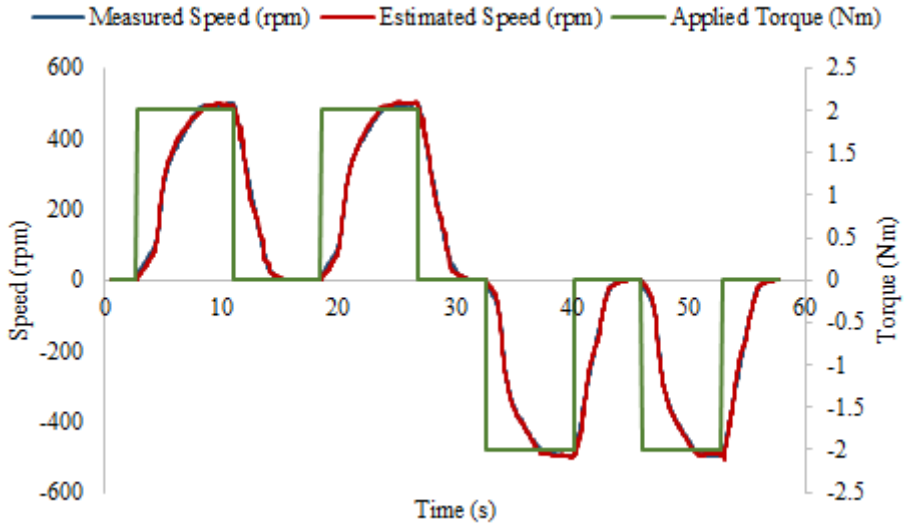


(b)

**Fig. 6.6. Experimental results for sensorless performance starting from standstill with nominal parameters without load. (a) Conventional Back-EMF MRAS (b) the proposed Vs-MRAS.**

#### *6.4.2.2 Sensitivity to stator resistance variation for 50% increase*

This test was carried out to demonstrate the performance of the conventional Back-EMF and the proposed Vs-MRAS schemes against the stator resistance variations. In this test, for both schemes, a voltage value equal to ($0.5R_s\bar{\imath}_{s\alpha\beta}$) was added to the input voltage components of the reference model. The result of the conventional scheme is shown in Fig. 6.7-(a) which clearly shows that this scheme is very sensitive to stator resistance variation and become unstable in the low speed region. Fig. 6.7-(b) shows the result for the proposed scheme which is clear that the estimated speed closely follows the measured speed. Hence the proposed scheme is robust to stator resistance variation and performs stably in both directions.

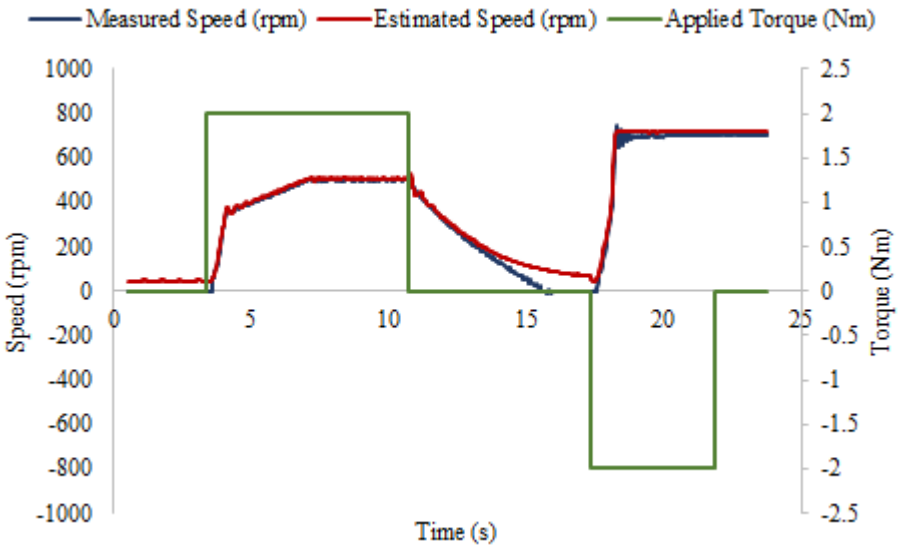


**(a)**

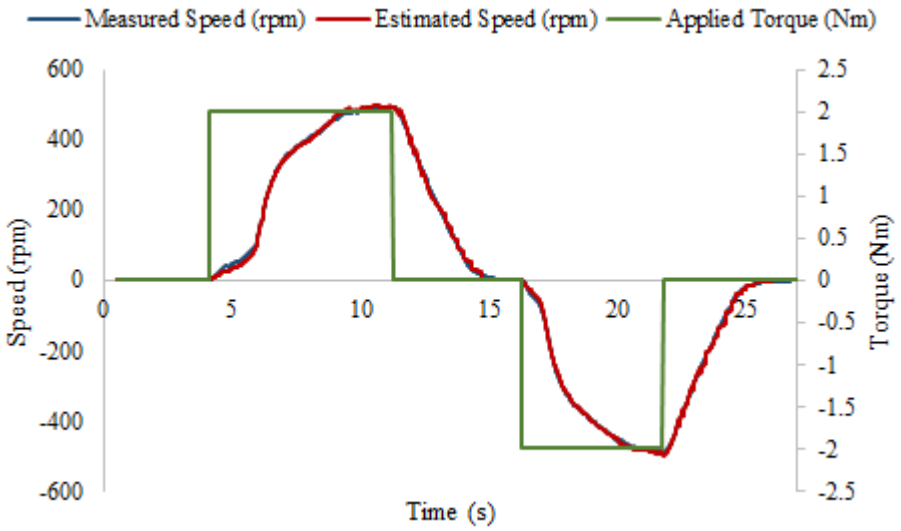


**(b)**

**Fig. 6.7. Experimental results for sensorless performance with 50% increase in the stator resistance without load. (a) Conventional Back-EMF MRAS (b) the proposed Vs-MRAS.**

#### *6.4.2.3 Sensitivity to magnetising inductance variation for 50% reduction*

The magnetising inductance can reduce to half of its nominal value due to the effect of saturation. Therefore, this test carried out to demonstrate the capability of the conventional and the proposed scheme while magnetising inductance is reduced by 50% in the estimator model. During these tests the shaft speed was varied from standstill to 3000 rpm, approximately twice the rated base speed of the IM, utilising a speed throttle connected to the SPMSM. Using both conventional and proposed scheme, a 30 Nm torque command applied from start. This test was also carried out for the proposed scheme when compensator mechanism was not employed. The speed tracking capability of both schemes and estimated rotor flux from estimator models are shown in Fig. 6.8-Fig. 6.10. Note that a moderate level of oscillations is expected when 30 Nm torque command is applied at standstill regardless of scheme used. From results of the conventional scheme, shown in Fig. 6.8, it can be seen that this scheme starts with excessive level of oscillations at start and completely loses control at around 2800 rpm. The performance of the proposed scheme without compensating mechanism, shown in Fig. 6.9, is much better than the conventional scheme, especially in the field weakening region. However, the proposed scheme without compensating mechanism has some oscillations and can become unstable during operations in the field weakening region. Although the proposed scheme with compensating mechanism, shown in Fig. 6.10, has some oscillations, this scheme remains stable throughout the field weakening region, twice the base speed, and also low speed regions. Hence, it can be stated that in spite of 50% magnetising inductance the proposed scheme with compensating mechanism remains stable over a wide range of speeds, especially in the field weakening region.

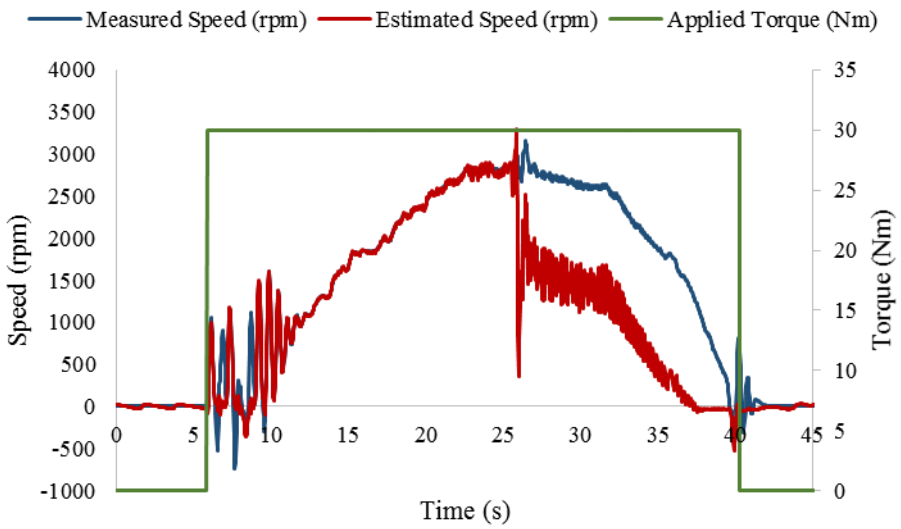


**(a)**

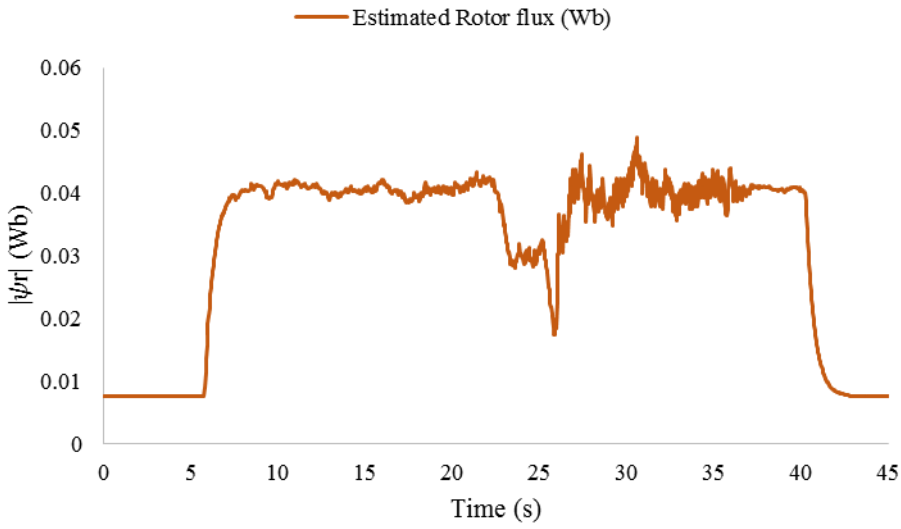


(b)

**Fig. 6.8. Experimental result for sensorless performance using conventional Back-EMF MRAS scheme during 50% reduction in magnetising inductance. From standstill to 3000 rpm at 30 Nm. (a) Speed tracking performance, and (b) estimated rotor flux from the estimator model.**

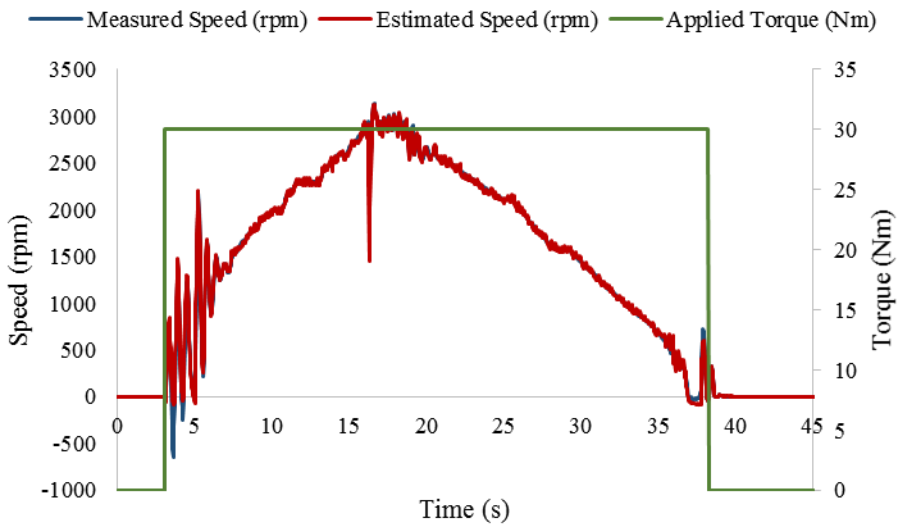


**(a)**

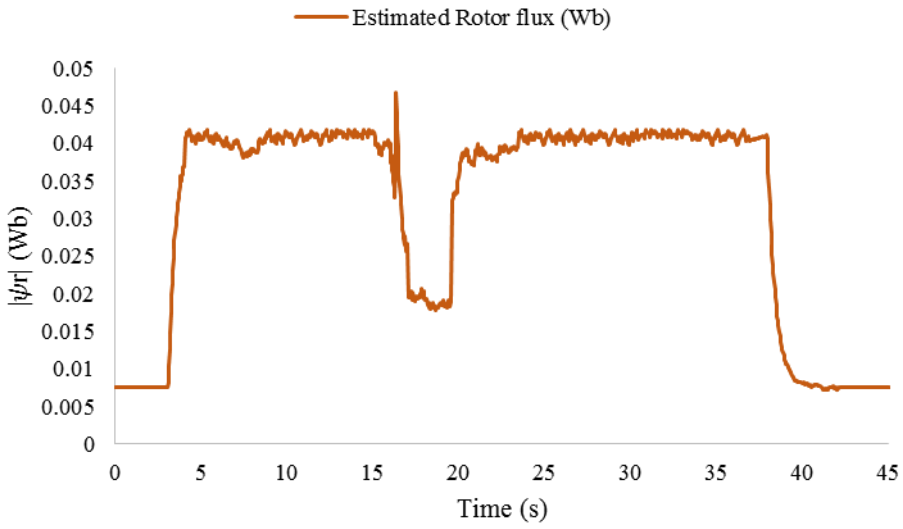


(b)

**Fig. 6.9. Experimental result for sensorless performance using the proposed Vs-MRAS scheme without compensating mechanism during 50% reduction in magnetising inductance. From standstill to 3000 rpm at 30 Nm. (a) Speed tracking performance, and (b) estimated rotor flux from the estimator model.**

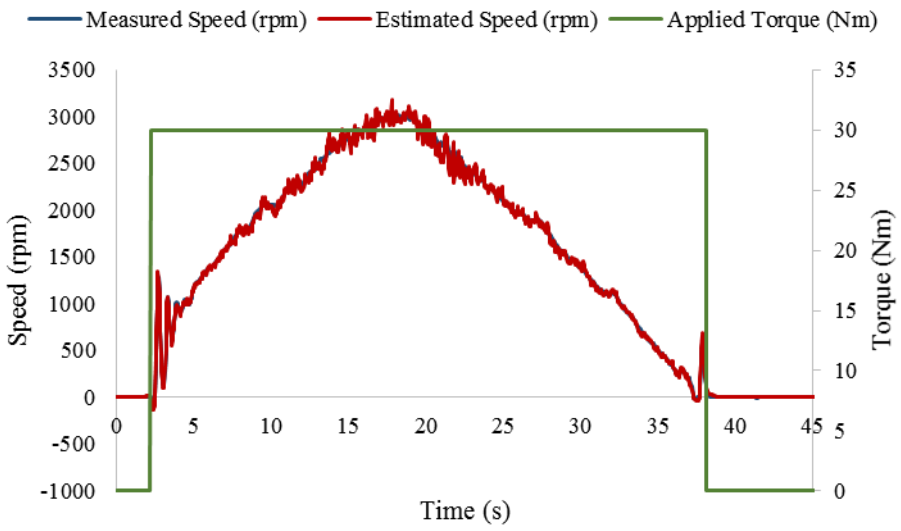


**(a)**

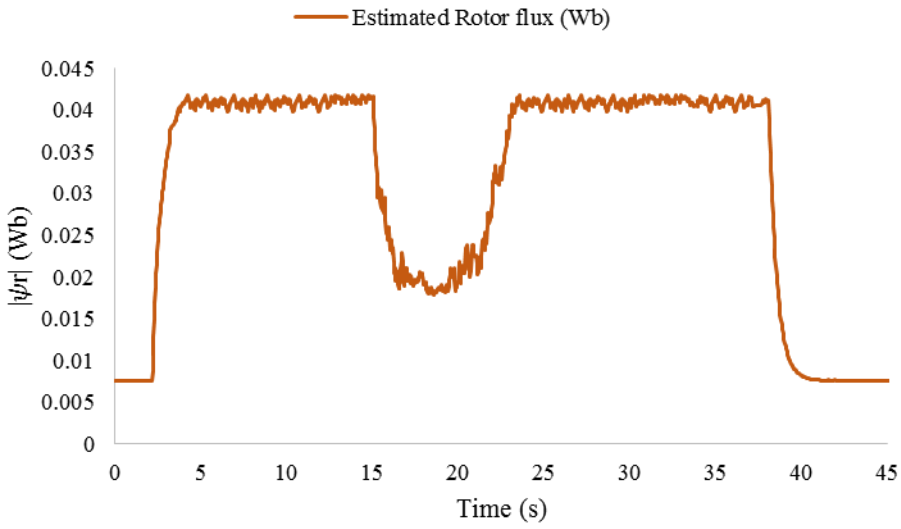


(b)

**Fig. 6.10. Experimental result for sensorless performance using the proposed Vs-MRAS scheme, with compensating mechanism, during 50% reduction in magnetising inductance. From standstill to 3000 rpm at 30 Nm. (a) Speed tracking performance, and (b) estimated rotor flux from the estimator model.**

### *6.4.2.4 Constant speed operation with different torque levels*

This test was carried out to demonstrate the behaviour of the proposed scheme at constant speed with load torque variations. For this test the shaft speed was kept constant at 400 rpm with the applied torque command varied in 5 Nm intervals from 5 Nm to 60 Nm. For this test the speed tracking capability of both schemes, and stator current components in the synchronous

reference frame were recorded. Results of this test are shown in Fig. 6.11 and Fig. 6.12 for the conventional and proposed schemes, respectively. From results of the conventional scheme it is clear that this scheme has significant oscillations, and at 55 Nm it completely loses stability. Hence, the estimated speed no longer tracks the measured speed. On the contrary, from results of the proposed scheme is clear that the estimated speed continuously tracks the measured speed closely regardless of variations in the torque command level.

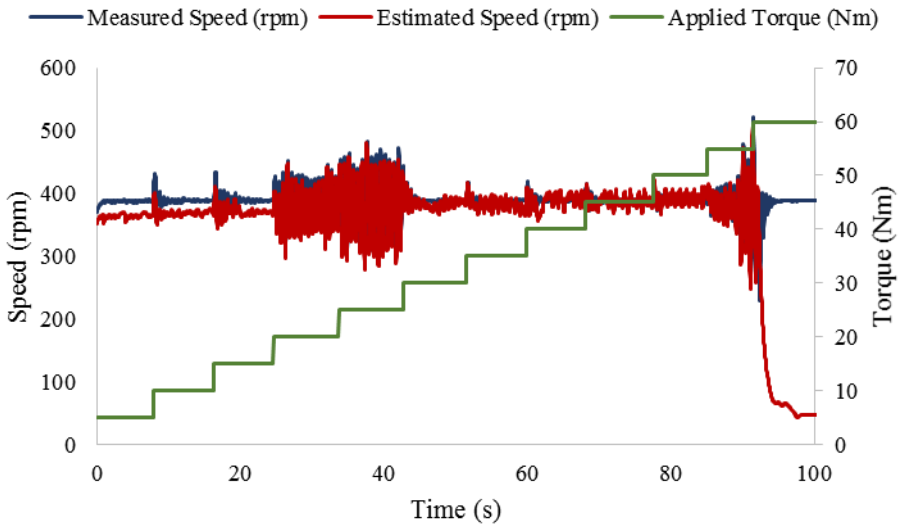


**(a)**

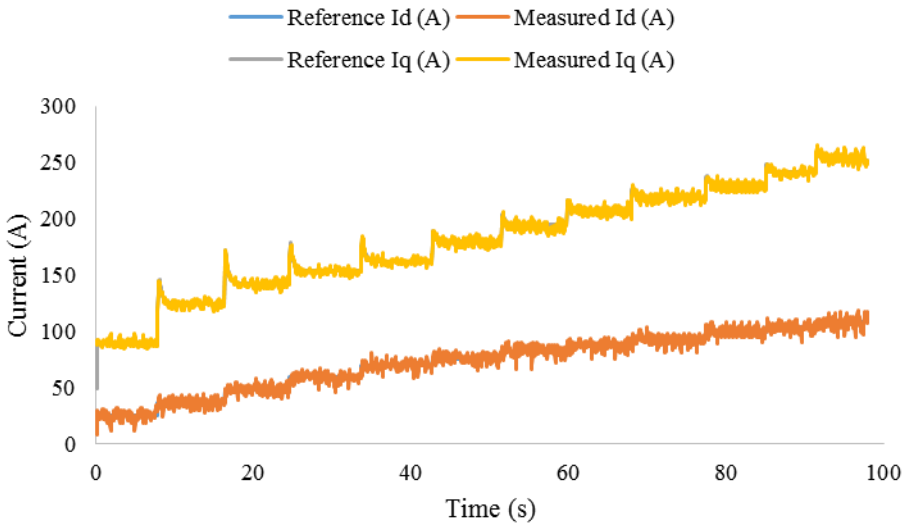


(b)

**Fig. 6.11. Experimental result for sensorless performance using conventional Back-EMF MRAS scheme at constant speed in region of 400 rpm with the torque command increased in 5 Nm intervals from 5 Nm to 60 Nm. (a) Speed tracking performance (b) stator current components.**

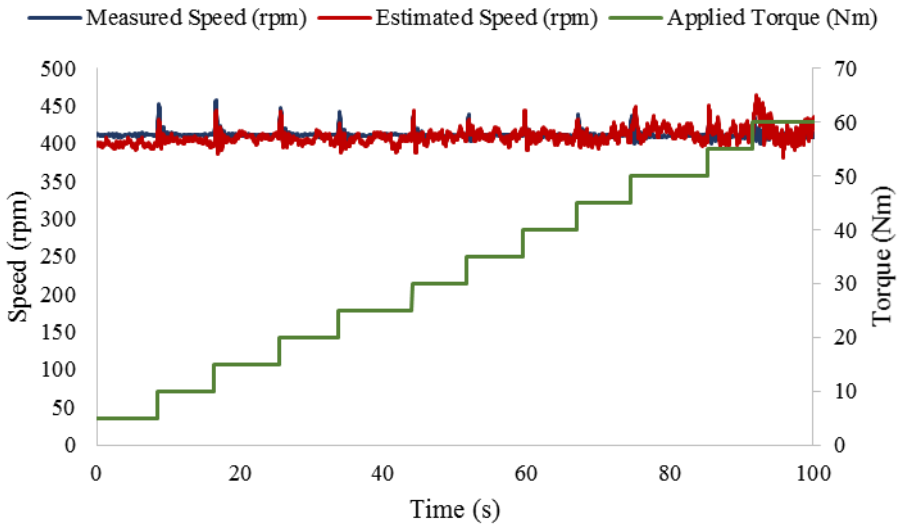


**(a)**

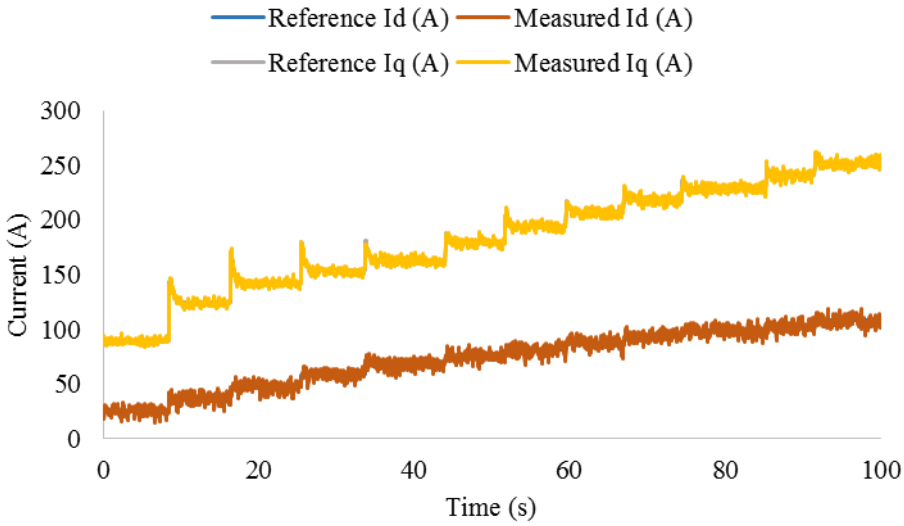


(b)

**Fig. 6.12. Experimental result for sensorless performance using the proposed Vs-MRAS scheme at constant speed in region of 400 rpm with the torque command increased in 5 Nm intervals from 5 Nm to 60 Nm. (a) Speed tracking performance (b) stator current components.**

### 6.4.3 Experimental results from golf buggy

The proposed scheme was implemented and tested on a golf buggy. For these tests the estimated synchronous speed, utilising the proposed scheme, was employed in the controller. The measured speed, from encoder, was only used for validation which is labelled as "Measured Speed" in the recorded results. Results were recorded by a laptop using DVT software. During these tests forward, park and reverse operation modes were manually selected using the vehicle's gear stick and torque command applied using accelerator pedal.

#### *6.4.3.1 Consistent vehicle-starting from standstill*

Consistency and reliability of the vehicle starting from standstill in the direction requested by the driver is critical when a sensorless drive employed for an EV application. Thus this test carried out to illustrate the performance of the proposed scheme for consecutive vehicle-starting in the forward and reverse operation modes. During this test the vehicle was driven in forward mode and then slowed down back to zero for three consecutive attempts. The same procedure also was repeated in the reverse direction. Vehicle test-drive result of this test is shown in Fig. 6.13. From the recorded result it is clear that utilising the proposed scheme provides a consistent vehicle-starting from standstill in both forward and reverse operation modes.

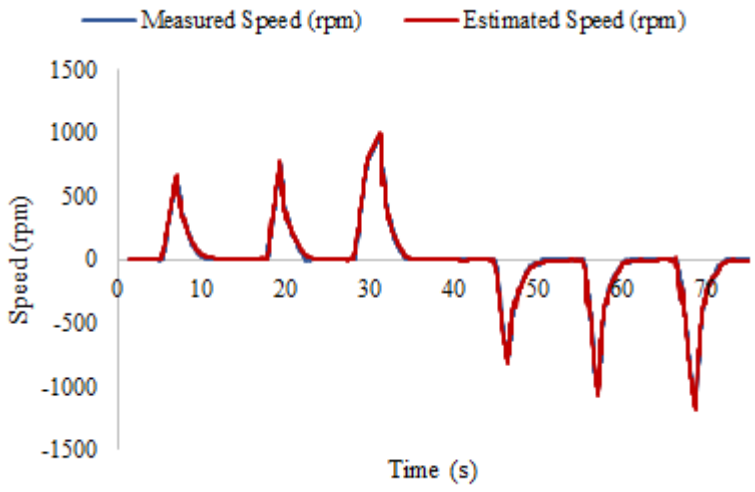


**Fig. 6.13. Experimental results using the Golf buggy. Sensorless vehicle test-drive for 3 attempts starting from standstill in forward and reverse drive modes.**

### *6.4.3.2 Smooth Forward and Reverse Test-Drive of golf buggy in wide speed range*

A sensorless drive which is employed for an EV application is required to be capable of performing in wide range of speeds, including the field weakening region. Therefore this test was carried out to demonstrate behavior of the proposed scheme for the sensorless drive in forward, park and reverse operation modes in a wide range of speeds including the field weakening region. During this test the vehicle was accelerated forward to around +2950 rpm and then slowed down to zero and the same procedure was repeated for the reverse direction for the speed around -2950 rpm. The result of this test is shown in Fig. 6.14, which confirms the capability and reliability of the proposed scheme across the whole speed range. The test-drive movement of the vehicle was smooth and without any cogging feelings at the vehicle-starting from standstill.

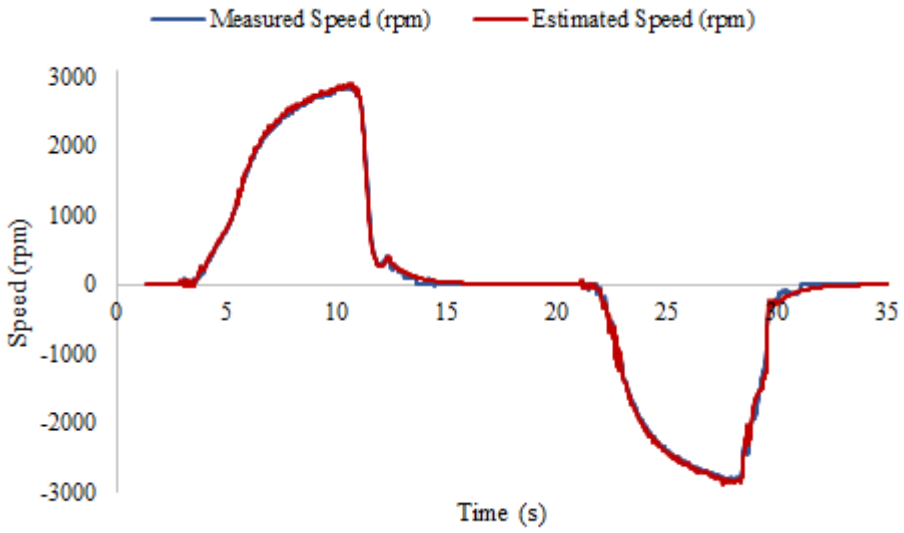


**Fig. 6.14. Experimental results using the Golf buggy. Sensorless vehicle test-drive in forward and reverse drive modes from standstill over a wide range of speeds.**

### *6.4.3.3 Vehicle hill-starting performance*

This test was carried out to demonstrate the robustness of the proposed scheme during vehicle hill-starting test. This experiment was carried out using a 15 degree ramp, which is especially designed for hill-starting tests. This test was carried out while the vehicle was at standstill on the ramp. The result of this test is shown in Fig. 6.15. In order to prevent the vehicle from rolling backwards a torque command of around 4 Nm was applied, using an accelerator

pedal. Then the vehicle was slowly driven forward, by gradually increasing the torque command, and slowed back to standstill by gradually easing the accelerator pedal to reduce the torque command back to around 4 Nm again. From the result it is clear that the vehicle did not roll backward while it was on the ramp and a reliable vehicle hill-starting can be achieved utilising the proposed scheme.

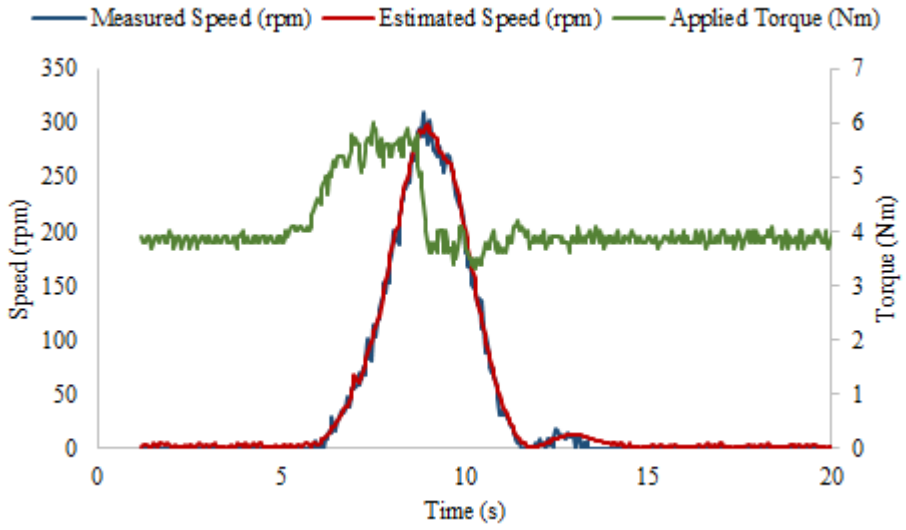


**Fig. 6.15. Experimental results using the Golf buggy. Sensorless vehicle test-drive for hill-starting from standstill in forward mode.**

## 6.5 Conclusion

The proposed novel Vs-MRAS for sensorless TCD of IM for the purpose of *limp-home* mode of EV applications was successfully implemented in the lab environment and on the golf buggy. The proposed scheme is relatively easy to implement and is independent from the prerequisite measured nominal values of stator resistance and inductance, and rotor resistance. Results of the proposed scheme confirm that this scheme is robust against parameter variations and is stable in the low speed regions. Results recorded while the proposed scheme was applied on the golf buggy confirm that a safe and consistent vehicle-starting and hill-starting from standstill can be achieved, with correct direction to that requested. More importantly, it provides a smooth and stable drive in a wide speed range, including the field weakening region. Therefore the proposed Vs-MRAS has proven to be a suitable scheme to be employed for *limp-home* mode operation in the EV/HEV applications by providing a reliable and smooth drive in a wide speed range.

The proposed scheme has the potential of being employed as a universal senseless scheme for IM and SPMSM. However, to employ this scheme for sensorless control of SPMSM, it is required to be hybridised using a HFSI scheme at zero and low speed regions. Developing a universal hybrid scheme will be the purpose of the next chapter.

# CHAPTER 7. UNIVERSAL SENSORLESS CONTROL OF AC MOTORS BASED ON HYBRID VS-MRAS

A novel universal sensorless scheme is described for AC motor drives based on a new HVs-MRAS. The presented sensorless scheme is employed for the purpose of *limp-home* mode in EV applications based on IRFOC technique. The scheme benefits from simplicity and robustness of the new Vs-MRAS, in the medium and high speed regions, and combined with the HFSI, for the low speed region, which provides a consistent and reliable sensorless drive over a wide range of speed, including the field weakening region. Unlike other sensorless schemes in the literature, the proposed HVs-MRAS is robust against motor parameter variations. The proposed scheme has been experimentally verified using the test setup, with the 19 kW IM and the 10 kW SPMSM. The scheme has also been implemented on two electric golf buggies. Results confirm the suitability of the scheme for EV applications.

## 7.1 Introduction

The HFSI based schemes are more suitable for the zero and low speed regions as the techniques used are independent of motor parameters. However, utilising these techniques in medium and high speed regions can incur additional losses and a reduction in control bandwidth [64]. In contrast, the fundamental model based schemes rely on calculation of the induced back-EMF to estimate rotor speed or position. These schemes are well suited for medium and high speed operations [62]. In the low speed region as the back-EMF is reduced, the influence of parameter variations and measurement noise become more important [53, 62]. These effects can cause the performance of the model based schemes to degrade and at zero speed even become completely instable [44, 62].

In order to design a robust sensorless algorithm with the capability of operating over a wide speed range, schemes based on a combination of the HFSI and the fundamental model have been widely employed in literature [56, 58, 62, 63, 65]. Although these approaches have different structures, they all follow the same principle the HFSI scheme is used for the zero and low speed regions, and a model based scheme is used for the medium and high speed regions. These schemes are normally amalgamated using a combining (or blending) function. A limitation of the aforementioned schemes is that they are designed and work with only a specific type of motor.

In this chapter a universal combined sensorless TCD using IRFOC based on a new universal HVs-MRAS is proposed. Unlike the other combined sensorless approaches, the proposed scheme can be employed for an IM or a SPMSM. Moreover the proposed scheme is robust against; parameter variations and errors due to digitisation in the high speed regions. The performance is first demonstrated with dynamometer testing, based on the 19 kW IM and the 10 kW SPMSM. Further tests are carried out with two electric golf buggy vehicles powered by 5 kW IM and 5 kW SPMSM, respectively. Experimental results for IM demonstrate the advantages of the proposed scheme over the conventional back-EMF MRAS [20] scheme, in tests including; sensorless starting from standstill and sensitivity to motor parameter variations. Both vehicles test–drives, utilising the proposed scheme, confirm the stability and reliability in the sensorless vehicle starting from standstill plus a wide speed range drive, including operation in the field weakening region.

The structure of this chapter is as follows; Section 7.2 describes universal sensorless TCD of AC motors using IRFOC. Section 7.3 gives a detailed description of the proposed scheme. Section 7.4 shows the experimental results of the proposed sensorless scheme. Finally, conclusions provided in Section 7.5.

## 7.2 Universal Sensorless TCD of AC motors based on IRFOC using HVs-MRAS

The overall block diagram of the universal sensorless TCD for AC motors based on IRFOC used in this chapter is shown in Fig. 7.1. In the absence of a speed/position sensor, a sensorless scheme is required for rotor flux angle estimation. Regarding TCD for the IM, the slip is normally required to be calculated from reference d-q current components in the synchronous reference frame, which is then added to the estimated electrical rotor speed. However, slip calculation is no longer required when the proposed scheme is employed as it estimates the synchronous speed directly. The reference d-axis current value is provided using a LUT and the value of the reference q-axis current is calculated from torque equation using the applied torque from accelerator pedal. A LPF is required to cancel out high frequency signals on the measured d-axis current ($i_d$). The carrier signal does not appear on the q-axis and hence, it does not need to be low-pass filtered [54].

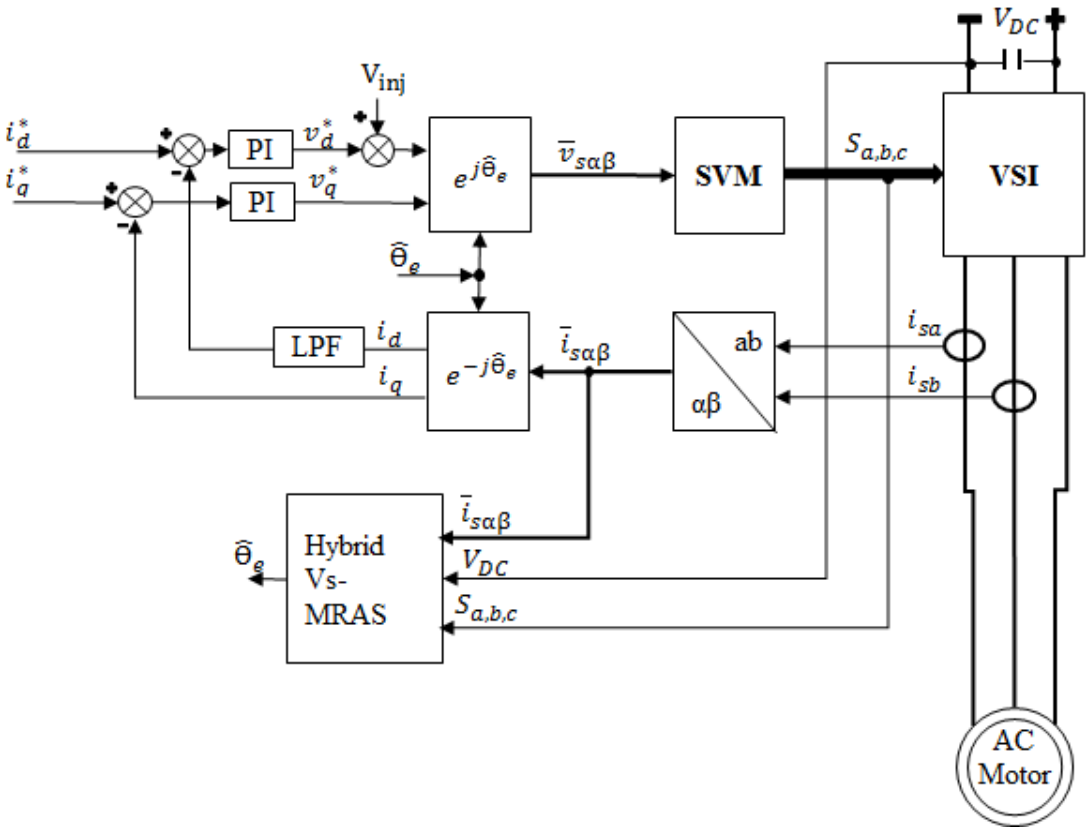


**Fig. 7.1. Overall block diagram of the universal hybrid sensorless torque controlled-drive based on IRFOC.**

## 7.3 Proposed universal hybrid stator voltage MRAS scheme

A block diagram of the proposed universal HVs -MRAS scheme is shown in Fig. 7.2. The reference model, is similar to Fig. 6.3, takes in the reconstructed stator voltage, from the measured DC-link voltage and the switching signals, and the estimated stator voltage components in the stationary reference frame. In return it provides reference stator voltage components in the stationary reference frame. The reference model benefits from two identical compensators, similar to the one presented in [5]. This approach is taken to deal with parameter variations and errors in the high speed regions due to digitisation.

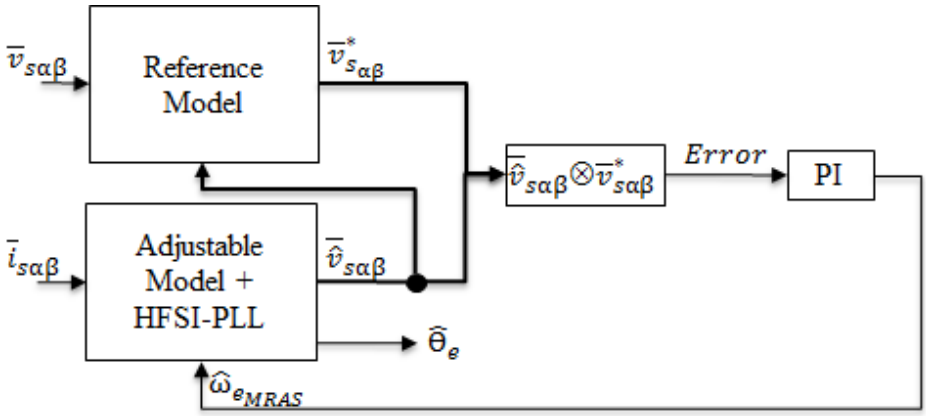


**Fig. 7.2. Block diagram of proposed universal hybrid stator voltage MRAS.**

The estimated stator voltage components are calculated from an adjustable model, which its signal flow diagram is shown in Fig. 7.3. It consists of a PLL mechanism for demodulation of the HFSI carrier, similar to Fig. 7.4 which is utilised in the zero and low speed regions, an adjustable stator voltage model, which is utilized for medium and high speed regions. A simple transition function is also employed, which is designed for soft switching between both estimated synchronous speeds. Hence, during transition the estimated synchronous speed is smooth and free from ripple. The adjustable model of the MRAS schemes, previously presented for IM [19, 20, 34], are usually designed to be dependent on the estimated rotor speed ($\hat{\omega}_r$). Hence, for the rotor flux angle ($\hat{\theta}_e$) estimation, the slip ($\omega_{sl}$) is required to be calculated. However, in the proposed scheme the adjustable model is designed to be directly dependent on the estimated synchronous speed. Therefore, the output of the PI controller is the estimated synchronous speed ($\hat{\omega}_e$), hence, there is no requirement for the slip calculation. More importantly, it renders this scheme to be a more suitable candidate for a universal sensorless drive for both IM and SPMSM.

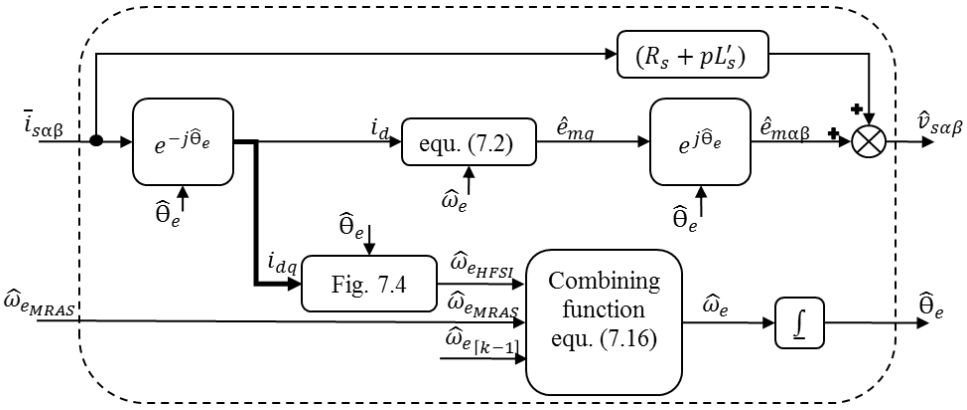


**Fig. 7.3. Signal flow diagram of the adjustable model of the proposed scheme.**

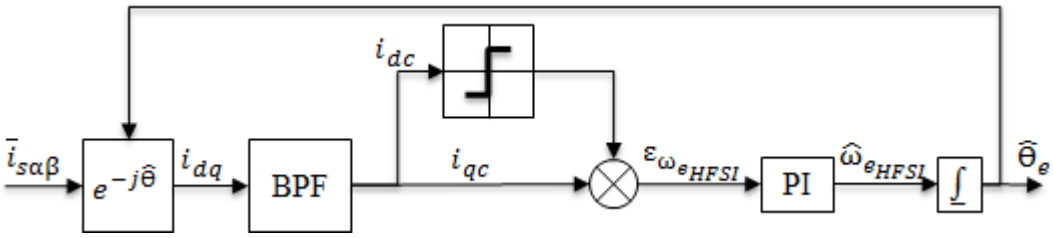


**Fig. 7.4. Signal flow diagram of the PLL mechanism used for demodulation of HFSI carrier.**

The detailed description of the proposed universal scheme is provided as follows; considering the stator voltage equations for the IM and SPMSM in the stationary reference frame, which can be expressed as given below:

$$\overline{v}_{s\alpha\beta} = (R_s + pL'_s)\overline{i}_{s\alpha\beta} + \overline{e}_{m\alpha\beta} \tag{7.1}$$

where, $L'_s = L_s\sigma$ and $L'_s = L_s$ for IM and SPMSM, respectively.

In order to design an adjustable model, which is dependent on the synchronous speed, the back-EMF components $\overline{e}_{m\alpha\beta}$ in (7.1) can be firstly calculated in the synchronous frame and then transformed into the stationary reference frame:

$$\overline{e}_{m\alpha\beta} = \overline{e}_{mdq}e^{j\theta_e} = \left(0 + j\omega_e k_\psi\right)e^{j\theta_e} \tag{7.2}$$

where;

$$k_\psi = \begin{cases} \dfrac{L_m^2}{L_r} i_d & ,for\ IM \\ \psi_{PM} & ,for\ SPMSM \end{cases}. \tag{7.3}$$

In order to design an adaptation mechanism for the proposed MRAS the state error equations are expressed as follows:

$$\dot{\epsilon}_{\alpha\beta} = [A]\left[\bar{\epsilon}_{\alpha\beta}\right] - [W]. \tag{7.4}$$

Where; $\left[\bar{\epsilon}_{\alpha\beta}\right] = \begin{bmatrix}(v_{s\alpha}^{*} - \hat{v}_{s\alpha})\\(v_{s\beta}^{*} - \hat{v}_{s\beta})\end{bmatrix}$ is error vector, $A = \begin{bmatrix}0 & -\omega_e\\ \omega_e & 0\end{bmatrix}$, and $W = (\omega_e - \hat{\omega}_e)\otimes - \bar{\hat{v}}_{s\alpha\beta}$.

To design an adaptation mechanism Popov's integral inequality [97] is employed, which is expressed as follows:

$$\int_0^{t_1} [\bar{\epsilon}]^T.[W]dt \geq -\gamma_0^2 \qquad for\ all\ \ t_1 \geq 0 \tag{7.5}$$

where; $\gamma_0^2$ is a positive real constant.

It is valid for the purpose of deriving an adaptation mechanism to assume that the synchronous reference speed is constant. Therefore by defining the estimated synchronous speed ($\hat{\omega}_e$) to be:

$$\hat{\omega}_e = \Phi_1([\epsilon]) + \int_0^t \Phi_2([\epsilon])dt \tag{7.6}$$

and substituting for $[W]$ and $\left[\bar{\epsilon}_{\alpha\beta}\right]$ from (7.4) in the integral inequality (7.5) and using the definition of $\hat{\omega}_e$ in (7.6), (7.5) becomes:

$$\begin{aligned}\int_0^{t_1} \left[\bar{\epsilon}_{\alpha\beta}\right]^T [W]dt \\ = \int_0^{t_1} \left(\epsilon_\alpha \hat{v}_{s\beta} - \epsilon_\beta \hat{v}_{s\alpha}\right)\Bigg[\omega_e - \Phi_1([\epsilon]) \\ - \int_0^t \Phi_2([\epsilon])dt\Bigg]dt \geq -\gamma_0^2.\end{aligned} \tag{7.7}$$

To solve the inequality in (7.7), the equation can be split into two separate inequalities, $I_1$ and $I_2$. Thus, we have:

$$\mathrm{I}_1 = \int_0^{t_1} \left(\epsilon_\beta \hat{v}_{s\alpha} - \epsilon_\alpha \hat{v}_{s\beta}\right)\Phi_1([\epsilon])dt \geq -\gamma_1^2 \tag{7.8}$$

$$\mathrm{I}_2 = \int_0^{t_1} \left(\epsilon_\beta \hat{v}_{s\alpha} - \epsilon_\alpha \hat{v}_{s\beta}\right)\left[\int_0^t \Phi_2([\epsilon])dt - \omega_e\right]dt \geq -\gamma_2^2 \tag{7.9}$$

if both of these inequalities, (7.8) and (7.9), are satisfied, it indicates that inequality (7.7) is

equally satisfied [97]. Regarding inequality (7.8), if the left side of the integral is positive, the inequality will be satisfied. To achieve this, a solution is to have:

$$\Phi_1([\epsilon]) = \left(\epsilon_\beta \hat{v}_{s\alpha} - \epsilon_\alpha \hat{v}_{s\beta}\right)k_1, \qquad k_1 \geq 0 \; for \; all \; t \geq 0. \tag{7.10}$$

Regarding inequality (7.9), the following well-known expression is used [19, 97],

$$\int_0^{t_1} \dot{f}(t) \, . \, k_2 f(t) \, dt \geq -\frac{k_2}{2} f^2(0), k_2 > 0 \tag{7.11}$$

selecting for $\dot{f}(t)$ and $k_2 f(t)$ in inequality (7.9) to be:

$$\dot{f}(t) = \left(\epsilon_\beta \hat{v}_{s\alpha} - \epsilon_\alpha \hat{v}_{s\beta}\right) \tag{7.12}$$

and

$$k_2 f(t) = \int_0^t \Phi_2([\epsilon])dt - \omega_e \tag{7.13}$$

By differentiating both sides of (7.13) with respect to time and using (7.12), we have:

$$\Phi_2([\epsilon]) = k_2 \dot{f}(t) = k_2\left(\epsilon_\beta \hat{v}_{s\alpha} - \epsilon_\alpha \hat{v}_{s\beta}\right). \tag{7.14}$$

Hence, Popov's integral inequality (7.5) can be satisfied by selecting (7.6) to be as follows:

$$\hat{\omega}_{e_{MRAS}} = \left(\epsilon_\beta \hat{v}_{s\alpha} - \epsilon_\alpha \hat{v}_{s\beta}\right)k_1 + \int_0^t \left(\epsilon_\beta \hat{v}_{s\alpha} - \epsilon_\alpha \hat{v}_{s\beta}\right)k_2 dt. \tag{7.15}$$

In order to combine both HFSI and Vs-MRAS a combining function is required, which has been designed as follows:

$$\hat{\omega}_e = \hat{\omega}_{e_{MRAS}} k_{SW} + \hat{\omega}_{e_{HFSI}}(1 - k_{SW}) \tag{7.16}$$

where, $k_{SW}$ is a positive soft switching constant.

The soft switching constant is calculated from:

$$k_{SW} = \frac{sign\left(\hat{\omega}_{e[k-1]}\right)\hat{\omega}_{e[k-1]}}{k_{\hat{\omega}_e}}, \qquad if \; k_{SW} > 1 \; then \; k_{SW} = 1. \tag{7.17}$$

Where; $k_{\hat{\omega}_e}$ is a positive constant, which represents the speed switch over between both schemes, which is set to be 5 rad/s in this chapter.

## 7.4 Results and discussion

In this section, experimental and simulation results and discussions are presented to evaluate the effectiveness of the proposed scheme for different operating conditions.

### 7.4.1 Simulation results

The behaviours of the proposed scheme for IM and SPMSM were evaluated, using simulation, for different torque levels with nominal parameters. During this test the measured speed was recorded from the IM and SPMSM models and compared against the estimated speed. The applied torque command value was also compared with the measured torque value from the output of the IM, and SPMSM model. The results of this test for the IM and SPMSM are shown in Fig. 7.5-(a) and (b), respectively. From these results, it is clear that the proposed universal sensorless control can be applied on both IM and SPMSM with the estimated speed closely tracking the measured speed for different applied torque demands. Note that simulating the effect of HFSI in Matlab/Simulink software is a difficult task and it requires a combination of both Matlab/Simulink and Magnet software. Therefore, for simulation results, instead of using the HFSI scheme at zero and low speed regions below 5 (rad/s), the measured speed, from motor models, is used.

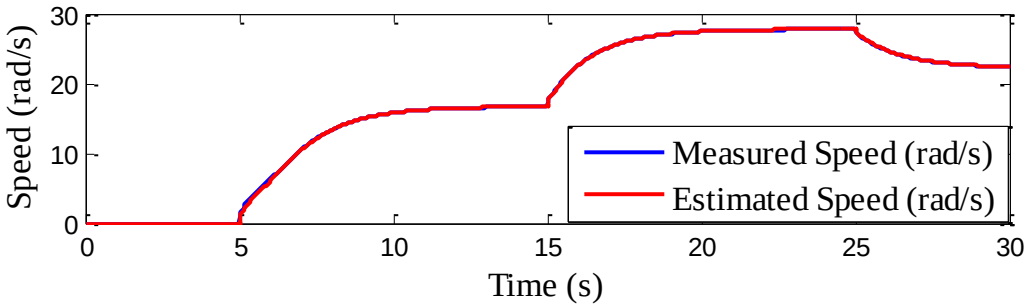


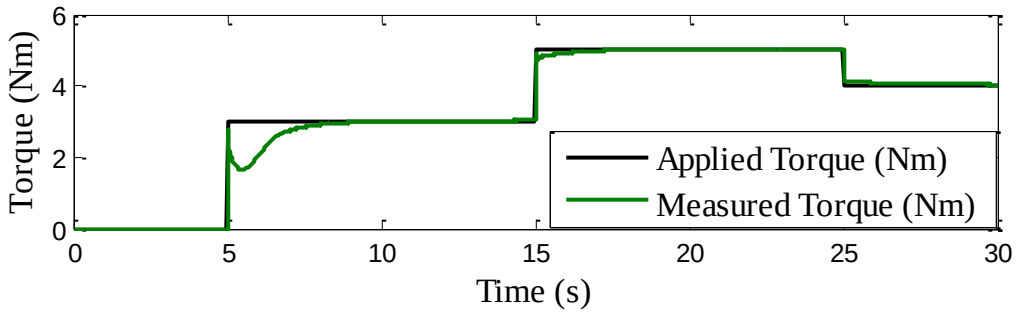


(a)

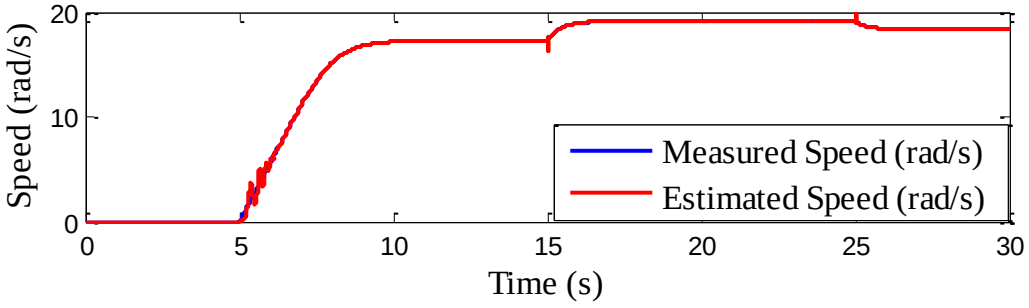


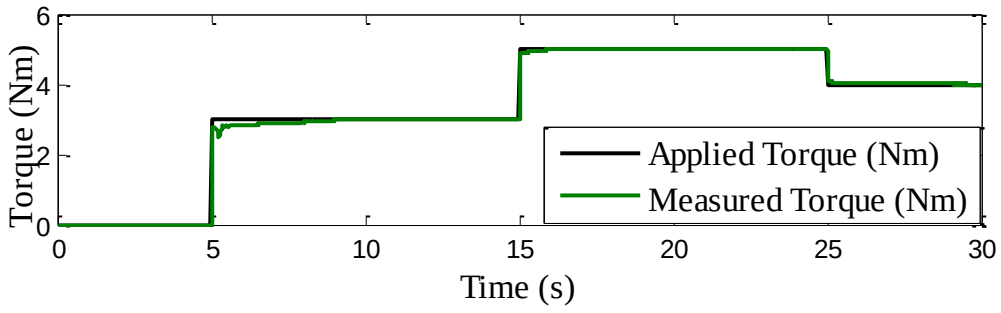


(b)

**Fig. 7.5. Simulation results for universal sensorless control using proposed scheme at different torque levels. (a) IM, and (b) SPMSM.**

### 7.4.2 Experimental results from dynamometer setup

The performance of the proposed scheme is compared against that of the conventional back-EMF MRAS scheme, using the 19-kW IM on a dynamometer setup. The scheme was also tested using the 10-kW SPMSM on dynamometer setup. The recorded behaviour of the proposed scheme implemented on both electric golf buggies is also presented. All of the experiments were conducted in sensorless mode. For these tests the measured (from encoder) and estimated (from sensorless scheme) speeds were recorded using the DVT software on a laptop. Regarding the injected voltage carrier, its amplitude was set to 2.5 V with frequency of 750 Hz. The injected voltage carrier was switched ON/OFF using a hysteresis band at 10 rad/s. The PI controller gains were initially tuned, whilst the speed from encoder was used for transformation between the reference frames. The gain values of all PI controllers used in this paper are provided in Table 7.1.

**Table 7.1. Gains of PI controllers.**

| **Description of PI Controllers** | **Type of scheme** | $k_p$ | $k_i$ |
|---|---|---|---|
| **Convectional back-EMF scheme** | MRAS | 0.8 | 0.08 |
| **Proposed scheme, IM on dynamometer** | Vs-MRAS adaptation mechanism | 0.5 | 0.05 |
| | Vs-MRAS identical compensators | 0.9 | 0.0001 |
| | HFSI | 0.3 | 0.2 |
| **Proposed scheme, SPMSM on dynamometer** | Vs-MRAS adaptation mechanism | 0.001 | 0.02 |
| | Vs-MRAS identical compensators | 0.9 | 0.0001 |
| | HFSI | 0.4 | 0.1 |
| **Proposed scheme, IM on golf buggy** | Vs-MRAS adaptation mechanism | 0.5 | 0.03 |
| | Vs-MRAS identical compensators | 0.9 | 0.0001 |
| | HFSI | 0.3 | 0.2 |
| **Proposed scheme, SPMSM on golf buggy** | Vs-MRAS adaptation mechanism | 0.005 | 0.05 |
| | Vs-MRAS identical compensators | 0.9 | 0.0001 |
| | HFSI | 0.4 | 0.1 |

#### *7.4.2.1 Starting from standstill using motor nominal parameters*

One of the critical requirements for a sensorless drive, employed for EV applications, is that it must be capable of performing sensorless starting from standstill in a correct direction to which it is requested by the driver of EV. Therefore, the following experiments were carried out, using the nominal motor parameters, to compare the conventional back-EMF [20] with the proposed hybrid scheme to demonstrate the capability of the proposed scheme for sensorless starting from standstill. Results for the conventional and proposed schemes are shown in Fig. 7.6-(a) and -(b), respectively. From the results for the conventional scheme it is clear that in the low speed region, the estimated speed does not follow the measured speed. It was also found that at zero speed the scheme becomes unstable and does not converge to zero. It can also be seen that when a -2 Nm applied torque demand was requested, for reverse direction, the IM accelerated in the opposite direction (forward direction) which is undesirable and unsafe to be used in EV applications. However, using the proposed scheme the estimated speed follows the measured speed and more importantly the IM accelerates in the correct direction, which matches the applied torque demand.

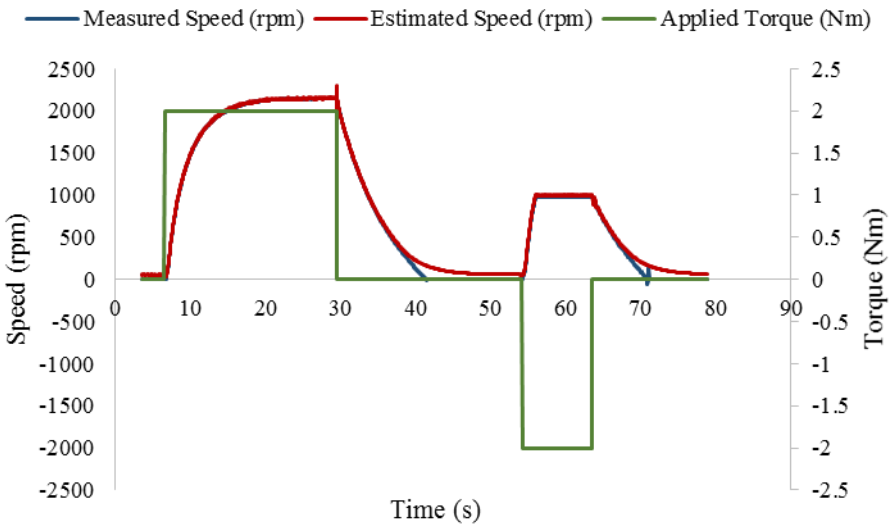


(a)

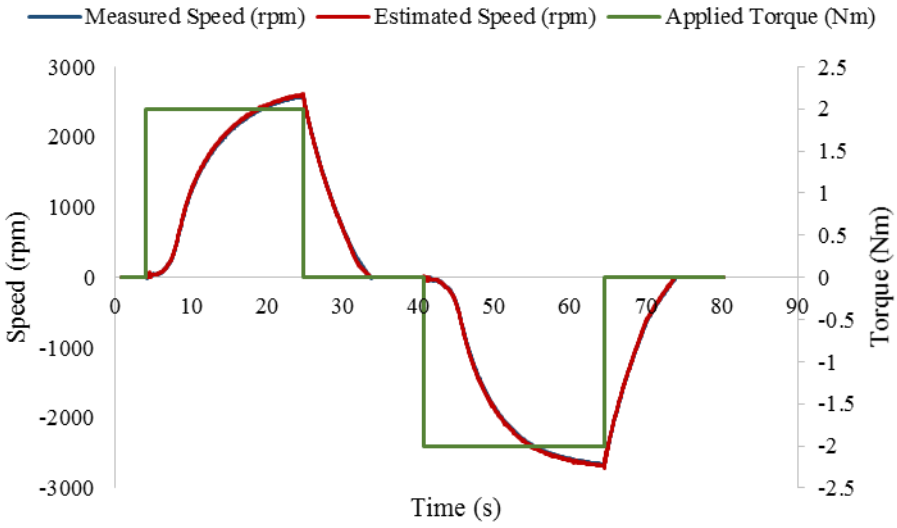


**(b)**

**Fig. 7.6. Experimental result of sensorless IM using nominal parameters at no load condition with ±2 Nm applied torque. (a) Conventional Back-EMF, and (b) proposed HVs-MRAS scheme.**

A test is also carried out to show the performance of the proposed scheme, when utilized on a SPMSM. The results are shown in Fig. 7.7-(a). This test includes three attempts in forward and reverse directions, respectively, for sensorless starting from standstill. It can be noted that not only does the estimated speed closely follow the measured speed but also the SPMSM has accelerated in the correct direction to that requested by the applied torque demand. Therefore, it can be stated that using the proposed scheme, provides a reliable and a stable sensorless drive, especially during starting from standstill. Note that the measured speed in the results for the SPMSM on the dynamometer setup are expected to be slightly noisy. This is due to the nature

of the Sine/Cos encoder. This test was also carried out for the IM and the results are shown in Fig. 7.7-(b).

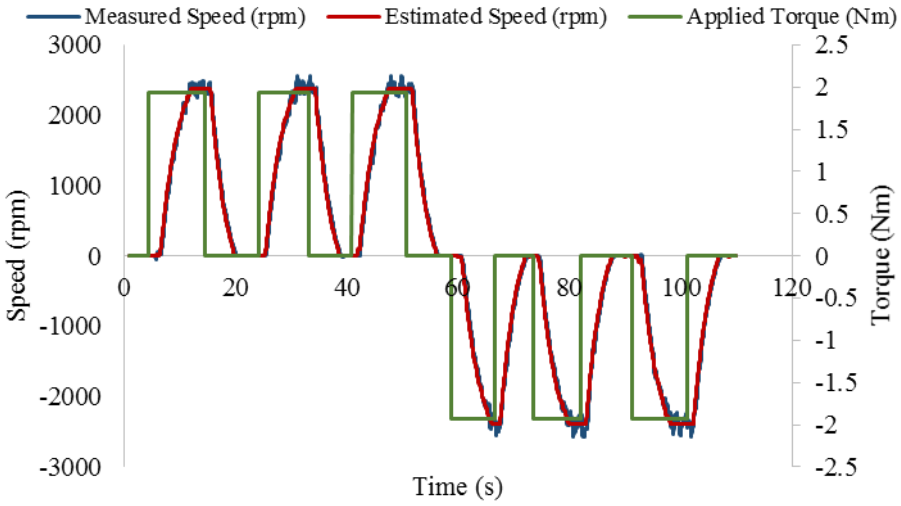


(a)

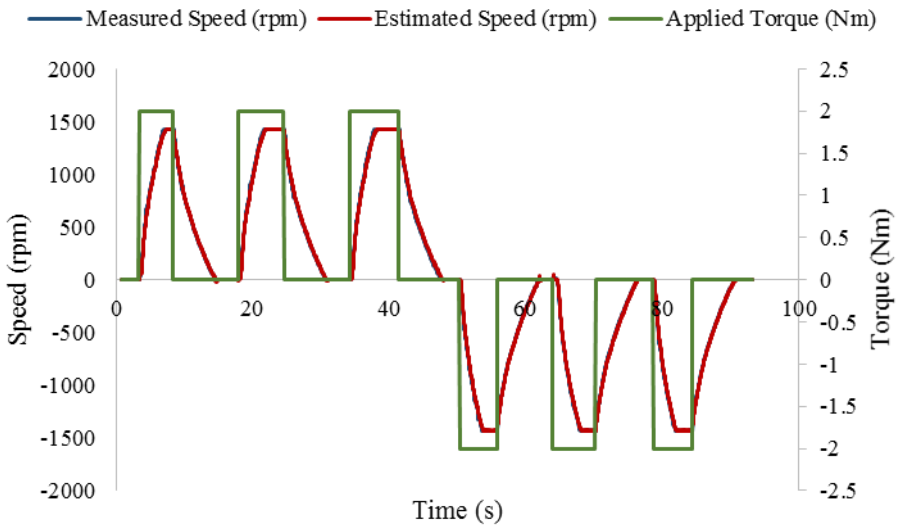


**(b)**

**Fig. 7.7. Experimental results using proposed sensorless HVs-MRAS at no load condition with three attempts in forward and reverse directions have been done, respectively. (a) SPMSM, and (b) IM.**

#### *7.4.2.2 Sensitivity to parameter variation test for 100% stator resistance variation*

It is important for a sensorless drive, which is employed for EV application to be robust against parameter variations. Hence, the following test was executed to demonstrate the behaviour of the proposed and conventional schemes for 100% variation in the stator resistance. During this test, for both schemes, an extra term ($R_s\bar{i}_{s\alpha\beta}$) was added to the input stator voltage components of the reference model. The proposed scheme benefits from the advantages of the HFSI at zero and low speed region and it is also equipped with two identical compensators in its reference model. Thus it is expected to be robust against motor parameter variation. The results of this test are shown in Fig. 7.8-(a), -(b), and -(c) for the conventional scheme on the IM, the proposed scheme and on the IM and SPMSM, respectively. From the result for the conventional scheme it can be seen that the estimated speed fails to follow the measured speed at zero and in the low speed region. Moreover, in comparison to the results taken when nominal parameters were used, the steady state error is considerably larger as shown in Fig. 7.7-(a). This scheme becomes unstable and causes the IM to accelerate in opposite direction when a -2 Nm torque command applied. However, from the results of the proposed scheme applied on the IM and SPMSM, it is clear that this scheme is robust to parameter variation and it continuous to perform reliably during starting from standstill.

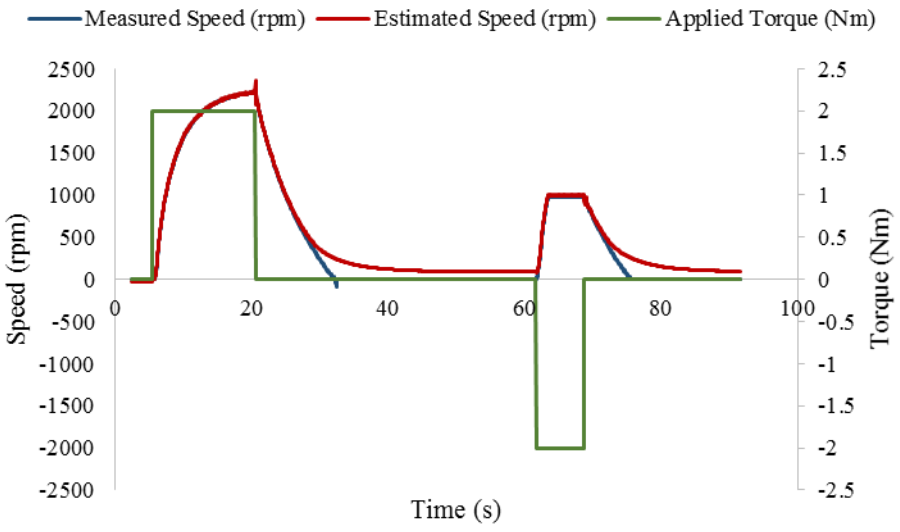


(a)

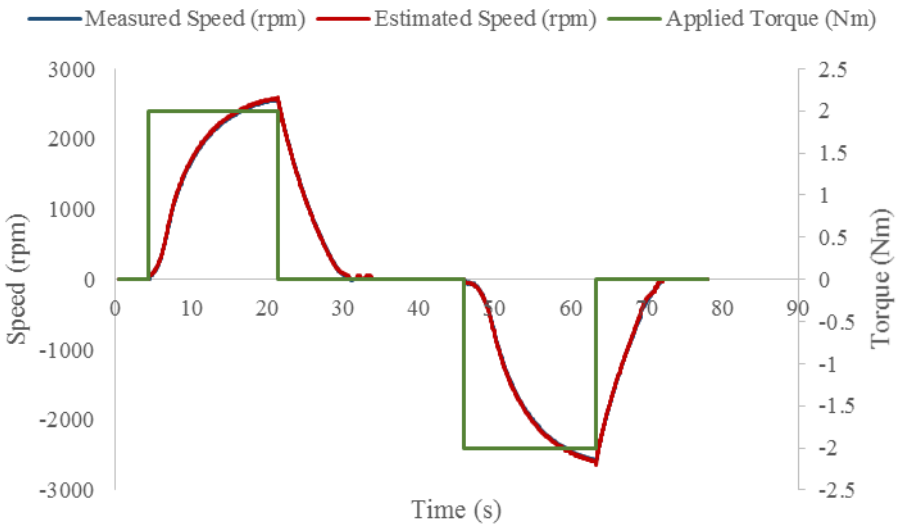


(b)

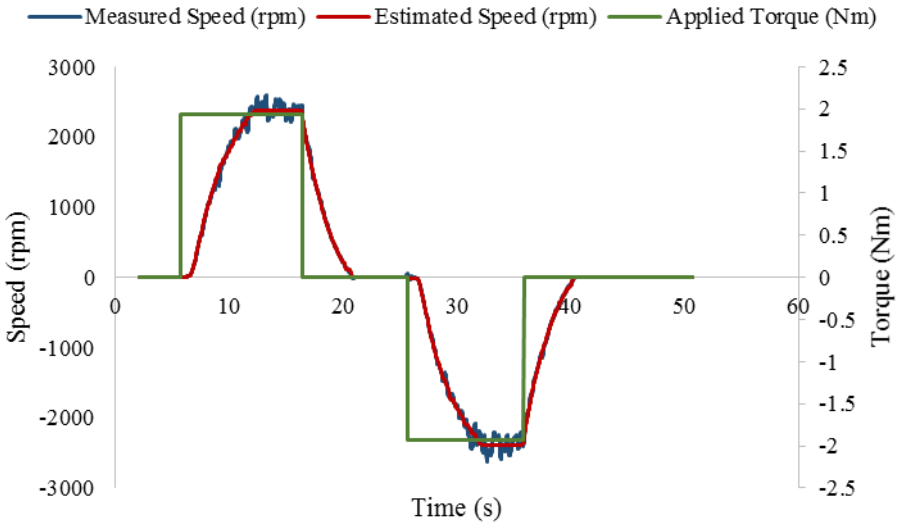


**(c)**

**Fig. 7.8. Sensorless experimental results for 100% stator resistance variation at no load condition. (a) Conventional back-EMF scheme on IM, (b) proposed HVs-MRAS scheme on IM, and (c) proposed HVs-MRAS scheme on SPMSM.**

### *7.4.2.3 Constant Speed operation at different torque levels*

This test was carried out to demonstrate the behaviour of the proposed scheme at constant speed with load torque variations. For this test, the shaft speed was kept constant at 500 rpm with the applied torque command varied in 5 Nm intervals from 10 Nm to 55 Nm. Results of this test are shown in Fig. 7.9-(a) and (b) for the IM and SPMSM, respectively. From the results taken for both motors it is clear that the estimated speed continuously tracks the measured speed closely. This is regardless of the variations in the torque command level.

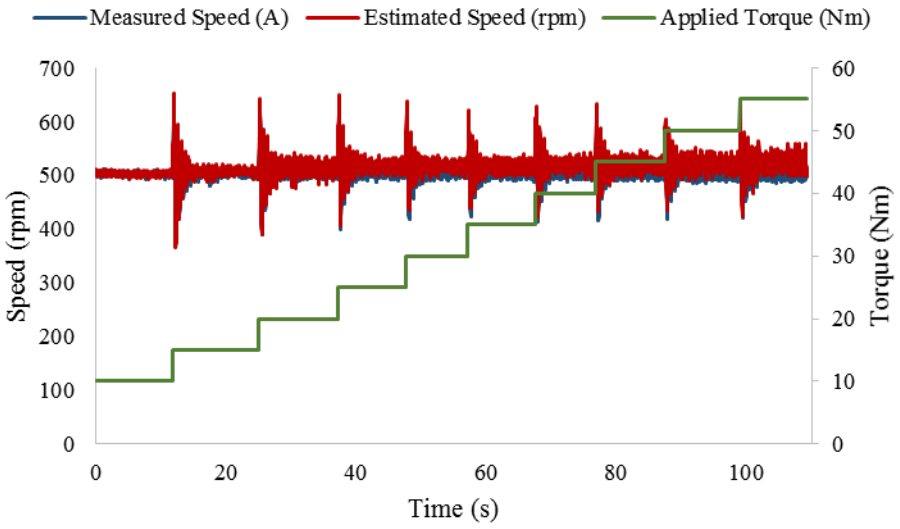


(a)

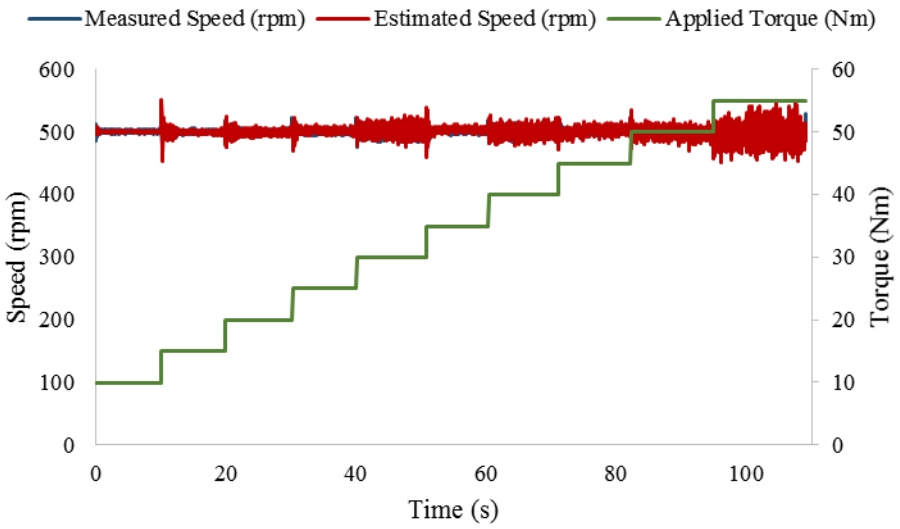


(b)

**Fig. 7.9. Sensorless experimental results using proposed HVs-MRAS at constant speed in the region of 500 rpm with torque command increased in 5 Nm intervals from 10 Nm to 55 Nm. (a) IM, and (b) SPMSM.**

### 7.4.3 Experimental results from golf buggies

The following tests were only carried out using the proposed scheme. This is to verify the capability of the proposed sensorless scheme, in the *limp-home* mode operation, regardless of being powered by either an IM or a SPMSM. During these tests the torque command applied using the vehicles' acceleration pedals. Also the torque direction (forward, park and reverse) was manually selected using the vehicles' gear sticks. All the results were recorded using a laptop with the measured speed from the encoder only used for verification purposes. Note that all the tests, using the vehicles, were carried out on an indoor test-track. This limits the maximum speed which can be achieved during high speed vehicle test-drive.

#### *7.4.3.1 Sensorless vehicle test-drive for several attempts starting from standstill*

In order to demonstrate reliability of the proposed scheme during vehicle sensorless operation starting from standstill, the following tests were carried out using electric golf buggies, powered by the IM and SPMSM. During these tests, vehicles were first driven forward and stopped for three consecutive times and then the same procedure was repeated in reverse direction. The results of these tests are shown in Fig. 7.10-(a) and -(b) for the golf buggy powered by the IM and SPMSM, respectively. It can be seen that using the proposed scheme, both vehicles perform reliably during several attempts starting from standstill. Moreover, the estimated speed follows the measured speed closely.

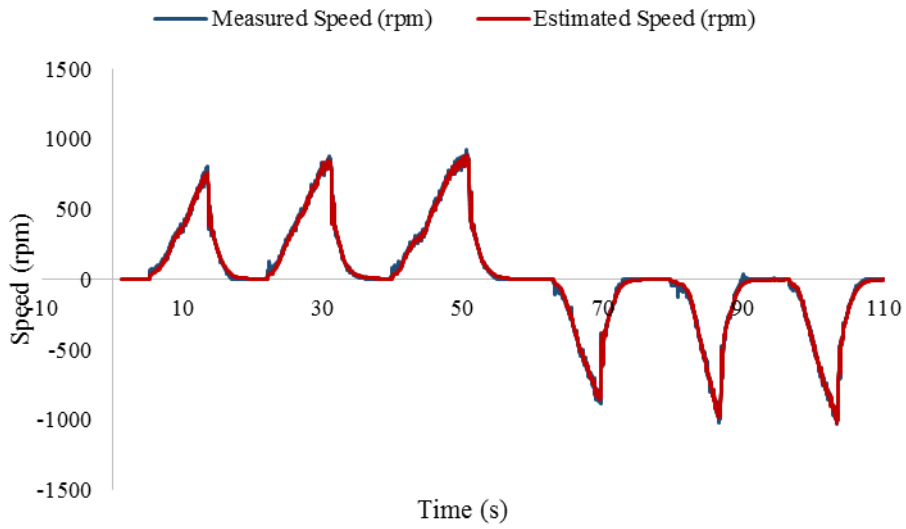


(a)

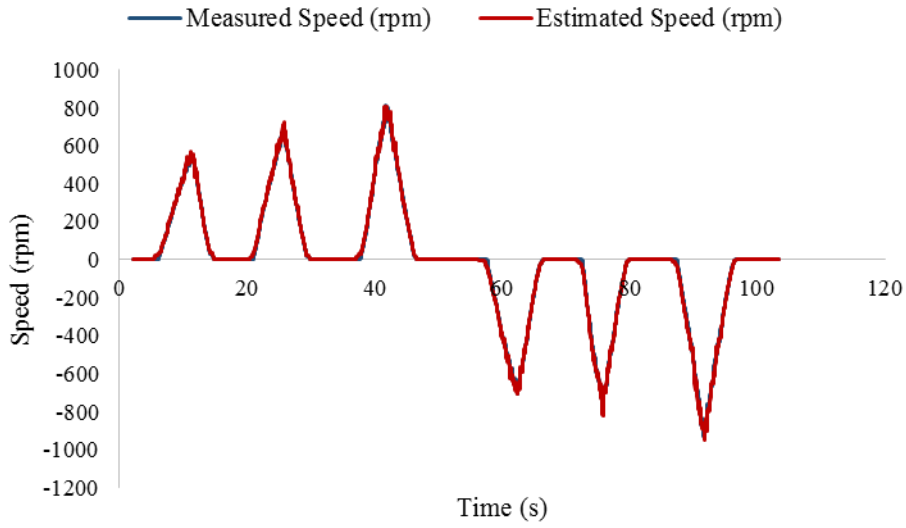


(b)

**Fig. 7.10. Sensorless vehicle test-drive using the proposed scheme for three consecutive attempts in forward and reverse direction, respectively. (a) Golf buggy powered by IM, and (b) golf buggy powered by SPMSM.**

### *7.4.3.2 Sensorless vehicle test-drive during a wide speed range*

It is essential that a sensorless scheme, which is employed for EV applications, be capable of performing stably in a wide speed range, especially in the field weakening region. Therefore these tests were carried out to demonstrate the behaviour of the proposed scheme in a wide speed range. For these tests, both vehicles were first accelerated forward from standstill to the field weakening region and then slowed back down to standstill. The same procedure is then repeated in the reverse direction. Results of these teste are shown in Fig. 7.11-(a) and -(b) for

the golf buggy powered by the IM and SPMSM, respectively. It is clear that the proposed scheme, regardless of motor type, is stable in a wide speed range, including the field weakening region. Moreover, using this scheme provides a smooth sensorless vehicle test-drive without any cogging-effect. Therefore it can be stated that the proposed scheme is suitable as a universal sensorless control for EV applications.

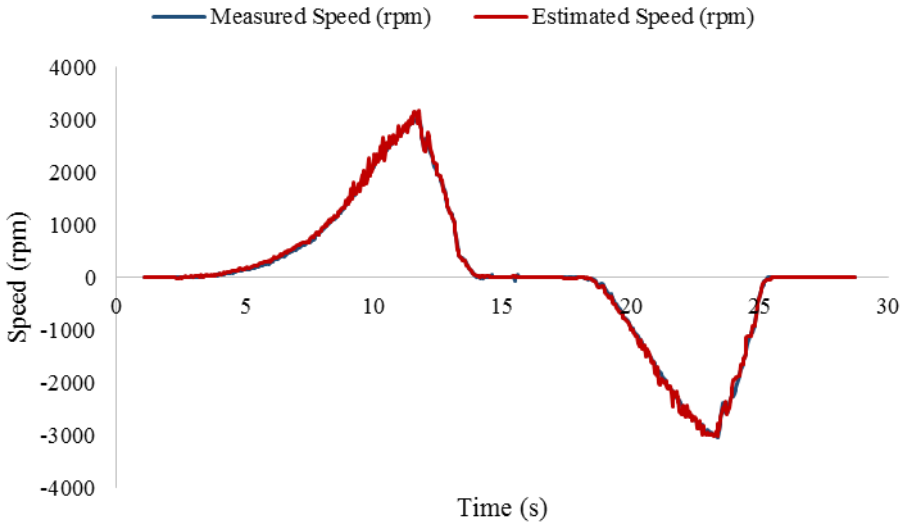


(a)

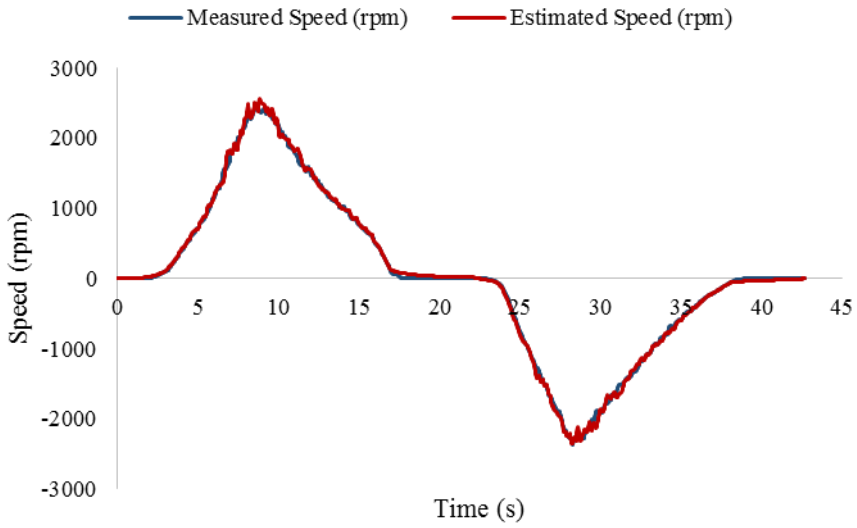


(b)

**Fig. 7.11. Sensorless vehicle test-drive using the proposed scheme in a wide speed range in forward and reverse direction, respectively. (a) Golf buggy powered by IM, and (b) golf buggy powered by SPMSM.**

## 7.5 Conclusion

The proposed universal sensorless HVs-MRAS scheme for IM and SPMSM has been successfully implemented and tested in a laboratory environment and with two electric golf buggies. The proposed scheme inherits the advantages of the HFSI at zero and low speed, hence, it is robust against motor parameter variations. The combining function provides a seamless transition between the HFSI and the Vs-MRAS schemes. Experimental results from the test setup and golf buggies confirm that using this scheme provides a safe and consistent vehicle-starting from standstill. More importantly, experimental results from golf buggies also verify the robustness and reliability of this scheme for EV application over a wide range of speeds, including the field weakening region. Hence, this scheme is suitable for *limp-home* of EV applications.

However, utilising this scheme in the hill-holding operation requires further improvement and the performance of the Vs-MRAS in chapter 6 for the IM is similar to that obtained from the hybrid scheme with one less PI controller to tune.

# CHAPTER 8. CONCLUSIONS AND FUTURE WORKS

## 8.1 Introduction

During the course of this research, several sensorless schemes based on MRAS were successfully developed for use in *limp-home* mode of EV applications. The behaviour of the developed schemes were experimentally investigated using test bench setup and electric vehicles. During tests particular attention was given to the critical sensorless vehicle starting from standstill and smooth vehicle test-drive in a wide range of speed, including the field weakening region. The aim of this chapter is to provide an overall conclusion of the findings in this research and recommendation for future studies.

## 8.2 Discussion and conclusion

As discussed in chapter 1, the efficiency and safety of EV applications are directly dependent on the accuracy and health of the motor controller. Speed/position sensor failure can paralyse the motor controller and as a result bring the EV to halt mode. Consequently, this can

result in a life-threatening event if it takes place on a highway or busy roundabout. Therefore, to improve the safety, reliability and availability of EV applications, a robust sensorless scheme is required for operation in the *limp-home* mode.

After a comprehensive literature review, which was carried out in chapter 2, the back-EMF MRAS scheme, originally developed by Peng and Fukao [20], was concluded to be the most suitable candidate among MRAS schemes. However, in order to employ this scheme in *limp-home* mode of EV applications, the scheme require some modifications to improve its performance. The main shortcomings of the conventional back-EMF MRAS scheme were found to be associated with the errors due to the sensitivity to the motor parameter variation, in zero and low speed regions, and digitisation in high speed regions. It was also found that the use of universal schemes promote the reduction in computational complexity of the overall sensorless drive when employed on AC motors.

The description of the mathematical modelling of the IM and SPMSM was provided in chapter 3. The principles of the IRFOC for the IM and SPMSM was also presented. Moreover, the principles of the conventional back-EMF MRAS and sensorless control using HFSI technique used in this project, originally developed by Linke [94], were presented. In chapter 4 the test bench setup and the electric golf buggies which have been used in this project were presented. Moreover, a full description of the components of the experimental test setup was listed and the dragon8 controller used in this thesis was described. The golf buggies description and their block diagram were also provided.

A new scheme was proposed in chapter 5 to deal with the shortcomings of the conventional back-EMF MRAS. The reference model of this scheme employs a novel compensating mechanism, to compensate for errors due to parameter variations, inverter non-linearity and digitisation in high speed regions. A new approach was used in the adjustable model of this scheme which is free from integration problems. This results in an effective sensorless control when starting from standstill and during high speed operation. The proposed scheme was successfully implemented and tested on two different IMs using the test bench setup and the IM golf buggy, respectively. This scheme is not computationally demanding and showed to be robust against stator resistance variations of 50% and 100% increase. The proposed scheme was found to be consistent and stable for the vehicle-starting from standstill and low speeds. It also performed reliably above base speed in the field weakening region. During the tests, the proposed scheme was shown satisfactory operation throughout forward and backword modes of operation in addition to the constant speed variable load operation. More importantly the scheme had demonstrated satisfactory performance for vehicle hill-starting. Therefore the proposed back-EMF MRAS scheme was shown to be suitable for the

*limp-home* mode operation of EV applications by providing consistent, safe and reliable operation over the whole speed range. However, to implement this scheme all the IM nominal parameters are required. Therefore, a sensorless scheme which is less dependent on the prerequisite knowledge of the IM nominal parameters was developed.

In chapter 6 a novel Vs-MRAS for sensorless TCD of IM for the purpose of *limp-home* mode of EV applications was presented. The Vs-MRAS scheme uses the error between the reference and estimated stator voltage vectors and estimates the synchronous speed. Unlike existing MRAS schemes, the proposed sensorless scheme does not require the measured nominal values of stator resistance, stator inductance, and rotor resistance. Moreover, using the proposed scheme eliminates the need for slip calculation. The scheme was successfully implemented in the lab environment and on the IM golf buggy. Results of the proposed scheme confirmed that this scheme is robust against parameter variations and is stable in the low speed regions. Results recorded while the proposed scheme was applied on the golf buggy confirm that a safe and consistent vehicle-starting and hill-starting from standstill can be achieved, with correct direction to that requested. More importantly, it was found that the scheme provides a smooth and stable drive in a wide speed range, including the field weakening region. Therefore the proposed Vs-MRAS was proven to be a suitable scheme to be employed for *limp-home* mode operation in the EV/HEV applications by providing a reliable and smooth drive in a wide speed range. However, to employ this scheme for sensorless control of SPMSM, it is required to be hybridised using a HFSI scheme at zero and low speed regions.

In chapter 7 a proposed universal sensorless HVs-MRAS scheme for IM and SPMSM was presented. Unlike the other combined sensorless approaches, the proposed scheme can be employed for an IM or a SPMSM. The scheme was successfully implemented and tested in the laboratory environment and with two electric golf buggies. The proposed scheme inherits the advantages of the HFSI at zero and low speed, hence, it was found to be robust against motor parameter variations. The combining function provides a seamless transition between the HFSI and the Vs-MRAS schemes. Experimental results from the test setup and golf buggies confirmed that using this scheme provides a safe and consistent vehicle-starting from standstill. More importantly, experimental results from golf buggies also verified the robustness and reliability of this scheme for EV application over a wide range of speeds, including the field weakening region. Hence, this scheme had shown to be suitable for *limp-home* of EV applications.

## 8.3 Future works

- Further research is required to improve the sensorless vehicle hill-hold operation for IM as the vehicle experiences roll-back during sensorless operation, which is not safe.
- This research has investigated sensorless schemes suitable for *limp-home* mode in EV application. However, further research is required to explore different possibilities of speed/position sensor failures and schemes to detect these failures.
- In order to have a smooth transition between both *sensored* and sensorless drives, further research is also required to design a smooth and reliable switching mechanism.
- In this research a universal sensorless drive is applied for IM and SPMSM. This scheme is a compelling approach for multiple industry applications, hence, further study is required to extend the compatibility range of this scheme to other types of motors.
- Additional work is also required to investigate the capability of the proposed compensating mechanism, in chapter 5, against the effects of inverter non-linearity.

# REFERENCES


[1] K. T. Chau, "Introduction," in *Electric Vehicle Machines and Drives: Design, Analysis and Application*, ed: Wiley-IEEE Press, 2015, p. 375.

[2] C. C. Chan, "The state of the art of electric and hybrid vehicles," *Proceedings of the IEEE*, vol. 90, pp. 247-275, 2002.

[3] M. E. H. Benbouzid, D. Diallo, and M. Zeraoulia, "Advanced Fault-Tolerant Control of Induction-Motor Drives for EV/HEV Traction Applications: From Conventional to Modern and Intelligent Control Techniques," *Vehicular Technology, IEEE Transactions on*, vol. 56, pp. 519-528, 2007.

[4] D. O. Neacsu and K. Rajashekara, "Comparative analysis of torque-controlled IM drives with applications in electric and hybrid vehicles," *Power Electronics, IEEE Transactions on*, vol. 16, pp. 240-247, 2001.

[5] E. Dehghan-Azad, S. Gadoue, D. Atkinson, H. Slater, P. Barrass, and F. Blaabjerg, "Sensorless Control of IM for Limp-Home Mode EV Applications," *IEEE Transactions on Power Electronics*, vol. 32, pp. 7140-7150, 2017.

[6] E. Dehghan-Azad, S. Gadoue, D. Atkinson, H. Slater, P. Barrass, and F. Blaabjerg, "Sensorless control of IM based on stator-voltage MRAS for Limp-home EV applications," *IEEE Transactions on Power Electronics*, vol. PP, pp. 1-1, 2017.

[7] E. Dehghan-Azad, S. Gadoue, D. Atkinson, H. Slater, and P. Barrass, "Sensorless torque-controlled Induction Motor drive for EV applications," in *2017 IEEE Transportation Electrification Conference and Expo (ITEC)*, 2017, pp. 263-268.

[8] J. Holtz, "Sensorless control of induction motor drives," *Proceedings of the IEEE*, vol. 90, pp. 1359-1394, 2002.

[9] P. Vas, *Sensorless Vector and Direct Torque Control*. New York: Oxford University Press, 1998.

[10] M. Aydin, M. Gokasan, and S. Bogosyan, "Fuzzy based parameter tuning of EKF observers for sensorless control of Induction Motors," in *2014 International Symposium on Power Electronics, Electrical Drives, Automation and Motion*, 2014, pp. 1174-1179.

[11] S. Bolognani, R. Oboe, and M. Zigliotto, "Sensorless full-digital PMSM drive with EKF estimation of speed and rotor position," *IEEE Transactions on Industrial Electronics*, vol. 46, pp. 184-191, 1999.

[12] N. K. Quang, N. T. Hieu, and Q. P. Ha, "FPGA-Based Sensorless PMSM Speed Control Using Reduced-Order Extended Kalman Filters," *IEEE Transactions on Industrial Electronics*, vol. 61, pp. 6574-6582, 2014.

[13] F. Mwasilu and J. W. Jung, "Enhanced Fault-Tolerant Control of Interior PMSMs Based on an Adaptive EKF for EV Traction Applications," *IEEE Transactions on Power Electronics*, vol. 31, pp. 5746-5758, 2016.

[14] Z. Yin, G. Li, Y. Zhang, J. Liu, X. Sun, and Y. Zhong, "A Speed and Flux Observer of Induction Motor Based On Extended Kalman Filter and Markov Chain," *IEEE Transactions on Power Electronics*, vol. PP, pp. 1-1, 2016.

[15] J. Lee, J. Hong, K. Nam, R. Ortega, L. Praly, and A. Astolfi, "Sensorless Control of Surface-Mount Permanent-Magnet Synchronous Motors Based on a Nonlinear Observer," *IEEE Transactions on Power Electronics*, vol. 25, pp. 290-297, 2010.

[16] H. Kim, J. Son, and J. Lee, "A High-Speed Sliding-Mode Observer for the Sensorless Speed Control of a PMSM," *IEEE Transactions on Industrial Electronics*, vol. 58, pp. 4069-4077, 2011.

[17] X. Zhang, "Sensorless Induction Motor Drive Using Indirect Vector Controller and Sliding-Mode Observer for Electric Vehicles," *IEEE Transactions on Vehicular Technology*, vol. 62, pp. 3010-3018, 2013.

[18] K. Ohyama, G. M. Asher, and M. Sumner, "Comparative analysis of experimental performance and stability of sensorless induction motor drives," *IEEE Transactions on Industrial Electronics*, vol. 53, pp. 178-186, 2005.

[19] C. Schauder, "Adaptive speed identification for vector control of induction motors without rotational transducers," *Industry Applications, IEEE Transactions on*, vol. 28, pp. 1054-1061, 1992.

[20] F. Z. Peng and T. Fukao, "Robust speed identification for speed-sensorless vector control of induction motors," *Industry Applications, IEEE Transactions on*, vol. 30, pp. 1234-1240, 1994.

[21] M. N. Marwali and A. Keyhani, "A comparative study of rotor flux based MRAS and back EMF based MRAS speed estimators for speed sensorless vector control of induction machines," in *Industry Applications Conference, 1997. Thirty-Second IAS Annual Meeting, IAS '97., Conference Record of the 1997 IEEE*, 1997, pp. 160-166 vol.1.

[22] J. W. Finch and D. Giaouris, "Controlled AC Electrical Drives," *Industrial Electronics, IEEE Transactions on*, vol. 55, pp. 481-491, 2008.

[23] I. Benlaloui, S. Drid, L. Chrifi-Alaoui, and M. Ouriagli, "Implementation of a New MRAS Speed Sensorless Vector Control of Induction Machine," *IEEE Transactions on Energy Conversion*, vol. 30, pp. 588-595, 2015.

[24] A. N. Smith, S. M. Gadoue, and J. W. Finch, "Improved Rotor Flux Estimation at Low Speeds for Torque MRAS-Based Sensorless Induction Motor Drives," *IEEE Transactions on Energy Conversion*, vol. 31, pp. 270-282, 2016.

[25] S. M. Gadoue, D. Giaouris, and J. W. Finch, "MRAS Sensorless Vector Control of an Induction Motor Using New Sliding-Mode and Fuzzy-Logic Adaptation Mechanisms," *Energy Conversion, IEEE Transactions on*, vol. 25, pp. 394-402, 2010.

[26] M. Comanescu and L. Xu, "Sliding-mode MRAS speed estimators for sensorless vector control of induction Machine," *IEEE Transactions on Industrial Electronics*, vol. 53, pp. 146-153, 2005.

[27] F. Wang, S. A. Davari, Z. Chen, Z. Zhang, D. A. Khaburi, J. Rodriguez, *et al.*, "Finite Control Set Model Predictive Torque Control of Induction Machine with a Robust Adaptive Observer," *IEEE Transactions on Industrial Electronics,* vol. PP, pp. 1-1, 2016.

[28] A. V. Ravi Teja, V. Verma, and C. Chakraborty, "A New Formulation of Reactive-Power-Based Model Reference Adaptive System for Sensorless Induction Motor Drive," *Industrial Electronics, IEEE Transactions on,* vol. 62, pp. 6797-6808, 2015.

[29] S. Maiti, C. Chakraborty, Y. Hori, and M. C. Ta, "Model Reference Adaptive Controller-Based Rotor Resistance and Speed Estimation Techniques for Vector Controlled Induction Motor Drive Utilizing Reactive Power," *IEEE Transactions on Industrial Electronics,* vol. 55, pp. 594-601, 2008.

[30] A. V. R. Teja, C. Chakraborty, S. Maiti, and Y. Hori, "A New Model Reference Adaptive Controller for Four Quadrant Vector Controlled Induction Motor Drives," *IEEE Transactions on Industrial Electronics,* vol. 59, pp. 3757-3767, 2012.

[31] S. Maiti, V. Verma, C. Chakraborty, and Y. Hori, "An Adaptive Speed Sensorless Induction Motor Drive With Artificial Neural Network for Stability Enhancement," *IEEE Transactions on Industrial Informatics,* vol. 8, pp. 757-766, 2012.

[32] S. M. Gadoue, D. Giaouris, and J. W. Finch, "Sensorless Control of Induction Motor Drives at Very Low and Zero Speeds Using Neural Network Flux Observers," *Industrial Electronics, IEEE Transactions on,* vol. 56, pp. 3029-3039, 2009.

[33] L. Zhen and L. Xu, "Sensorless field orientation control of induction machines based on a mutual MRAS scheme," *IEEE Transactions on Industrial Electronics,* vol. 45, pp. 824-831, 1998.

[34] T. Orlowska-Kowalska and M. Dybkowski, "Stator-Current-Based MRAS Estimator for a Wide Range Speed-Sensorless Induction-Motor Drive," *IEEE Transactions on Industrial Electronics,* vol. 57, pp. 1296-1308, 2010.

[35] L. Yan and L. Yongdong, "Sensorless control of PM synchronous motors based on MRAS method and initial position estimation," in *Sixth International Conference on Electrical Machines and Systems, 2003. ICEMS 2003.*, 2003, pp. 96-99 vol.1.

[36] A. Khlaief, M. Boussak, and A. Châari, "A MRAS-based stator resistance and speed estimation for sensorless vector controlled IPMSM drive," *Electric Power Systems Research,* vol. 108, pp. 1-15, 3// 2014.

[37] Y. Zhao, W. Qiao, and L. Wu, "Improved Rotor Position and Speed Estimators for Sensorless Control of Interior Permanent-Magnet Synchronous Machines," *IEEE Journal of Emerging and Selected Topics in Power Electronics,* vol. 2, pp. 627-639, 2014.

[38] M. Rashed, P. F. A. MacConnell, A. F. Stronach, and P. Acarnley, "Sensorless Indirect-Rotor-Field-Orientation Speed Control of a Permanent-Magnet Synchronous Motor With Stator-Resistance Estimation," *IEEE Transactions on Industrial Electronics,* vol. 54, pp. 1664-1675, 2007.

[39] J. Holtz and Q. Juntao, "Drift- and parameter-compensated flux estimator for persistent zero-stator-frequency operation of sensorless-controlled induction motors," *Industry Applications, IEEE Transactions on,* vol. 39, pp. 1052-1060, 2003.

[40] B. Karanayil, M. F. Rahman, and C. Grantham, "An implementation of a programmable cascaded low-pass filter for a rotor flux synthesizer for an induction motor drive," *IEEE Transactions on Power Electronics,* vol. 19, pp. 257-263, 2004.

[41] A. R. Haron and N. R. N. Idris, "Simulation of MRAS-based Speed Sensorless Estimation of Induction Motor Drives using MATLAB/SIMULINK," in *2006 IEEE International Power and Energy Conference*, 2006, pp. 411-415.

[42] M. Rashed and A. F. Stronach, "A stable back-EMF MRAS-based sensorless low-speed induction motor drive insensitive to stator resistance variation," *Electric Power Applications, IEE Proceedings* -, vol. 151, pp. 685-693, 2004.

[43] G. Shen, W. Yao, B. Chen, K. Wang, K. Lee, and Z. Lu, "Automeasurement of the Inverter Output Voltage Delay Curve to Compensate for Inverter Nonlinearity in Sensorless Motor Drives," *IEEE Transactions on Power Electronics,* vol. 29, pp. 5542-5553, 2014.

[44] J. Holtz and Q. Juntao, "Sensorless vector control of induction motors at very low speed using a nonlinear inverter model and parameter identification," *IEEE Transactions on Industry Applications,* vol. 38, pp. 1087-1095, 2002.

[45] B. Wang, Y. Zhao, Y. Yu, G. Wang, D. Xu, and Z. Dong, "Speed-Sensorless Induction Machine Control in the Field-Weakening Region Using Discrete Speed-Adaptive Full-Order Observer," *IEEE Transactions on Power Electronics,* vol. 31, pp. 5759-5773, 2016.

[46] D. P. Mar, x010D, eti, x, I. R. Kr, x010D, *et al.*, "Discrete Rotor Flux and Speed Estimators for High-Speed Shaft-Sensorless IM Drives," *IEEE Transactions on Industrial Electronics,* vol. 61, pp. 3099-3108, 2014.

[47] M. Martinez-Iturralde, G. Martinez, J. Atencia, A. G. Rico, and J. Florez, "Analysis of voltage measurement techniques for direct torque control of induction motors," in *Electric Machines and Drives Conference, 2003. IEMDC'03. IEEE International*, 2003, pp. 1151-1155 vol.2.

[48] H. Jung-Ik and S. Seung-Ki, "Sensorless field-orientation control of an induction machine by high-frequency signal injection," *IEEE Transactions on Industry Applications,* vol. 35, pp. 45-51, 1999.

[49] J. Ji-Hoon, S. Seung-Ki, H. Jung-Ik, K. Ide, and M. Sawamura, "Sensorless drive of surface-mounted permanent-magnet motor by high-frequency signal injection based on magnetic saliency," *IEEE Transactions on Industry Applications,* vol. 39, pp. 1031-1039, 2003.

[50] P. L. Xu and Z. Q. Zhu, "Novel Carrier Signal Injection Method Using Zero-Sequence Voltage for Sensorless Control of PMSM Drives," *IEEE Transactions on Industrial Electronics,* vol. 63, pp. 2053-2061, 2016.

[51] Y. D. Yoon, S. K. Sul, S. Morimoto, and K. Ide, "High-Bandwidth Sensorless Algorithm for AC Machines Based on Square-Wave-Type Voltage Injection," *IEEE Transactions on Industry Applications,* vol. 47, pp. 1361-1370, 2011.

[52] C. Caruana, G. M. Asher, K. J. Bradley, and M. Woolfson, "Flux position estimation in cage induction machines using synchronous HF injection and Kalman filtering," *IEEE Transactions on Industry Applications,* vol. 39, pp. 1372-1378, 2003.

[53] P. L. Jansen and R. D. Lorenz, "Transducerless position and velocity estimation in induction and salient AC machines," *IEEE Transactions on Industry Applications,* vol. 31, pp. 240-247, 1995.

[54] J. Holtz, "Sensorless Control of Induction Machines—With or Without Signal Injection?," *IEEE Transactions on Industrial Electronics,* vol. 53, pp. 7-30, 2005.

[55] F. Briz, M. W. Degner, P. Garcia, and J. M. Guerrero, "Rotor position estimation of AC machines using the zero-sequence carrier-signal voltage," *IEEE Transactions on Industry Applications,* vol. 41, pp. 1637-1646, 2005.

[56] S. C. Yang and Y. L. Hsu, "Full Speed Region Sensorless Drive of Permanent Magnet Machine Combining Saliency-Based and Back-EMF-Based Drive," *IEEE Transactions on Industrial Electronics,* vol. PP, pp. 1-1, 2016.

[57] M. Schroedl, "Sensorless control of AC machines at low speed and standstill based on the “INFORM” method," in *Industry Applications Conference, 1996. Thirty-First IAS Annual Meeting, IAS '96., Conference Record of the 1996 IEEE*, 1996, pp. 270-277 vol.1.

[58] C. Silva, G. M. Asher, and M. Sumner, "Hybrid rotor position observer for wide speed-range sensorless PM motor drives including zero speed," *IEEE Transactions on Industrial Electronics,* vol. 53, pp. 373-378, 2006.

[59] K. Hyunbae, H. Kum-Kang, R. D. Lorenz, and T. M. Jahns, "A novel method for initial rotor position estimation for IPM synchronous machine drives," *IEEE Transactions on Industry Applications,* vol. 40, pp. 1369-1378, 2004.

[60] J. Holtz, "Acquisition of Position Error and Magnet Polarity for Sensorless Control of PM Synchronous Machines," *IEEE Transactions on Industry Applications,* vol. 44, pp. 1172-1180, 2008.

[61] J. Yu-seok, R. D. Lorenz, T. M. Jahns, and S. Seung-Ki, "Initial rotor position estimation of an interior permanent-magnet synchronous machine using carrier-frequency injection methods," *IEEE Transactions on Industry Applications,* vol. 41, pp. 38-45, 2005.

[62] G. D. Andreescu, C. I. Pitic, F. Blaabjerg, and I. Boldea, "Combined Flux Observer With Signal Injection Enhancement for Wide Speed Range Sensorless Direct Torque Control of IPMSM Drives," *IEEE Transactions on Energy Conversion,* vol. 23, pp. 393-402, 2008.

[63] G. Foo and M. F. Rahman, "Sensorless Sliding-Mode MTPA Control of an IPM Synchronous Motor Drive Using a Sliding-Mode Observer and HF Signal Injection," *IEEE Transactions on Industrial Electronics,* vol. 57, pp. 1270-1278, 2010.

[64] Y. Sun, M. Preindl, S. Sirouspour, and A. Emadi, "Unified Wide-Speed Sensorless Scheme Using Nonlinear Optimization for IPMSM Drives," *IEEE Transactions on Power Electronics,* vol. PP, pp. 1-1, 2016.

[65] Z. Ma, J. Gao, and R. Kennel, "FPGA Implementation of a Hybrid Sensorless Control of SMPMSM in the Whole Speed Range," *IEEE Transactions on Industrial Informatics,* vol. 9, pp. 1253-1261, 2013.

[66] S. Morimoto, K. Kawamoto, M. Sanada, and Y. Takeda, "Sensorless control strategy for salient-pole PMSM based on extended EMF in rotating reference frame," *IEEE Transactions on Industry Applications,* vol. 38, pp. 1054-1061, 2002.

[67] M. J. Corley and R. D. Lorenz, "Rotor position and velocity estimation for a salient-pole permanent magnet synchronous machine at standstill and high speeds," *IEEE Transactions on Industry Applications,* vol. 34, pp. 784-789, 1998.

[68] S. Yamamoto, H. Hirahara, A. Tanaka, T. Ara, and K. Matsuse, "Universal Sensorless Vector Control of Induction and Permanent-Magnet Synchronous Motors Considering Equivalent Iron Loss Resistance," *IEEE Transactions on Industry Applications,* vol. 51, pp. 1259-1267, 2015.

[69] L. Harnefors, M. Jansson, R. Ottersten, and K. Pietilainen, "Unified sensorless vector control of synchronous and induction motors," *IEEE Transactions on Industrial Electronics,* vol. 50, pp. 153-160, 2003.

[70] I. Boldea, M. C. Paicu, and G. D. Andreescu, "Active Flux Concept for Motion-Sensorless Unified AC Drives," *IEEE Transactions on Power Electronics,* vol. 23, pp. 2612-2618, 2008.

[71] C. Zhiqian, M. Tomita, S. Ichikawa, S. Doki, and S. Okuma, "Sensorless control of interior permanent magnet synchronous motor by estimation of an extended electromotive force," in *Conference Record of the 2000 IEEE Industry Applications Conference. Thirty-Fifth IAS Annual Meeting and World Conference on Industrial Applications of Electrical Energy (Cat. No.00CH37129)*, 2000, pp. 1814-1819 vol.3.

[72] S. Morimoto, M. Sanada, and Y. Takeda, "Mechanical Sensorless Drives of IPMSM With Online Parameter Identification," *IEEE Transactions on Industry Applications,* vol. 42, pp. 1241-1248, 2006.

[73] S. Koonlaboon and S. Sangwongwanich, "Sensorless control of interior permanent-magnet synchronous motors based on a fictitious permanent-magnet flux model," in *Fourtieth IAS Annual Meeting. Conference Record of the 2005 Industry Applications Conference, 2005.*, 2005, pp. 311-318 Vol. 1.

[74] J. Faiz, M. B. B. Sharifian, A. Keyhani, and A. B. Proca, "Sensorless direct torque control of induction motors used in electric vehicle," *IEEE Transactions on Energy Conversion,* vol. 18, pp. 1-10, 2003.

[75] M. Dybkowski and T. Orlowska-Kowalska, "Performance of the speed sensorless Induction Motor drive for traction application with MRAS type speed and flux estimator," in *2012 13th International Conference on Optimization of Electrical and Electronic Equipment (OPTIM)*, 2012, pp. 477-481.

[76] B. Singh, P. Jain, A. P. Mittal, and J. R. P. Gupta, "Speed sensorless electric vehicle propulsion system using DTC IM drive," in *2006 India International Conference on Power Electronics*, 2006, pp. 7-11.

[77] C. Conilh and M. Pietrzak-David, "Sensorless Traction System with Low Voltage High Current Induction Machine for Indoor Vehicle," in *2005 International Conference on Power Electronics and Drives Systems*, 2005, pp. 50-55.

[78] M. Farasat and E. Karaman, "Speed sensorless electric vehicle propulsion system using hybrid FOC-DTC induction motor drive," in *2011 International Conference on Electrical Machines and Systems*, 2011, pp. 1-5.

[79] M. Farasat, E. Karaman, A. M. Trzynadlowski, and M. S. Fadali, "Hybrid field orientation and direct torque control for electric vehicle motor drive with an extended Kalman filter," in *2012 IEEE Energytech*, 2012, pp. 1-6.

[80] S. Rind, Y. Ren, and L. Jiang, "MRAS based speed sensorless indirect vector control of induction motor drive for electric vehicles," in *2014 49th International Universities Power Engineering Conference (UPEC)*, 2014, pp. 1-6.

[81] J. Zhang, X. Wen, and Y. Hua, "A novel speed-sensorless vector control technique of induction motor for Electrical vehicle propulsion," in *2008 IEEE Vehicle Power and Propulsion Conference*, 2008, pp. 1-5.

[82] N. Patel, T. O'Meara, J. Nagashima, and R. Lorenz, "Encoderless IPM traction drive for EV/HEV's," in *Industry Applications Conference, 2001. Thirty-Sixth IAS Annual Meeting. Conference Record of the 2001 IEEE*, 2001, pp. 1703-1707 vol.3.

[83] K. Jezernik, "Speed sensorless torque control of induction motor for EV's," in *7th International Workshop on Advanced Motion Control. Proceedings (Cat. No.02TH8623)*, 2002, pp. 236-241.

[84] W. Fengxiang, Z. Zhenbin, S. Alireza Davari, R. Fotouhi, D. Arab Khaburi, J. Rodriguez, *et al.*, "An Encoderless Predictive Torque Control for an Induction Machine With a Revised Prediction Model and EFOSMO," *Industrial Electronics, IEEE Transactions on,* vol. 61, pp. 6635-6644, 2014.

[85] B. Grcar, G. Stumberger, A. Hofer, and P. Cafuta, "IM Torque Control Schemes Based on Stator Current Vector," *Industrial Electronics, IEEE Transactions on,* vol. 61, pp. 126-138, 2014.

[86] M. Habibullah, D. D. C. Lu, D. Xiao, and M. F. Rahman, "A Simplified Finite-State Predictive Direct Torque Control for Induction Motor Drive," *Industrial Electronics, IEEE Transactions on,* vol. PP, pp. 1-1, 2016.

[87] N. Venkataramana Naik and S. P. Singh, "A Comparative Analytical Performance of F2DTC and PIDTC of Induction Motor Using DSPACE-1104," *Industrial Electronics, IEEE Transactions on,* vol. 62, pp. 7350-7359, 2015.

[88] D. Casadei, F. Profumo, G. Serra, and A. Tani, "FOC and DTC: two viable schemes for induction motors torque control," *Power Electronics, IEEE Transactions on,* vol. 17, pp. 779-787, 2002.

[89] C. Lascu, I. Boldea, and F. Blaabjerg, "Direct torque control of sensorless induction motor drives: a sliding-mode approach," *Industry Applications, IEEE Transactions on,* vol. 40, pp. 582-590, 2004.

[90] B. El Badsi, B. Bouzidi, and A. Masmoudi, "Bus-Clamping-Based DTC: An Attempt to Reduce Harmonic Distortion and Switching Losses," *Industrial Electronics, IEEE Transactions on*, vol. 60, pp. 873-884, 2013.

[91] V. S. S. P. K. Hari and G. Narayanan, "Theoretical and Experimental Evaluation of Pulsating Torque Produced by Induction Motor Drives Controlled with Advanced Bus-Clamping Pulse Width Modulation," *Industrial Electronics, IEEE Transactions on*, vol. PP, pp. 1-1, 2015.

[92] K. H. Nam, *Ac Motor Control and Electric Vehicle Applications*. Boca Raton, Florida: Taylor & Francis Group, 2010.

[93] I. K. Won, D. Y. Kim, Y. H. Jang, K. M. Choo, S. W. Hong, and C. Y. Won, "Improved FOC of IPMSM using model predictive current control decreasing switching loss for EV," in *2016 19th International Conference on Electrical Machines and Systems (ICEMS)*, 2016, pp. 1-6.

[94] M. Linke, "Injection of alternating carrier signals for sensorless control of revolving field machine," Ph.D. dissertation, Dept. Elect. Eng., Wuppertal Univ., Wuppertal, Germany 2003.

[95] G. F. Franklin, J. D. Powell, and A. Emami-Naeini, *Feedback Control of Dynamic Systems*, 6th ed. Upper Saddle River: Pearson Education, 2010.

[96] S. Myoung-Ho, H. Dong-Seok, C. Soon-Bong, and C. Song-Yul, "An improved stator flux estimation for speed sensorless stator flux orientation control of induction motors," *IEEE Transactions on Power Electronics*, vol. 15, pp. 312-318, 2000.

[97] Y. D. Landau, *Adaptive Control: The Model Reference Approach (Control and System Theory)* vol. 8. New York, USA: MARCEL DEKKER, INC., 1979.

# APPENDIX

Fig. 10.1 and Fig. 10.2 show overall Simulink implementation of the IM and PMSM models, respectively. Both models take in the 3-phase stator voltage from voltage source inverter output and in return calculate; the stator current components in the stationary reference frame, electromagnetic torque and mechanical speed in (rad/s).

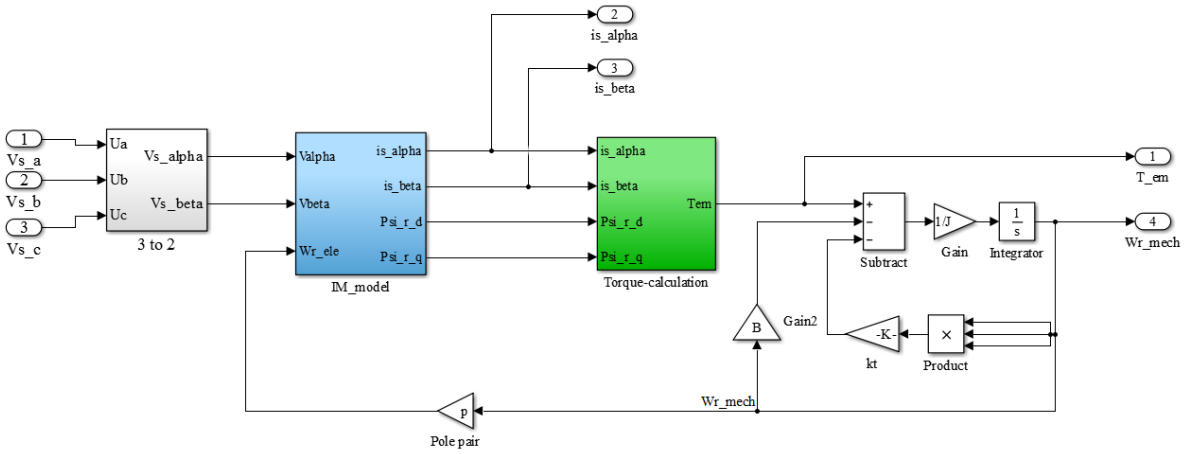


**Fig. 10.1. Simulink implementation of the IM model.**

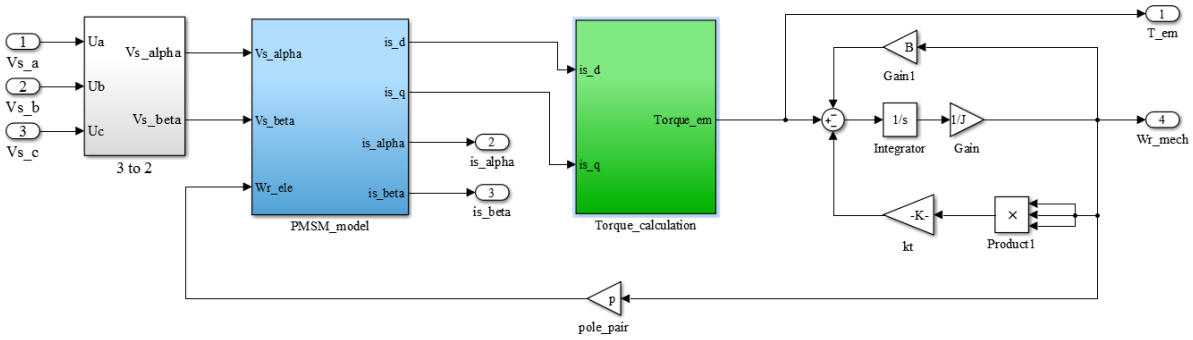


**Fig. 10.2. Simulink implementation of the PMSM model.**

Fig. 10.3 shows Simulink implementation of the voltage source inverter model. This model includes 2 µs deadtime delay on the rising edges of the switching signals. The block takes in the switching signals (S1, S2 and S3) from sinusoidal PWM block and in return provides 3-phase stator voltage inputs for electric motor models.

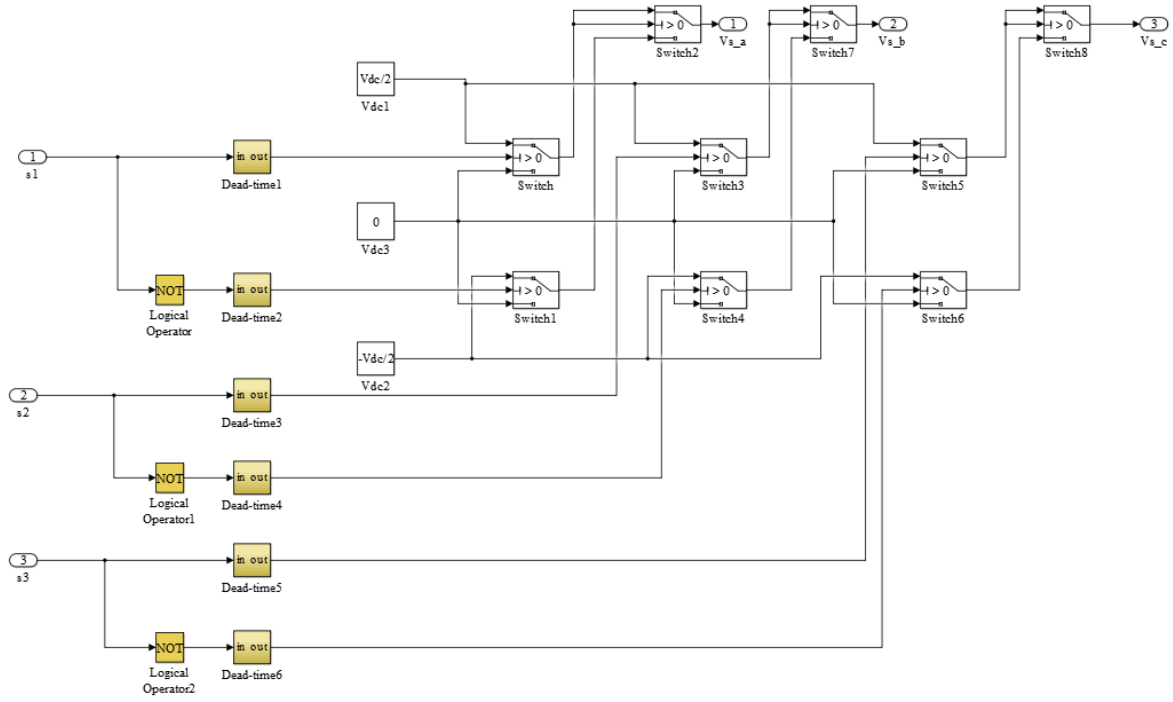


**Fig. 10.3. Simulink implementation of the voltage source inverter model.**

Fig. 10.4 shows Simulink implementation of the sinusoidal PWM with 8 kHz carrier.

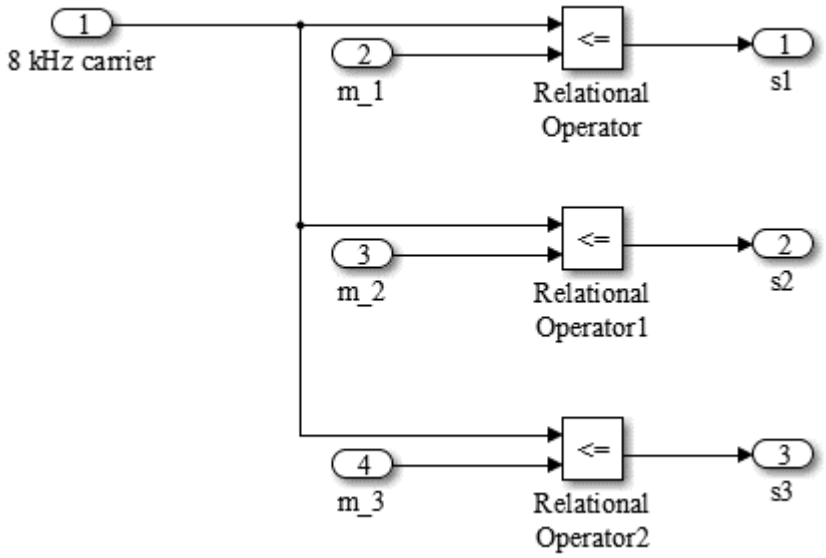


**Fig. 10.4. Simulink implementation of the sinusoidal PWM.**

Fig. 10.5 shows Simulink implementation of the IRFOC for the IM. This block takes in the applied torque reference, measured stator current components in the stationary reference frame and measured speed from the output of the IM block, and in return provides stator voltages to the input of the sinusoidal PWM block.

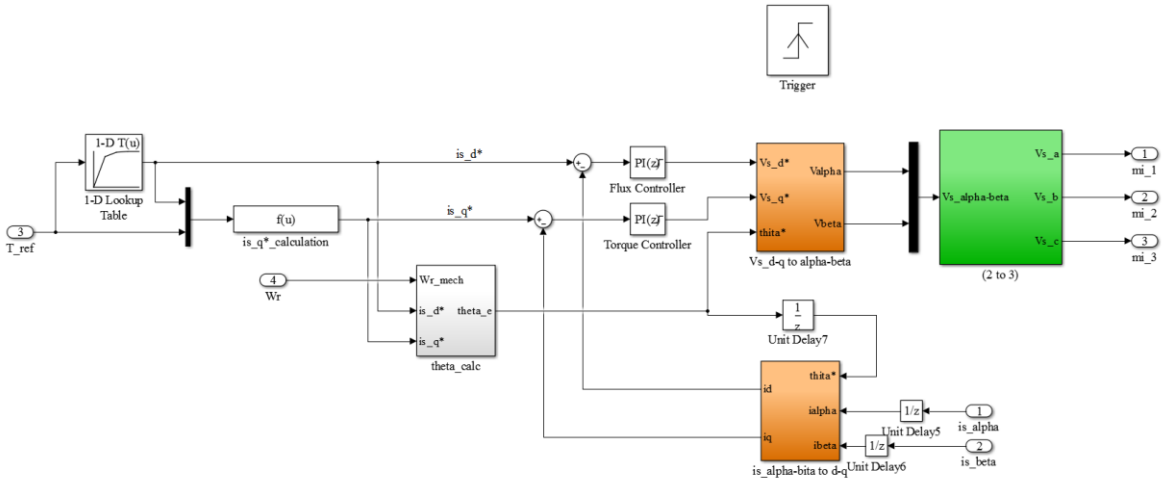


**Fig. 10.5. Simulink implementation of the IRFOC.**

Fig. 10.6 shows overall Simulink implementation of the torque-controlled drive for the voltage source inverter fed IM based on vector control using IRFOC.

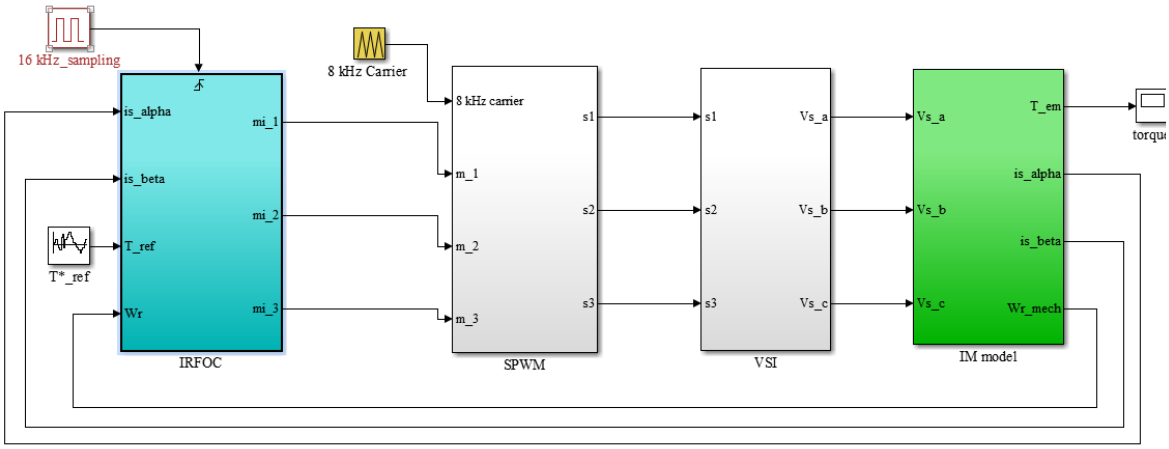


**Fig. 10.6. Simulink implementation of the TCD for the VSI fed IM based on vector control using IRFOC.**

Fig. 10.7 shows Simulink implementation of the equation (6.1). This is used for reconstruction of the stator voltage components in the stationary reference frame using DC-link voltage and switching signals. The equation is also shown below for convenience.

$$\bar{v}_{s\alpha\beta} = \frac{2 * V_{DC}}{3}\left(S_a + S_b e^{j\frac{2\pi}{3}} + S_c e^{-j\frac{2\pi}{3}}\right). \qquad (10.1)$$

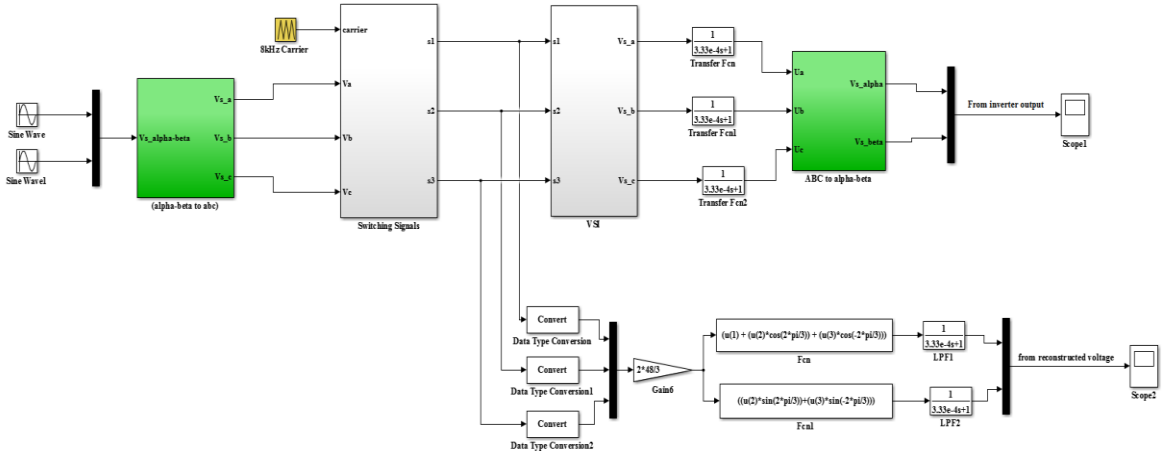


**Fig. 10.7. Simulink implementation of the equation (10.1).**

In order to demonstrate the validity of the equation (10.1), using Simulink, following test was carried out. The test contains comparison between the measured stator voltage from output of the VSI and reconstructed stator voltage components in the stationary reference frame. Fig. 10.8 (a) and -(b) show the stator voltage components in the stationary reference frame recorded

from the output of the VSI and reconstructed using equation (10.1), respectively. From results it is clear that both stator voltage components are similar in the frequency and amplitude.

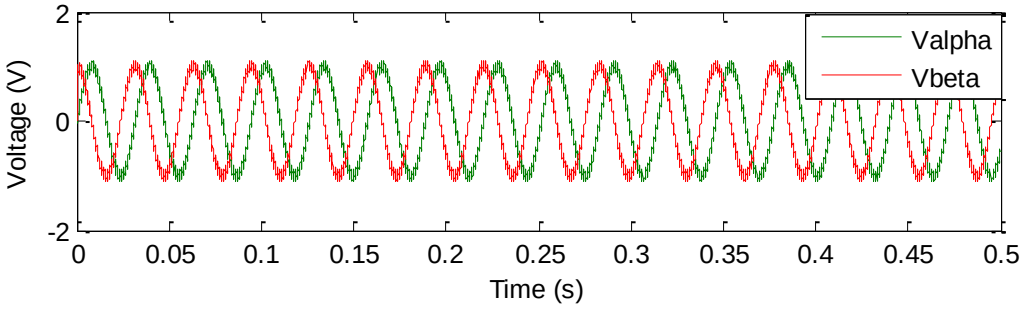


(a)

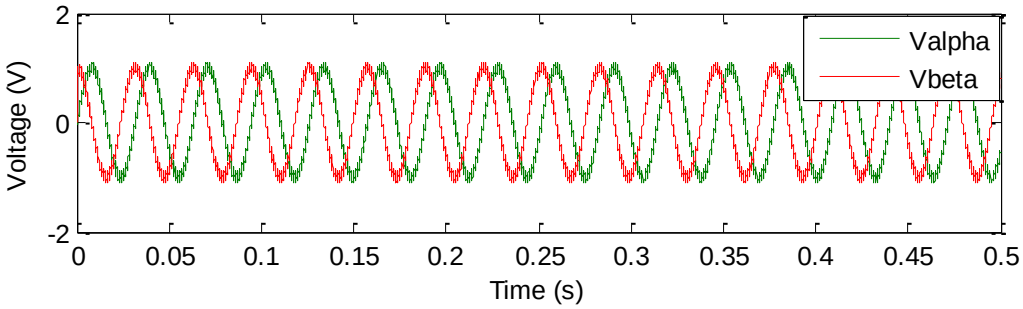


(b)

**Fig. 10.8. Simulation results for the stator voltage components in the stationary reference frame. (a) From output of the VSI and (b) reconstructed voltage from DC-link and switching signals equation (10.1).**